



AFRL-RI-RS-TR-2017-009

LINK AND NETWORK LAYERS DESIGN FOR ULTRA-HIGH-SPEED TERAHERTZ-BAND COMMUNICATIONS NETWORKS

STATE UNIVERSITY OF NEW YORK (SUNY) AT BUFFALO

JANUARY 2017

FINAL TECHNICAL REPORT

APPROVED FOR PUBLIC RELEASE; DISTRIBUTION UNLIMITED

STINFO COPY

**AIR FORCE RESEARCH LABORATORY
INFORMATION DIRECTORATE**

NOTICE AND SIGNATURE PAGE

Using Government drawings, specifications, or other data included in this document for any purpose other than Government procurement does not in any way obligate the U.S. Government. The fact that the Government formulated or supplied the drawings, specifications, or other data does not license the holder or any other person or corporation; or convey any rights or permission to manufacture, use, or sell any patented invention that may relate to them.

This report is the result of contracted fundamental research deemed exempt from public affairs security and policy review in accordance with SAF/AQR memorandum dated 10 Dec 08 and AFRL/CA policy clarification memorandum dated 16 Jan 09. This report is available to the general public, including foreign nationals. Copies may be obtained from the Defense Technical Information Center (DTIC) (<http://www.dtic.mil>).

AFRL-RI-RS-TR-2017-009 HAS BEEN REVIEWED AND IS APPROVED FOR PUBLICATION IN ACCORDANCE WITH ASSIGNED DISTRIBUTION STATEMENT.

FOR THE CHIEF ENGINEER:

/ S /

MICHAEL J. MEDLEY
Work Unit Manager

/ S /

JOHN D. MATYJAS
Technical Advisor, Computing &
Communications Division
Information Directorate

This report is published in the interest of scientific and technical information exchange, and its publication does not constitute the Government's approval or disapproval of its ideas or findings.

REPORT DOCUMENTATION PAGE

Form Approved
OMB No. 0704-0188

The public reporting burden for this collection of information is estimated to average 1 hour per response, including the time for reviewing instructions, searching existing data sources, gathering and maintaining the data needed, and completing and reviewing the collection of information. Send comments regarding this burden estimate or any other aspect of this collection of information, including suggestions for reducing this burden, to Department of Defense, Washington Headquarters Services, Directorate for Information Operations and Reports (0704-0188), 1215 Jefferson Davis Highway, Suite 1204, Arlington, VA 22202-4302. Respondents should be aware that notwithstanding any other provision of law, no person shall be subject to any penalty for failing to comply with a collection of information if it does not display a currently valid OMB control number.
PLEASE DO NOT RETURN YOUR FORM TO THE ABOVE ADDRESS.

1. REPORT DATE (DD-MM-YYYY) JAN 2017	2. REPORT TYPE FINAL TECHNICAL REPORT	3. DATES COVERED (From - To) FEB 2015 – SEP 2016		
4. TITLE AND SUBTITLE LINK AND NETWORK LAYERS DESIGN FOR ULTRA-HIGH-SPEED TERAHERTZ-BAND COMMUNICATIONS NETWORKS		5a. CONTRACT NUMBER FA8750-15-1-0050		
		5b. GRANT NUMBER N/A		
		5c. PROGRAM ELEMENT NUMBER 62702F		
6. AUTHOR(S) Josep Miquel Jornet, Erik Einarsson		5d. PROJECT NUMBER T2RB		
		5e. TASK NUMBER UB		
		5f. WORK UNIT NUMBER JJ		
7. PERFORMING ORGANIZATION NAME(S) AND ADDRESS(ES) University at Buffalo State University of New York (SUNY) 501 Capen Hall Buffalo, NY 14260		8. PERFORMING ORGANIZATION REPORT NUMBER		
9. SPONSORING/MONITORING AGENCY NAME(S) AND ADDRESS(ES) Air Force Research Laboratory/RITE 525 Brooks Road Rome NY 13441-4505		10. SPONSOR/MONITOR'S ACRONYM(S) AFRL/RI		
		11. SPONSOR/MONITOR'S REPORT NUMBER AFRL-RI-RS-TR-2017-009		
12. DISTRIBUTION AVAILABILITY STATEMENT Approved for Public Release; Distribution Unlimited. This report is the result of contracted fundamental research deemed exempt from public affairs security and policy review in accordance with SAF/AQR memorandum dated 10 Dec 08 and AFRL/CA policy clarification memorandum dated 16 Jan 09.				
13. SUPPLEMENTARY NOTES				
14. ABSTRACT Terahertz (THz)-band communication is an emerging technology that can address two relevant challenges for the U.S. Air Force. First, THz-band frequencies (0.1 to 10 THz) remain almost completely unutilized for communication; hence, being the first to exploit this band provides an unmatched technological advantage. Second, the huge transmission bandwidth associated with the THz-band can satisfy demand for higher data rates in communication networks, thereby enabling Terabit-per-second (Tbps) wireless links. The objective of this project is to establish the theoretical foundations for practical THz-band communication networks. Over the duration of the project (20 months), contributions have been made across different areas both related to THz device technologies as well as to physical and link layer solutions for THz communication networks. More specifically, in terms of THz devices, graphene-based plasmonic phase modulators and plasmonic nano-antenna arrays have been proposed, modeled and analyzed. In terms of physical and link layer solutions, new models for interference in THz communication, symbol detection and physical layer synchronization strategies; a packet size optimization framework; and link layer synchronization and medium access control protocols have been devised, formulated and modeled. These have also been validated by a combination of numerical, simulation and experimental results.				
15. SUBJECT TERMS Terahertz-band communications, terabit-per-second (Tbps), graphene-based antenna, graphene-based transceiver, plasmonic				
16. SECURITY CLASSIFICATION OF:		17. LIMITATION OF ABSTRACT UU	18. NUMBER OF PAGES 81	19a. NAME OF RESPONSIBLE PERSON Michael J. Medley
a. REPORT U	b. ABSTRACT U	c. THIS PAGE U		19b. TELEPHONE NUMBER (Include area code) N/A

Contents

1	SUMMARY	1
2	INTRODUCTION	2
3	GRAPHENE-BASED PLASMONIC PHASE MODULATOR	6
3.1	Motivation	6
3.2	Methods, Assumptions and Procedures	6
3.2.1	Propagation Properties of SPP Waves on Gated Graphene Structures	6
3.2.2	Graphene-based Plasmonic Phase Modulator	8
3.2.3	Performance Analysis	9
3.3	Results and Discussions	11
3.3.1	Model Validation	11
3.3.2	Constellation and Symbol Error Rate	11
3.3.3	Discussion	12
4	GRAPHENE-BASED PLASMONIC NANO-ANTENNA ARRAYS	14
4.1	Motivation	14
4.2	Methods, Assumptions and Procedures	15
4.2.1	Mutual Coupling Between Plasmonic Nano-Antennas	15
4.3	Coupling Coefficient	16
4.3.1	Performance of Plasmonic Nano-antenna Arrays	16
4.4	Results and Discussions	18
4.4.1	Simulation Validation of Mutual Coupling	18
4.4.2	Numerical Analysis of Array Performance	18
4.4.3	Discussion	20
5	MULTI-USER INTERFERENCE MODELING IN THE THZ BAND	22
5.1	Motivation	22
5.2	Methods, Assumptions and Procedures	22
5.2.1	System Model	22
5.2.2	Interference Model	24
5.3	Results and Discussions	27
5.3.1	Experimental Setup	27
5.3.2	Single Interferer Model Validation	29
5.3.3	Multiple Interferer Model Validation	30
5.3.4	Discussion	30
6	TERAHERTZ SYMBOL DETECTION AND PHYSICAL LAYER SYNCHRONIZATION	31
6.1	Motivation	31
6.2	Methods, Assumptions and Procedures	31
6.2.1	System Model and Synchronization Algorithm	31
6.2.2	Continuous-Time Moving-Average Detector	34
6.2.3	Throughput Analysis	37
6.3	Results and Discussions	38
6.3.1	Synchronization Test with Experimental Data	38
6.3.2	Numerical Results	39
6.3.3	Discussion	41

7	PACKET SIZE OPTIMIZATION	43
7.1	Motivation	43
7.2	Methods, Assumptions and Procedures	44
7.2.1	System Model and Optimization Problem Formulation	44
7.2.2	Problem Solution Approach and Algorithm	49
7.3	Results and Discussions	50
7.3.1	Numerical Results and Performance Evaluation	50
8	LINK LAYER SYNCHRONIZATION AND MEDIUM ACCESS CONTROL	54
8.1	Motivation	54
8.2	Methods, Assumptions and Procedures	55
8.2.1	THz-band Communication System Model	55
8.2.2	Receiver-initiated Synchronization and Medium Access Control Protocol	57
8.3	Results and Discussions	62
8.3.1	Macroscale Scenario	62
8.3.2	Nanoscale Scenario	62
8.3.3	Discussion	63
9	CONCLUSIONS	65
10	LIST OF ACRONYMS	66

List of Figures

1	Graphene-based plasmonic phase modulator.	8
2	Electric field distribution over a graphene-based waveguide at $f_c=4$ THz, for different Fermi energies, E_F ($L=2$ μ m, $d=90$ nm).	12
3	Frequency response of the phase modulator, as a function of the Fermi energy, E_F , for different carrier frequencies f_c ($L=2$ μ m, $d=90$ nm).	12
4	Performance of a binary plasmonic phase modulator with $E_{F,0} = 0.28$ eV, $E_{F,1} = 0.13$ eV, ($f_c=4$ THz, $L=2$ μ m, $d=90$ nm).	13
5	Graphene-based plasmonic nano-antenna array.	14
6	Resonance frequency as a function of the separation distance between resonant elements for different antenna resonant frequencies.	19
7	Directivity and power gain of a nine antenna uniform planar array as functions of the separation between elements.	20
8	Total gain of a graphene-based plasmonic nano-antenna array, as a function of the number of elements.	21
9	Illustration of a TS-OOK transmission.	23
10	Sinusoidal approximation of the transmitted pulse in TS-OOK.	25
11	Illustration of the THz beam from the transmitter (Tx) to receiver (Rx) via reflections from the metal rods, which emulate interference from multiple nodes.	27
12	Top view of the linear apparatus that holds the metal rods in place.	28
13	THz pulse from the reflection off of one metal rod in position 13.	28
14	Measured and approximated received pulse energy as functions of the transmission distance.	28
15	Interference distribution of a single interferer.	29
16	Interference distribution of two interferers.	29
17	Illustration of PDF converging to Gaussian with increasing number of nodes.	30
18	Synchronization block diagram.	32
19	CTMA symbol detector block diagram.	34
20	Window length bigger than T_p (top); Window length equal to T_p , but pulse does not fit in a single integration window (center); Window length equal to T_p and pulse fits in a single integration window (bottom).	35
21	Illustration of the synchronization algorithm for $m = x = 2$: First iteration (top); Second iteration (middle); Third iteration (bottom).	39
22	Maximum number of bits before resynchronization as a function of m^x , for different values of the clock skew μ	40
23	SER as a function of the SNR for different values of m^x	40
24	Throughout as a function of the SNR for different values of m^x (frame length=1000 bits).	41
25	Throughout as a function of the SNR for different values of x ($m=2$, frame length=1000 bits).	41
26	Throughout as a function of the SNR for different values of bits ($m=3$, $x=6$).	41
27	Link efficiency for ARQ, when $d = 1$ cm.	52
28	Link efficiency for different error-control techniques, when $d = 1$ cm and $\lambda_{harv} = 200$ nJ/s.	52

29	Optimal link efficiency for different error-control techniques, when $\lambda_{harv} = 200$ nJ/s, and $L_{data}^{max} = 16$ Kbits.	52
30	Optimal packet size for different error-control techniques, when $\lambda_{harv} = 200$ nJ/s, and $L_{data}^{max} = 16$ Kbits.	53
31	Optimal link efficiency for different error-control techniques, when $d = 1$ mm, and $L_{data}^{max} = 16$ Kbits.	53
32	Discard probability as a function of the antenna turning speed ω	63
33	Throughput as a function of the antenna turning speed ω	63
34	Packet discard probability as a function of the node density.	64
35	Throughput as a function of the node density.	64

1 SUMMARY

Terahertz (THz)-band communication is an emerging technology that can address two relevant challenges for the U.S. Air Force. First, THz-band frequencies (0.1 to 10 THz) remain almost completely unutilized for communication; hence, being the first to exploit this band provides an unmatched technological advantage. Second, the huge transmission bandwidth associated with the THz-band can satisfy demand for higher data rates in communication networks, thereby enabling Terabit-per-second (Tbps) wireless links. The objective of this project is to establish the theoretical foundations for practical THz-band communication networks. Over the duration of the project (20 months), contributions have been made across different areas both related to THz device technologies as well as to physical and link layer solutions for THz communication networks. More specifically, in terms of THz devices, graphene-based plasmonic phase modulators and plasmonic nano-antenna arrays have been proposed, modeled and analyzed. In terms of physical and link layer solutions, new models for interference in THz communication, symbol detection and physical layer synchronization strategies; a packet size optimization framework; and link layer synchronization and medium access control protocols have been devised, formulated and modeled. These have also been validated by a combination of numerical, simulation and experimental results.

2 INTRODUCTION

Over the last few years, wireless data traffic has drastically increased due to a change in the way today's society creates, shares and consumes information. In 2015, the need to provide wireless connectivity to *anything, anywhere, anytime* has resulted in more than 7.9 million mobile devices connected to the Internet, which have generated a total of 3.7 exabytes per month of mobile data traffic [1]. Moreover, estimates forecast that there will be 11.6 billion mobile-connected devices by 2020, mainly in part due to the Internet of Things paradigm. In parallel with the growth in the total number of interconnected devices, there has been an increasing demand for higher speed wireless communication. In particular, wireless data rates have doubled every eighteen months for the last three decades [2]. Following this trend, *Terabit-per-second (Tbps) links* are expected to become a reality within the next five years.

Several alternatives are being considered to meet this demand. *At frequencies below 5 GHz*, advanced digital modulations and sophisticated physical layer schemes are being used to achieve a very high spectral efficiency. However, the very small available bandwidth in the overcrowded electromagnetic (EM) spectrum limits the achievable data rates. For example, in Long-Term Evolution Advanced (LTE-A) networks, peak data rates on the order of 1 Gigabit-per-second (Gbps) are feasible over 100 MHz of aggregated bandwidth when utilizing a 4×4 MIMO scheme [3]. Similarly, dynamic spectrum access and sharing techniques are being heavily investigated to better utilize the available bandwidth. While these technologies will contribute to achieve maximum spectral efficiency, they are far from being able to support Tbps.

Millimeter-wave (mm-wave) communication systems (30 to 300 GHz) have gained a lot of attention in the last few years due to their ability to support much higher data rates than communication systems below 5 GHz [4]. Several sub-bands have been allocated for communications, including 38.6 to 40 GHz (1.4 GHz bandwidth), 57 to 64 GHz (7 GHz bandwidth, but usually smaller due to international regulations) and 71 to 76 GHz / 81 to 86 GHz (10 GHz bandwidth in total). Millimeter-wave technology is already playing a key role in current systems (e.g., IEEE 802.11ad), and will continue to do so in future (e.g., 5G cellular) systems. While this is the way to go, the total consecutive available bandwidth for mm-wave communication systems is still less than 10 GHz. This would require a physical layer efficiency of almost 100 bps/Hz to support Tbps, which is several times higher than that of the state of the art for existing systems. This result motivates further research and the exploration of even higher frequency bands for communication.

Optical wireless communication (OWC) systems, which operate in the infrared (187 to 400 THz / 750 to 1600 nm), visible (400 to 770 THz / 390 to 750 nm), or even ultraviolet (1000 to 1500 THz / 200 to 280 nm) EM spectrum bands, are similarly being explored as a way to improve the achievable data rates in wireless networks [5]. The intrinsically very large available bandwidth at such very high frequency plays to their advantage. However, there are several aspects that currently limit these approaches and require further research, including the size and limited portability of infrared systems; low transmission power budget due to eye-safety limits and the impact of atmospheric effects on the signal propagation (e.g., scattering from molecules and particles); or the impact of ambient noise in visible communication (e.g., any light source).

In this context, ***Terahertz-band (0.1 to 10 THz) communication is envisioned as a key wireless technology to satisfy the need for much higher wireless data rates [6–9]***. This frequency band, which lies between mm-waves and the far infrared, remains still one of the least explored regions in the EM spectrum. For many decades, the lack of compact high-power signal

sources and high-sensitivity detectors able to work at room temperature has hampered the use of the THz band for any application beyond sensing. However, many recent advancements with different technologies is finally closing the so-called THz gap. For example, on the one hand, in an *electronic approach*, III–V semiconductor technologies have demonstrated record performance in terms of output power, noise figure, and power-added efficiency at sub-THz frequencies, and are quickly approaching the 1 THz mark [10–12]. On the other hand, in an *optics approach*, Quantum Cascade Lasers are rising as potential candidates for high-power THz-band signal generation [13–16]. More recently, the use of nanomaterials such as graphene is enabling the development of novel plasmonic devices, which intrinsically operate in the THz-band [17–22].

Independently of the specific enabling technology, **THz-band communication can address two relevant challenges for the US Air Force (USAF)**. First, THz-band frequencies remain almost completely unutilized for communication; hence, being the first to exploit this band provides an unmatched technological advantage. Second, the huge transmission bandwidth associated with the THz-band can satisfy demand for higher data rates in communication networks, thereby enabling Terabit-per-second wireless links [8]. Nevertheless, this very large bandwidth comes at the cost of a very high propagation loss [23], mainly because of molecular absorption, which also creates a unique distance dependence on the available bandwidth. All these introduce many challenges to practical THz communication systems and require the development of innovative solutions. Moreover, many of these might be *helpful for broadband wireless communication systems below and above the THz band, i.e., mm-waves and OWC, respectively*.

The objective of this project is to establish the theoretical foundations for practical THz-band communication networks. Along this 20-month-long project, contributions have been made across different areas, ranging from new graphene-based plasmonic devices for *true* THz communications, to new physical and link layer protocols for ultra-broadband networking in the THz band. More specifically, contributions have been made along the following intertwined thrusts:

- **Graphene-based Plasmonic Phase Modulator (Sec. 3):** While major efforts have been made towards developing compact THz sources and detectors able to work at room temperature, the modulator/demodulator is a fundamental block in any communication system. As part of this effort, we have proposed, modeled and analyzed the performance of a graphene-based modulator able to tune on demand the phase of a propagating Surface Plasmon Polariton (SPP) wave as it propagates from the source towards the antenna. This work has been published in [24] and an extended version of the work is being prepared for journal publication. In addition, the University at Buffalo is currently preparing a US Patent Application for this invention.
- **Graphene-based Plasmonic Nano-antenna Arrays (Sec. 4):** The limited power of THz transceivers and the very high path loss at THz frequencies drastically limit the transmission distance between THz devices. To overcome this limitation, by taking advantage of the very small size of THz plasmonic transceivers and antennas, massive nano-antenna arrays can be created [25]. As part of this project, we have proposed, modeled and analyzed the performance of graphene-based plasmonic nano-antenna arrays, whose radiation diagram can be dynamically tuned in space and frequency. This work has been published in [26], and an extended version of the work is being prepared for journal publication. In addition, new strategies to experimentally fabricate the proposed structures have been devised and disseminated to the research community [27]. Moreover, we have set up a pioneering

experimental characterization platform for 2D nanomaterials and nanostructures, to be used for the analysis of the developed devices, and published the results in [28].

- **Interference Modeling in THz Pulse-based Communications (Sec. 5):** Many of the envisioned applications of THz-band communications involved a large number of devices communicating over short distances at very high data-rates (up to Tbps) [29]. In such scenarios, multi-user interference can become a bottleneck if not properly addressed. As part of this effort, we have developed and experimentally validated a stochastic multi-user interference model for THz-band communication networks. The proposed model takes into account not just the power of interfering signals, but also their precise time-domain waveforms. An innovative testbed has been developed to validate the analytical models. This work has been published in [30] and an extended version is currently in preparation. In addition, we have also explored and published both stochastic geometry [31] and novel integral geometry [32] approaches to interference modeling in THz communication networks.
- **Symbol Detection and Physical Layer Synchronization (Sec. 6):** When transmitting at Gbps and Tbps, physical layer synchronization becomes one of the main challenges due to the very short symbol duration. Due to the lack of Analog-to-Digital Converters (ADCs) able to digitize the received signal at rates close to the Nyquist frequency, analog synchronization schemes are needed. As part of this effort, we have proposed, modeled and experimentally tested an analog symbol detection and synchronization scheme, built upon graphene-based voltage-controlled delay (VCD) lines and a continuous-time moving-average (CTMA) detector. The developed work has been published in [33] and an extended version is in preparation.
- **Packet Size Optimization for THz Communication (Sec. 7):** One of the key applications of THz communications is in the field of nanonetworks and wireless nanosensor networks (WNSNs) [29,34]. While the THz band provides nanosensors with a very large bandwidth [23], the limited capacity of nano-batteries, which requires the use of time-consuming energy-harvesting procedures [35,36], and the limited computational capabilities of nanosensors, affect the throughput of WNSNs. All these interdependencies motivate the joint analysis of the nano-device capabilities, the THz band peculiarities and their impact on the achievable throughput. As part of this effort, we have tackled the throughput maximization problem in WNSNs, by taking into account the existing device and communication interdependencies, and identified the optimal packet size for different system-level objectives. The developed work has been published in [37].
- **Link Layer Synchronization and Medium Access Control Protocols for THz Networks (Sec. 8):** Traditionally, Medium Access Control (MAC) protocols have been designed by taking into account that the most scarce resource is the channel available bandwidth. As a result, nodes usually need to contend for the channel. At THz frequencies, perhaps the only resource which is not limiting is the bandwidth. However, as mentioned earlier, this bandwidth comes at the cost of a very high propagation loss, which imposes both energy constraints in battery-powered devices and the need for ultra-directional communications among spaced devices. As part of this effort, we have proposed, modeled and analyzed the performance of new MAC protocols that shift the focus from the channel to the receiver. The proposed receiver-initiated protocols rely on a one-way handshake triggered by the receiver, and can effectively

outperform existing zero-way (i.e., ALOHA-type) or 2-way (i.e., CSMA-type) protocols in terms of achievable throughput. This work has been published in [38], and an extended journal version has been submitted for publication. In addition, we have proposed, modeled and analyzed a dual-band MAC protocol, aimed at synergistically leveraging the advantages of both 2.4 GHz (omnidirectional transmissions) and THz (ultra-high data-rates) [39].

In the following sections, we describe the Methods, Assumptions, Procedures, Results and Discussions for each of the aforementioned contributions.

3 GRAPHENE-BASED PLASMONIC PHASE MODULATOR

3.1 Motivation

In the last decade, there has been major progress towards developing new types of THz sources and detectors [10–16, 21], usually in the context of THz sensing and imaging applications. When it comes to communications, in addition to THz signal sources and detectors, a modulator is needed to embed information on the transmitted signals. The desired properties of a modulator include high modulation bandwidth, i.e., the speed at which the properties of the modulated signal can be changed, and high modulation depth, i.e., the maximum difference between modulation states. Different types of modulators able to control the amplitude or phase of THz waves have been developed to date [40]. In [41], a high-electron-mobility transistor based on a III-V semiconductor material was utilized to modulate the amplitude of a THz wave. In [42], a metamaterial-based modulator was utilized to control the phase of a THz wave. In both cases, sub-GHz modulation bandwidths and low modulation depths limit the use of these devices in practical communication systems.

More recently, the use of graphene to develop THz wave modulators has been proposed [43]. Graphene has excellent electrical conductivity, making it very well suited for propagating extremely-high-frequency electrical signals [18]. In [44], a graphene-based amplitude modulator for THz waves was developed. This was enabled by the possibility to dynamically control the conductivity of graphene. In [45], a similar principle was exploited in a graphene-based meta-device. In these setups, the main challenge is to increase the modulation depth. A low modulation depth makes the transmitted symbols more difficult to distinguish and, thus, results in higher symbol error rates (SER) in practical communication systems.

As part of this project, we have proposed, modeled and analyzed the performance of a graphene-based plasmonic phase modulator for THz-band communications. Our proposed modulator consists of a fixed-length graphene-based plasmonic waveguide with a metallic back gate. Its working principle relies on the possibility to electronically control the propagation speed of a Surface Plasmon Polariton (SPP) wave on graphene at THz frequencies by modifying the chemical potential of the graphene layer. In this section, we summarize our contributions towards this aim. In Sec. 3.2.1, starting from the dynamic complex conductivity of graphene and a revised dispersion equation for SPP waves, we develop an analytical model for the plasmonic phase modulator. By utilizing the model, in Sec. 3.2.3, we analyze the performance of the proposed plasmonic modulator when utilized to implement a M-ary phase shift keying modulation in terms of SER. Finally, we validate the model by means of electromagnetic simulations, and provide numerical results to illustrate the modulator performance in Sec. 3.3.

3.2 Methods, Assumptions and Procedures

3.2.1 Propagation Properties of SPP Waves on Gated Graphene Structures

The analysis of the proposed plasmonic phase modulator requires the characterization of the SPP propagation properties on graphene. These depend on the conductivity of the graphene sheet. In this section, we first recall the conductivity model utilized in our analysis and then define the dispersion equation for SPP waves on gated graphene structures.

Complex Conductivity Model of Graphene In our analysis, we consider a surface conductivity model for infinitely large graphene sheets obtained using the Kubo formalism [46, 47]. This is given by

$$\sigma^g = \sigma_{\text{intra}}^g + \sigma_{\text{inter}}^g, \quad (1)$$

$$\sigma_{\text{intra}}^g = i \frac{2e^2}{\pi \hbar^2} \frac{k_B T}{\omega + i\tau_g^{-1}} \ln \left(2 \cosh \left(\frac{E_F}{2k_B T} \right) \right), \quad (2)$$

$$\sigma_{\text{inter}}^g = \frac{e^2}{4\hbar} \left(H \left(\frac{\omega}{2} \right) + i \frac{4\omega}{\pi} \int_0^\infty \frac{G(\epsilon) - G(\omega/2)}{\omega^2 - 4\epsilon^2} d\epsilon \right), \quad (3)$$

and

$$G(a) = \frac{\sinh(\hbar a / k_B T)}{\cosh(E_F / k_B T) + \cosh(\hbar a / k_B T)}, \quad (4)$$

where $\omega = 2\pi f$, $\hbar = h/2\pi$ is the reduced Planck's constant, e is the electron charge, k_B is the Boltzmann constant, T is temperature, E_F refers to the Fermi energy of the graphene sheet, and τ_g is the relaxation time of electrons in graphene, which depends on the electron mobility μ_g . E_F can be easily modified by means of electrostatic bias or gating of the graphene layer, enabling the aforementioned antenna tuning.

As we showed in [19], a more accurate conductivity model can be developed by taking into account the impact of electron lateral confinement on graphene nano-ribbons, but the two models converge for graphene strips which are 50 nm wide or more. In our analysis, we consider plasmonic resonant cavities which are a few hundred nanometers wide. Finally, from [46, 47], it is important to note that the conductivity model described by (1) and the following was derived by neglecting the spatial dispersion of the AC field. Therefore, it can be used for the analysis of the SPP propagation in the long wavelength limit only, i.e., $\omega \gg k_{\text{spp}} v_F$, where k_{spp} is the SPP wave number and $v_F \approx 8 \times 10^5$ m/s is the Fermi velocity of Dirac fermions in graphene.

Dispersion Equation for Surface Plasmon Polariton Waves The propagation properties of SPP waves can be obtained by deriving and solving the SPP wave dispersion equation on graphene. In many of the related graphene plasmonic works [48–50], the dispersion equation was obtained by considering a graphene layer at the interface between two infinitely large dielectric materials, usually between air and silicon dioxide (SiO_2). However, the proposed modulator relies on the presence of a metallic ground plane at a distance d from the graphene layer, which is needed both to create the plasmonic waveguide as well as to control the Fermi energy of the graphene layer and tune its conductivity.

From [51], the dispersion equation for Transverse Magnetic (TM) SPP waves on gated graphene structures in the quasi-static regime—i.e., for $k_{\text{spp}} \gg \omega/c$, where c is the speed of light—is given by

$$-i \frac{\sigma^g}{\omega \epsilon_0} = \frac{\epsilon_1 + \epsilon_2 \coth(k_{\text{spp}} d)}{k_{\text{spp}}}, \quad (5)$$

where σ^g is the conductivity of graphene given by (1), ϵ_1 is the relative permittivity of the dielectric above the graphene layer, and ϵ_2 is the relative permittivity of the dielectric between the graphene layer and the metallic ground plane, which are separated by a distance d . It can be easily shown by

taking the limit of $d \rightarrow \infty$ that (5) tends to the quasi-static dispersion equation of SPP waves in ungated graphene used in the aforementioned works.

By solving (5), the complex wave vector k_{spp} can be obtained. The real part of the wave vector,

$$\text{Re}\{k_{spp}\} = \frac{2\pi}{\lambda_{spp}} = \frac{\omega}{v_p}, \quad (6)$$

determines the SPP wavelength λ_{spp} and the SPP wave propagation speed. The imaginary part determines the SPP decay or, inversely,

$$\mathcal{L} = \frac{1}{2 \text{Im}\{k_{spp}\}}, \quad (7)$$

determines the SPP propagation length, which is defined as the distance at which the SPP intensity has decreased by a value of $1/e$. Unfortunately, a closed-form expression for k_{spp} in this case does not exist, but can only be obtained numerically.

3.2.2 Graphene-based Plasmonic Phase Modulator

In this section, we explain the working principle of the plasmonic phase modulator and develop its analytical model.

Working Principle The conceptual design of the proposed graphene-based plasmonic phase modulator is shown in Fig. 1. The phase modulator consists of a plasmonic waveguide, which is composed of a graphene sheet (the plasmonic material) mounted over a metallic flat surface (the ground plane), with a dielectric material layer in between, which supports the graphene layer. In this paper, we consider that a SPP wave is already propagating over the graphene layer. Different mechanisms could be utilized to launch the SPP wave. For example, a THz plasma wave could be generated by a HEMT-like device and coupled to the graphene waveguide [21]. Alternatively, a Quantum Cascade Laser and a grating structure could be utilized for the same [14].

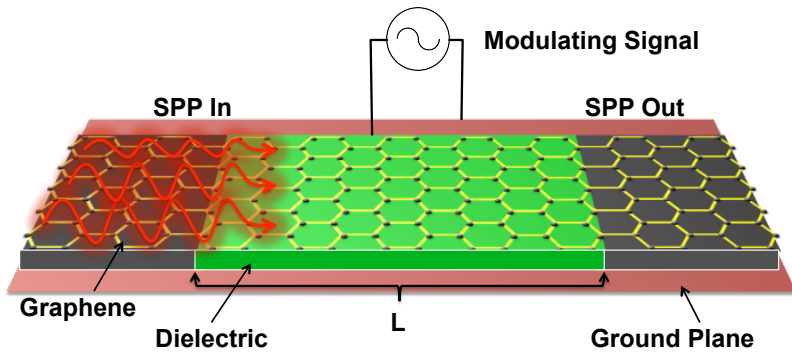


Fig. 1: Graphene-based plasmonic phase modulator.

The basic idea for any phase modulator is to establish a relation between the data bits to be transmitted, which constitute the modulating signal, and the transmitted signal phase. In our proposed plasmonic phase modulator, the modulating signal is applied as a bias voltage to the graphene layer and controls its Fermi energy, E_F . From (6), (5) and (1), it is clear that the Fermi

energy directly controls the propagation speed of the SPP wave on the gated graphene structure. Therefore, for a fixed length waveguide, the phase at the output of the waveguide is effectively modulated by the data bits to be transmitted. The resulting signal can be further propagated and eventually radiated in free-space by means of a plasmonic nano-antenna [19, 49, 50].

Analytical Model In this section we develop an analytical model for the phase of the plasmonic signal at the output of the plasmonic phase modulator shown in Fig. 1. We denote the plasmonic signals at the input and the output of the plasmonic waveguide as X and Y , respectively. The modulator frequency response is denoted by H . The following relation can be then written,

$$Y(f, E_F) = X(f) H(f, E_F), \quad (8)$$

where f stands for frequency and E_F is the Fermi energy of the graphene layer on which the SPP wave propagates.

The modulator frequency response H is given by

$$H(f, E_F) = |H(f, E_F)| \exp(j\theta(f, E_F)), \quad (9)$$

where $|H|$ accounts for the variation in the SPP wave intensity and θ represents the change in the SPP phase at the output of the fixed-length waveguide.

From Sec. 3.2.1, the magnitude of the modulator response can be written as

$$|H(f, E_F)| = \exp(-2 \operatorname{Im}\{k_{spp}(f, E_F)\}L), \quad (10)$$

where L represents the waveguide length.

The total phase change θ that the SPP wave suffers as it propagates through the waveguide is given by

$$\theta(f, E_F) = \frac{2\pi L}{\lambda_{spp}(f, E_F)} = L \operatorname{Re}\{k_{spp}(f, E_F)\}, \quad (11)$$

where λ_{spp} is the plasmonic wavelength obtained from k_{spp} as discussed in Sec. 3.2.1, which depends on the signal frequency f and the Fermi energy E_F .

By combining (10) and (11) in (9), the modulator frequency response can be written as

$$H(f, E_F) = \exp(-2 \operatorname{Im}\{k_{spp}(f, E_F)\}L) \cdot \exp(j \operatorname{Re}\{k_{spp}(f, E_F)\}L). \quad (12)$$

In an ideal phase modulator, the intensity or amplitude of the signal should remain constant, independently of the phase. However, the SPP decay in graphene structures is not negligible. As a result, we cannot independently modulate the signal amplitude and phase. This has a direct impact on the performance of the modulator in a practical communication system, which we analyze in the next section.

3.2.3 Performance Analysis

In this section, we define the constellation of a non-uniform plasmonic phase shift keying digital modulation and formulate the SER for M-ary modulations.

Signal Space Constellation The signal space or constellation represents the possible symbols generated by a given modulation scheme as points in the complex plane. The real part of each of such points is referred to as the in-phase component and the imaginary part denotes the quadrature component.

The number of modulated symbols or points in the constellation is given by $M = 2^k$, where $k = 2, 4, \dots$ refers to the modulation order. The position of each symbol S_m , $m = 1..M$, depends on the modulator behavior. For the system described in Sec. 3.2.2, at fixed carrier frequency f_c , the magnitude and phase of each symbol is given by

$$S_m = |S_m| \exp(\theta_m), \quad (13)$$

$$|S_m| = A_0 |H(f_c, E_{F,m})|, \quad (14)$$

$$\theta_m = \theta_0 + \theta(f_c, E_{F,m}), \quad (15)$$

where A_0 and θ_0 refer to the amplitude and phase of the input SPP wave. $E_{F,m} = \{E_{F,1}, E_{F,2}, \dots, E_{F,M}\}$ is the set of Fermi energies that correspond to the transmitted symbols. In our analysis, we consider $A_0 = 1$ and $\theta_0 = 0$. The constellation for the proposed plasmonic phase modulator can only be numerically obtained and will be provided in Sec. 3.3.

Symbol Error Rate The most common metric for a modulation scheme in a practical communication system is the SER. This is implicitly related to the modulation intensity or depth. The more “distinguishable” the symbols are, the lower the SER. In general terms, for a modulated symbol S_m , the symbol error probability P_e is given by [52],

$$P_e = P\{\text{Detect } S_{\tilde{m}}, \tilde{m} \neq m \mid \text{Given that } S_m \text{ is sent}\}, \quad (16)$$

where $m = 1, 2, 3, \dots, M$. The SER for a digital phase modulation with uniform constellation is derived based on the symbol decision regions, which due to symmetry, are easy to define. However, this is not the case for non-uniform modulations. Instead, the SER for the proposed plasmonic phase modulation scheme can be directly derived starting from the distance between symbols in the non-uniform constellation.

In general terms, the union bound for the SER is given by [52],

$$SER \leq \frac{1}{M} \sum_{m=1}^M \sum_{\substack{1 \leq \tilde{m} \leq M \\ \tilde{m} \neq m}} Q \left[\sqrt{\frac{D(S_m, S_{\tilde{m}})^2}{2N_0}} \right], \quad (17)$$

where the Q function refers to the tail probability of the standard normal distribution, $D(S_m, S_{\tilde{m}})$ stands for the distance between two symbols S_m and $S_{\tilde{m}}$, and is given by

$$D(S_m, S_{\tilde{m}})^2 = \|S_m - S_{\tilde{m}}\|^2, \quad (18)$$

and N_0 is the noise power spectral density.

A common representation of the SER is as a function of signal-to-noise ratio (SNR) or the energy per symbol to noise power spectral density E_s/N_0 . From (14), this is given by

$$SNR_m = \frac{E_{s,m}}{N_0} = \frac{|H_m(f_c, E_F)|^2}{N_0}. \quad (19)$$

Finally, by combining (17), (18) and (19), the SER for the non-uniform constellation can be further expressed as

$$SER \leq \frac{1}{M} \sum_{m=1}^M \sum_{\substack{1 \leq \tilde{m} \leq M \\ \tilde{m} \neq m}} Q \left[\left(\frac{E_{s,m} e^{j2\theta_m}}{N_0} + \frac{E_{s,\tilde{m}} e^{j2\theta_{\tilde{m}}}}{N_0} - 2 \cos(\theta_m + \theta_{\tilde{m}}) \sqrt{\frac{E_{s,m}}{N_0} \cdot \frac{E_{s,\tilde{m}}}{N_0}} \right)^{1/2} \right]. \quad (20)$$

The SER will be numerically investigated in the next section.

3.3 Results and Discussions

In this section, we validate our models and analyze the performance of the proposed plasmonic phase modulator.

3.3.1 Model Validation

We utilize COMSOL Multi-physics to simulate the behavior of the plasmonic phase modulator shown in Fig. 1. Graphene is modeled as a transition boundary condition with impedance given by (1), with $\tau_g = 2.2$ ps at room temperature $T = 300$ K. The graphene layer rests on top of a metallic ground plane with a 90 nm-thick SiO_2 dielectric in between ($\varepsilon_r = 4$). In Fig. 2, the z-component of the electric field on a 2- μm -long graphene-based waveguide is shown for $f_c = 4$ THz and two values of E_F , namely, 0.13 eV and 0.28 eV. For $E_F = 0.13$ eV, the waveguide length L corresponds to approximately one and a half SPP wavelength and, thus, it introduces a phase change of π . For $E_F = 0.28$ eV, the waveguide length L corresponds to one full SPP wavelength and introduces a phase change of 2π . Hence, we can define a plasmonic phase modulator of order $M=2$, where bit “0” is transmitted as a phase change of 2π by tuning E_F to 0.28 eV and bit “1” is transmitted with a phase change of π by tuning E_F to 0.13 eV.

In addition to the phase, we are interested in the change in the amplitude of the SPP wave amplitude, as it will affect the signal space constellation and the SER. In Fig. 3(a) and Fig. 3(b), we illustrate the magnitude and phase of the plasmonic phase modulator as a function of the Fermi energy, E_F , and for different carrier frequencies, f_c . On the one hand, we are interested in working in a range of E_F such that the magnitude of the modulator does not significantly change. On the other hand, however, we need at least a phase difference of π to create orthogonal symbols. Next, we investigate the performance of a specific modulator design.

3.3.2 Constellation and Symbol Error Rate

In Fig. 4(a), the non-uniform constellation for a plasmonic phase modulator with $f_c = 4$ THz, $E_{F,0} = 0.28$ eV, $E_{F,1} = 0.13$ eV, and $L = 2\mu\text{m}$, $d = 90$ nm is shown. Similarly, in Fig. 4(b), the SER (17) for the proposed modulator is shown as a function of the SNR and compared to that of a uniform binary phase shift keying (BPSK) modulation with the same average energy per symbol E_s . As expected, the SER for the proposed modulator is slightly higher but still comparable to that of the uniform case.

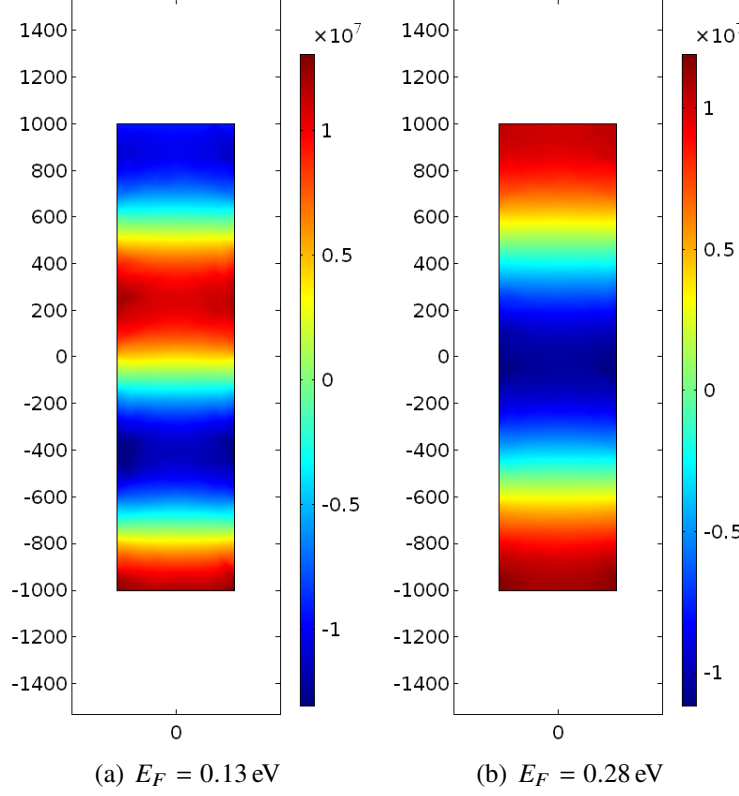


Fig. 2: Electric field distribution over a graphene-based waveguide at $f_c=4 \text{ THz}$, for different Fermi energies, E_F ($L=2 \mu\text{m}$, $d=90 \text{ nm}$).

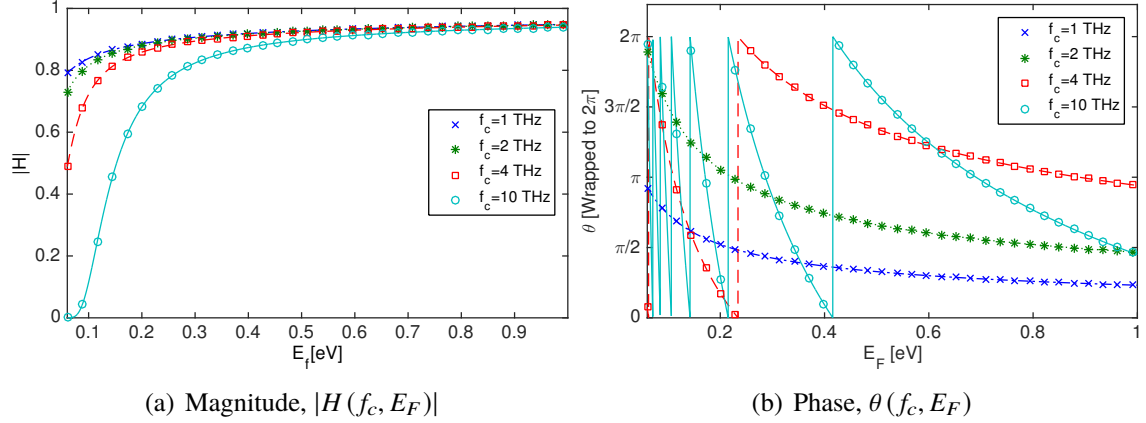


Fig. 3: Frequency response of the phase modulator, as a function of the Fermi energy, E_F , for different carrier frequencies f_c ($L=2 \mu\text{m}$, $d=90 \text{ nm}$).

3.3.3 Discussion

As part of this effort, we have proposed a novel graphene-based plasmonic phase modulator scheme for THz-band communication. The proposed modulator leverages the possibility to tune the propagation speed and, thus, output phase of a SPP wave as its propagates over a graphene

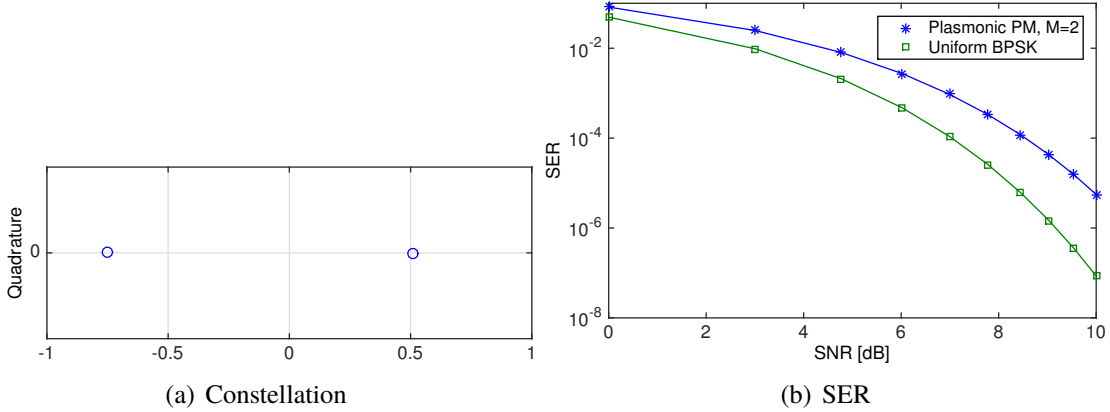


Fig. 4: Performance of a binary plasmonic phase modulator with $E_{F,0} = 0.28$ eV, $E_{F,1} = 0.13$ eV, ($f_c=4$ THz, $L=2$ μ m, $d=90$ nm).

layer. We have developed an analytical model for the modulator by starting from the surface conductivity model of graphene and the dispersion equation of SPP waves in gated graphene structures. COMSOL Multi-physics has been utilized to validate the proposed model. We have then analyzed the performance of plasmonic modulator in terms of symbol error rate for the specific case of a digital binary phase shift keying modulation. The results have shown that, despite generating a non-uniform signal space constellation, the modulated symbols are sufficiently apart to be easily distinguishable. This highlights the potential of the proposed approach to enable practical wireless communication systems in the THz band.

4 GRAPHENE-BASED PLASMONIC NANO-ANTENNA ARRAYS

4.1 Motivation

After modulation, the propagating SPP wave needs to be radiated. As first shown in [53] by using the transmission line formalism, a graphene-based antenna just one micrometer long and several hundreds of nanometers wide can be designed to resonate in the THz-band. This frequency is two orders of magnitude lower than the resonance frequency of a metallic antenna with comparable dimensions. Nevertheless, there are several limitations in single-antenna systems that motivate the development of graphene-based nano-antenna arrays (Fig. 5) [25]. An array configuration would simultaneously solve some of the inherent roadblocks to THz communication while opening up many new possibilities. On the one hand, despite their individual efficiency, single nano-antennas suffer from limited available output power due to their very small size (a few μm^2). On the other hand, the THz band itself introduces significant losses in the form of spreading losses and attenuation due to molecular absorption. A THz band array can alleviate these problems by producing huge increases in gain due to power amplification and/or beamforming. In addition, large arrays introduce the possibility to take advantage of Multiple-Input and Multiple-Output (MIMO) communication schemes for both beamforming and spatial multiplexing.

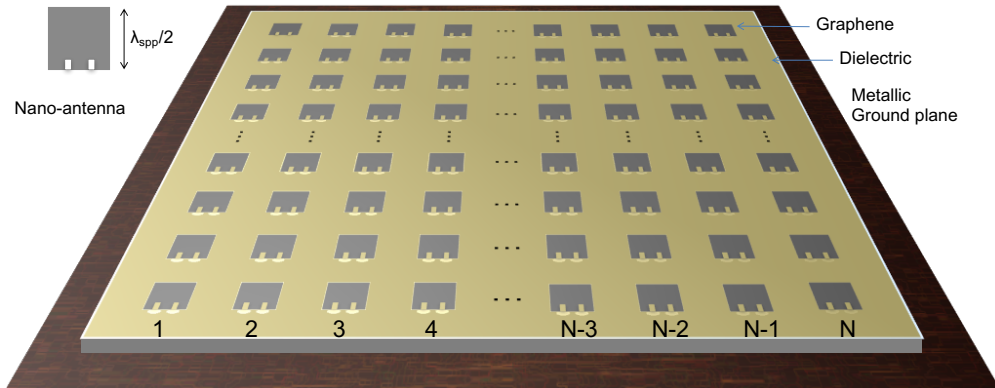


Fig. 5: Graphene-based plasmonic nano-antenna array.

In the design of a plasmonic nano-antenna array, there are two equally important challenges. First, the individual nano-antenna that serves as the basic element of the array must be designed. This has already been the subject of multiple works, starting with [53]. Since then, there have been many studies concerning graphene-based nano-antennas which investigate variations such as electrically tunable [49], reconfigurable [50], and beamforming antennas [54]. The second challenge is to determine how these individual elements should be placed relative to each other. Here mutual coupling concerns become just as important as individual design, as this determines how closely antennas can be placed and subsequently determines the size of the total array. Some works have been done in this area, but they are not sufficient or applicable to this case. For example, in [55] coupling is considered between graphene nanoribbons, but it does not consider how the distance between elements affects coupling strength and how it impacts system performance. Analysis is needed which considers coupling among nano-antennas.

As part of this project, we have developed the fundamental theory of graphene-based plasmonic nano-antenna arrays for THz communications. In particular, we have first analyzed the mutual

coupling between graphene-based nano-antennas (Sec. 4.2.1). More specifically, we have developed a mathematical analysis along with numerical simulations of a two-element array in order to understand how the strength of mutual coupling changes with respect to the separation between plasmonic elements. The second contribution has been an investigation of the performance of nano-antenna arrays in terms of the achievable gain and directivity (Sec. 4.3.1). In addition to the ideal gain, the impact of mutual coupling on the gain has been considered in our analysis. As before, the developed models have been validated by means of electromagnetic simulations with COMSOL Multi-physics (Sec. 4.4).

4.2 Methods, Assumptions and Procedures

4.2.1 Mutual Coupling Between Plasmonic Nano-Antennas

Coupled Mode Theory The coupling between two resonant modes, such as those excited in resonant plasmonic nano-antennas, can be described mathematically using coupled mode theory. A full coupled mode model of the nano-antenna consists of a resonator with terms for conduction losses, radiation losses, and incident power from outside waves. From [55], the amplitude of the fields in two such nano-antennas is given by:

$$\frac{d\tilde{a}_1}{dt} = (i\omega_1 - \gamma_1 - \Gamma_1)\tilde{a}_1 + ik\tilde{a}_2 + i\sqrt{\gamma_1}(s_+ + i\sqrt{\gamma_2}e^{-ikd}\tilde{a}_2), \quad (21)$$

$$\frac{d\tilde{a}_2}{dt} = (i\omega_2 - \gamma_2 - \Gamma_2)\tilde{a}_2 + ik\tilde{a}_1 + i\sqrt{\gamma_2}(s_+ + i\sqrt{\gamma_1}e^{-ikd}\tilde{a}_1), \quad (22)$$

where a_1 and a_2 refer to the amplitudes and ω_1 and ω_2 are the natural frequencies [56]. In addition, γ is the radiative loss, Γ is the conduction loss, k is the coupling coefficient, s_+ is an incoming plane wave, and $\tilde{a}_{1,2} = a_{1,2}e^{j\omega t}$. While this is physically the case, when the goal is to investigate the near field coupling the model is greatly simplified by considering only the case of two lossless resonators. This is possible because the radiative and conductive losses are purely real, and therefore do not affect the resonance conditions induced by the reactive fields. In addition, when nano-antenna separation distances are small enough the near field coupling effects dominate and the coupling due to re-radiation of energy can be assumed to be zero [55]. Therefore, we assume that $\Gamma = 0$, $\gamma = 0$, and $s_+ = 0$, and that the resonators are excited by a time varying function. In this case, the equations for the resonators are given as:

$$\frac{da_1}{dt} = j\omega_1 a_1 + k_{12} a_2, \quad (23)$$

$$\frac{da_2}{dt} = j\omega_2 a_2 + k_{21} a_1. \quad (24)$$

The theory is valid as long as the coupling perturbations can be considered linear, which is true if the coupling terms $k_{12}a_2$ and $k_{21}a_1$ are much smaller than $j\omega_1 a_1$ and $j\omega_2 a_2$. Due to the symmetry of the problem, as well as energy conservation constraints discussed in [56], k_{12} must be equal to k_{21} . By taking this system of linear equations, one can solve for the eigenfrequencies, resulting in:

$$\omega = \frac{\omega_1 + \omega_2}{2} \pm \sqrt{\left(\frac{\omega_1 - \omega_2}{2}\right)^2 + |k_{12}|^2}, \quad (25)$$

where all the terms have been previously defined.

Physically the eigenfrequencies can be understood as the natural resonant frequencies of the two nano-antennas. Because a nano-antenna is a passive component, if the natural resonance frequency changes the result is not that the antenna will change operating frequency, but rather that it will now only radiate efficiently at the new resonances. In a system where the nano-antennas are already being excited by a driving frequency, a change in the natural resonance will manifest itself as a change in the input impedance of the system. A typical array will be excited with the same frequency in each antenna. In this case, $\omega_1 = \omega_2 = \omega_0$, and the equation for the eigenfrequencies simplifies to

$$\omega = \omega_0 \pm k, \quad (26)$$

where k is the coupling coefficient.

4.3 Coupling Coefficient

The coupling coefficient is the result of the non-radiating near fields in the antenna and in conventional microstrip antenna theory it is derived from Maxwell's equations. There have been multiple attempts to model the mutual coupling between elements by using the transmission line model [57], the cavity model [58] [59] [60], or the method of moments for microstrip antennas. While these studies have had success in predicting coupling in metallic microstrip antennas, they have drawbacks which limit their use in studying coupling between plasmonic nano-antenna arrays. The problem is that most studies neglect surface waves to simplify the model. In a plasmonic nano-antenna, surface waves are critical to the operation of the antenna, and in fact are the only kind of waves that can be supported [19]. Even when studies account for surface waves, these surface waves are fundamentally different from SPP waves. The surface waves on metallic antennas occur at dielectric-dielectric boundaries and propagate over the entire dielectric surface. These waves detract from the total power available to be radiated. In contrast, a plasmonic nano-antenna relies on SPP waves for generating the electric field and are only supported on the boundary between a dielectric and a metal, which means they can only exist where the patch is present. Because of these differences, the models used for predicting the coupling coefficient in metallic antenna arrays cannot be assumed to work for plasmonic arrays. Further analysis is needed which takes into account the properties of SPP waves.

Because the wavelength in a plasmonic nano-antenna is confined to a much smaller length than the radiated free space wavelength, it is expected that the mutual coupling will only start to become a major factor at distances related to the plasmonic wavelength, and consequently allow array elements to be separated much less than would be required in a perfect electric conducting antenna. Taking this into consideration, we predict that the coupling coefficient can be approximated by an exponential function given as

$$k = \alpha \omega_0 e^{-d\beta}, \quad (27)$$

where ω_0 is the resonant frequency without coupling, α and β are tuning constants, and d is the separation distance between elements.

4.3.1 Performance of Plasmonic Nano-antenna Arrays

In the design of an array, it is important to consider the overall system performance and how it is impacted by coupling and other factors. An array constructed using graphene nano-antennas

will differ in two important aspects from a conventional array. First, as previously discussed, the coupling is expected to be based mainly on the physical size of the nano-antenna. For a plasmonic nano-antenna where there is a high confinement factor, near field coupling will only be an issue at distances much less than the free space wavelength. On one hand, this will allow for array elements to be placed much closer in proximity to each other, resulting in a high density of elements in the available area. On the other hand, this limits the beamforming abilities, which require distance comparable to the free space wavelength in order to achieve constructive superposition of field amplitudes. Second, the possibility to use one plasmonic signal source per antenna to power every element individually means that an increase in output power, and consequently gain, can be achieved independently of phase variation or beamforming. These differences are illustrated by considering the array factor \mathcal{AF} of a uniform square planar array with N powered elements per side, separated by a distance of λ , which is given in [61] by

$$\mathcal{AF}(\theta, \phi) = \left(\frac{\sin\left(N\frac{\psi_x}{2}\right)}{\sin\left(\frac{\psi_x}{2}\right)} \right) \left(\frac{\sin\left(N\frac{\psi_y}{2}\right)}{\sin\left(\frac{\psi_y}{2}\right)} \right), \quad (28)$$

$$\psi_x = kd \sin \theta \cos \phi - \frac{2\pi}{kd} \sin \theta_0 \cos \phi_0, \quad (29)$$

$$\psi_y = kd \sin \theta \sin \phi - \frac{2\pi}{kd} \sin \theta_0 \sin \phi_0, \quad (30)$$

where θ refers to the elevation angle, ϕ is the azimuth, (θ_0, ϕ_0) is the beam pointing direction, $k = \frac{2\pi}{\lambda}$ is the wavenumber, and d is the uniform distance between elements. In a conventional array \mathcal{AF} is normalized with respect to N to account for the total power being split between N antennas, and to better illustrate radiation pattern changes from field multiplication. However, here it is left unnormalized with respect to N due to the fact that the nano-antennas will be powered independently and contribute to the overall gain. In addition, for a plasmonic nano-antenna array the distance between the elements will be the plasmonic wavelength rather than some multiple of the freespace wavelength. In this case, we replace d with the plasmonic wavelength λ_{spp} , and the array factor becomes

$$\mathcal{AF}(\theta, \phi) = \left(\frac{\sin\left(N\frac{\psi_x}{2}\right)}{\sin\left(\frac{\psi_x}{2}\right)} \right) \left(\frac{\sin\left(N\frac{\psi_y}{2}\right)}{\sin\left(\frac{\psi_y}{2}\right)} \right), \quad (31)$$

$$\psi_x = \frac{2\pi}{\gamma} \sin \theta \cos \phi - \frac{2\pi}{\gamma} \sin \theta_0 \cos \phi_0, \quad (32)$$

$$\psi_y = \frac{2\pi}{\gamma} \sin \theta \sin \phi - \frac{2\pi}{\gamma} \sin \theta_0 \sin \phi_0, \quad (33)$$

where γ is the confinement factor and is equal to $\frac{\lambda}{\lambda_{\text{spp}}}$. When using this formula it is clear that the higher the confinement factor becomes, the lower the directivity will be, although it still has a minimum value of 1. However, analysis using this formula suggests that even with decreased directivity due to a high confinement factor, or equivalently, close element spacing, the attainable gain is still high due to power multiplication.

Table 1: Curve fitted Parameters for k

Frequency	1 THz	5 THz	8 THz
α	0.02563	0.02158	0.02188
β	$1e10^{-11}$	$1e10^{-11}$	$1e10^{-11}$

4.4 Results and Discussions

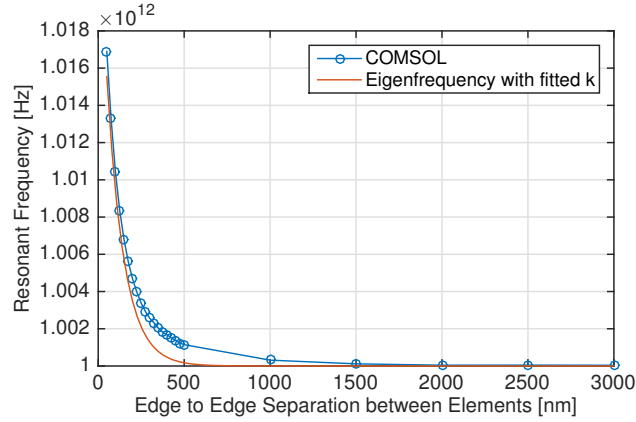
In this section, the analytical model for the mutual coupling coefficient is validated, and the nano-antenna array performance claims are verified by means of full-wave electromagnetic simulations. In order to numerically find the coupling coefficient, a two element array is simulated using COMSOL Multiphysics. Graphene is modeled as a transition boundary condition with complex-valued dynamic conductivity given by the model in [27], where $\tau_g = 0.5$ ps is the relaxation time of electrons in graphene, $T = 300$ K is the temperature, and with E_F values from 0.1 to 1.25 eV, where E_F is the Fermi energy of the graphene patch. These values are based on analysis of Raman spectra obtained from CVD-grown graphene. The graphene layer rests on top of a 90-nm-thick SiO_2 dielectric ($\epsilon_r = 4$), which separates the graphene from the ground plane. This thickness is chosen because it maximizes visual detection of graphene on SiO_2 . The antenna is fed with a lumped port that connects the graphene layer to the ground plane on one side. A perfectly matched layer and scattering boundary are used to accurately approximate an infinite space. The antennas are meshed with a resolution of $\lambda_{spp}/5$. To simulate the array performance measures of gain and directivity, the same parameters are used to construct a uniform planar three by three array for a total of nine elements.

4.4.1 Simulation Validation of Mutual Coupling

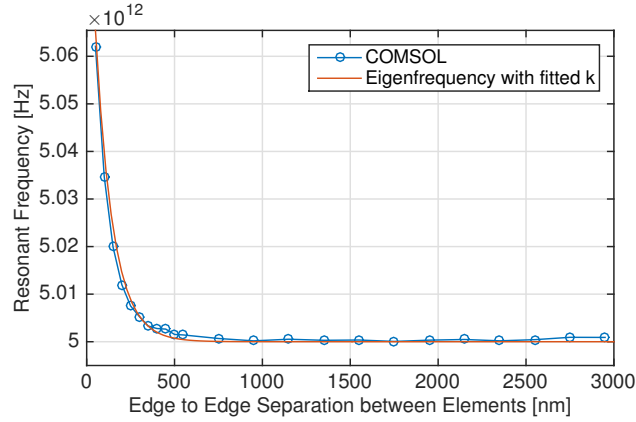
The effect of mutual coupling on resonant frequency was found through the measurement of the input impedance at the ports. As previously discussed, the frequency at which the imaginary part of the input impedance disappears is considered to be the resonant frequency. The mutual coupling dependency on the separation of the elements was found by performing a frequency sweep for different separation distances for three different frequencies that are representative of the THz band. The coupling coefficient (27) was also plotted using curve fitting tools to match the tuning parameters. As shown in Fig. 6, the change in frequency as a function of separation distance is comparable to the plasmonic wavelength, which in this case is 2 μm for both simulations. It also shows that the matched coupling coefficient equations are well matched to their respective coupling sweeps. Table 1 summarizes the matched coefficients for each frequency.

4.4.2 Numerical Analysis of Array Performance

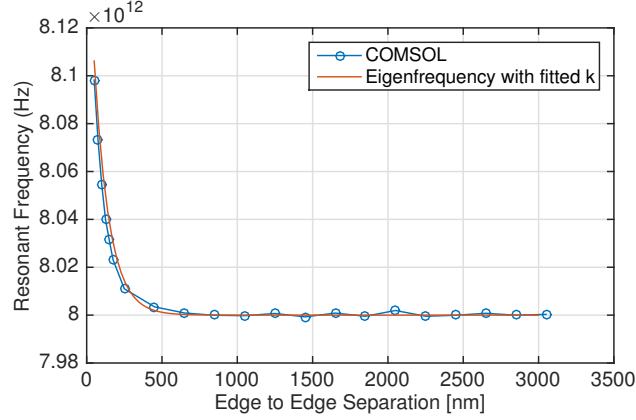
In addition to studying the change in frequency in a two element array, the overall array performance and the impact of mutual coupling on this performance was simulated. The simulation used a nine element array, and directivity and gain are calculated from radiated power values computed by COMSOL. The directivity as plotted in Fig. 7a takes into account the combined effects of the array directivity and the single nano-antenna's directivity, while neglecting power amplification. What can be seen from the graph is that the directivity when the antenna separation distance is comparable to λ_{spp} is predominately due to the directivity of the single nano-antenna, which is about



(a) Plasmonic Array Resonant Frequency at 1 THz



(b) Plasmonic Array Resonant Frequency at 5 THz

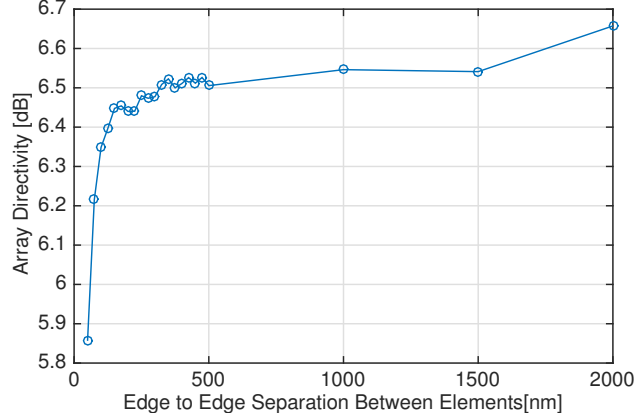


(c) Plasmonic Array Resonant Frequency at 8 THz

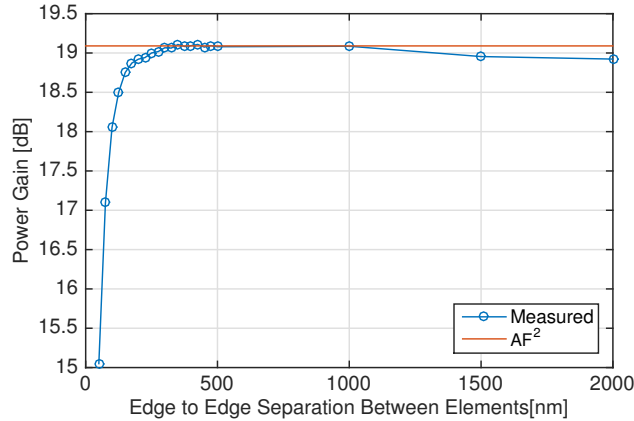
Fig. 6: Resonance frequency as a function of the separation distance between resonant elements for different antenna resonant frequencies.

6.5 dB. The added directivity from the array due to constructive interference does not occur until the separation approaches $\lambda/2$. In Fig. 7b, the power multiplication gain of the array over that of a single nano-antenna is plotted. This gain in power is shown to be equal in magnitude to the square

of the array factor, which for an array of nine elements is equivalent to 81, or about 19 dB. In both figures it is clear that mutual coupling effects cause a large drop in both directivity and power gain, but only for very close separation distances.



(a) Plasmonic Array Directivity at 8 THz



(b) Plasmonic Array Power Gain at 8 THz

Fig. 7: Directivity and power gain of a nine antenna uniform planar array as functions of the separation between elements.

Finally, in Fig. 8, the total gain of a plasmonic array is calculated based on the number of antennas in the array for different separation distances. The total gain shown here represents the maximum radiated power of a plasmonic array compared to that of a single isotropic nano-antenna and includes the directivity of a graphene nano-antenna, the directivity of the array, and the power multiplication from multiple powered antennas. It is important to note that even the lowest separation distance shown here is large enough that mutual coupling effects are not a concern.

4.4.3 Discussion

As part of this effort, we have analyzed the performance of graphene-based plasmonic nano-antenna arrays at THz frequencies, by taking the impact of mutual coupling into account. Coupled mode theory has been utilized to model the mutual coupling between two neighboring plasmonic nano-antennas and the coupling coefficient has been defined. The resulting gain of an active plasmonic

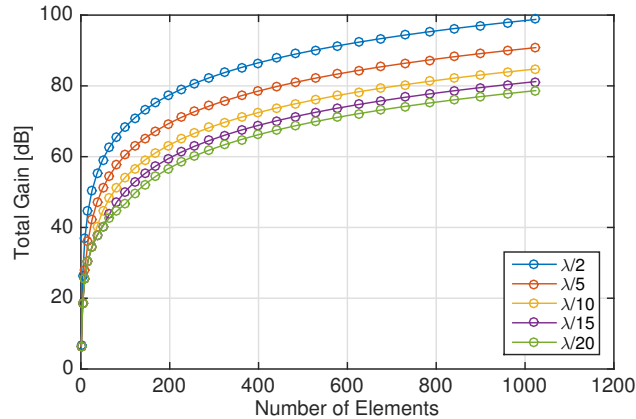


Fig. 8: Total gain of a graphene-based plasmonic nano-antenna array, as a function of the number of elements.

nano-antenna array has been derived, and finite-element simulations have been utilized to both validate the models and numerically explore the performance of plasmonic nano-antenna arrays. It has been shown that near field coupling between antennas becomes negligible at separation distances much less than the free space wavelength. Consequently, a very large number of elements can be integrated in plasmonic nano-antenna arrays with a resulting very small footprint and, potentially, lead to practical THz communication systems.

5 MULTI-USER INTERFERENCE MODELING IN THE THZ BAND

5.1 Motivation

As mentioned in the introduction, the THz band provides wireless communication devices with an unprecedentedly large bandwidth, ranging from several tens of GHz up to a few THz [23, 62]. The main phenomenon affecting the propagation of THz-band signals is the absorption by water vapor molecules. For communication distances below 1 m, where the number of molecules found along the path is small, the THz band behaves as a single transmission window several THz wide. In this scenario, the transmission of one-hundred-femtosecond-long pulses by following an on-off keying modulation spread in time has been recently proposed [63]. The power spectral density (PSD) of such pulses, which can be generated and detected by means of different electronic, photonic and plasmonic devices, has its main frequency components under 4 THz. By utilizing an on-off keying modulation, the transmitter can reduce its energy consumption by remaining silent during the transmission of logical “0s”, and by spreading the transmission of the pulses in time, concurrent transmissions can be multiplexed in time.

The transmission of ultra-short pulses minimizes the probability of collisions due to the very small time that the channel is occupied by each user. However, given that many of the envisioned applications of THz-band communications involve very large node densities (e.g., wireless nanosensor networks or networks on chip), multi-user interference results unavoidably. Many stochastic models of interference have been developed to date [64–66]. However, these models do not capture the peculiarities of the THz band channel, such as the molecular absorption loss. More recently, new interference models for THz-band communication have been developed [63, 67]. However, these models do not take into account the specific waveforms that are being transmitted (e.g., Gaussian-shaped pulses), and, in addition, no experimental validation for any of the models exists to date.

As part of this effort, we have developed a stochastic model of multi-user interference in pulse-based THz-band communications and experimentally validated it. This model is developed by considering the fact that the interference power at the receiver is not a combination of the received powers from the individual nodes, rather the power of the combination of the signal amplitudes. For this, first, we obtained the probability density function (PDF) of the interference generated by one interfering node at the receiver, starting from the PDFs of the pulse received energy and the PDF of the pulse shape. Then, we extended this model to account for multiple nodes which can constructively or destructively interfere. Finally, we validated the model by comparing the results to experimental measurements. Next, in Sec. 5.2.1, we describe the system model. The stochastic model of multi-user interference is developed in Sec. 5.2.2. Finally, we describe our experimental setup, validate the analytical model and provide numerical results in Sec. 5.3.

5.2 Methods, Assumptions and Procedures

5.2.1 System Model

To model the multi-user interference, we first need to take into account both the spatial distribution of the nodes as well as their temporal activity. In this section, we describe the system model utilized in the paper.

Network Topology We consider that nodes are randomly distributed in space by following a spatial Poisson process with rate λ . Without losing generality, we consider that the intended receiver is located at the center of a disc of radius a and area $A = \pi a^2$. The probability of finding k nodes in the disc is given by

$$P(k \in A) = \frac{(\lambda \pi a^2)^k}{k!} e^{-\lambda \pi a^2}. \quad (34)$$

Under the Poisson assumption, the locations of the nodes follow independent and identically distributed uniform distributions. If d is the distance to the origin from a point that is uniformly distributed in A , then the PDF of the distance distribution D is given by

$$f_D(d) = \begin{cases} \frac{2d}{a^2} & \text{for } 0 < d < a \\ 0 & \text{otherwise.} \end{cases} \quad (35)$$

Physical and Link Layers We consider that nodes communicate by utilizing TS-OOK [63]. In this scheme, a symbol “1” is sent by transmitting a hundred-femtosecond long pulse and a symbol “0” is sent by silence, i.e., a node does not transmit anything (Fig. 9). The time between symbols T_s is much longer than the symbol duration T_p , i.e., $\beta = T_s/T_p \gg 1$.

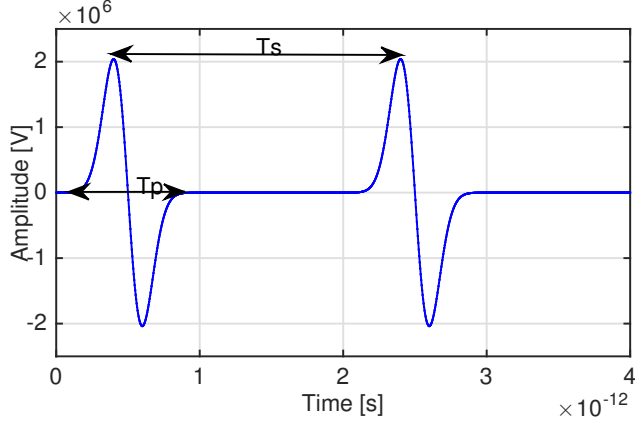


Fig. 9: Illustration of a TS-OOK transmission.

The pulses in TS-OOK are usually modeled as Gaussian-shaped. More specifically, the radiated pulses $s(t)$ resemble the first time derivative of a Gaussian pulse,

$$s(t) = \frac{dx(t)}{dt} = -\frac{(t - \mu)}{\sigma^2} x(t), \text{ with} \quad (36)$$

$$x(t) = a_0 \frac{e^{-\frac{(t-\mu)^2}{2\sigma^2}}}{\sqrt{2\pi}\sigma}, \quad (37)$$

where a_0 is a normalizing constant to adjust the pulse total energy, σ is the standard deviation of the Gaussian pulse in seconds, and μ is the center of the pulse in time, given in seconds. The total length of the radiated pulses $s(t)$ is approximately $T_p = 7\sigma$.

TS-OOK enables robust and concurrent communication among nodes. In the envisioned scenarios, nodes can start transmitting at any time without being synchronized or controlled by any

type of network central entity. However, due to the fact that the time between transmissions T_s is much longer than the pulse duration T_p , several nodes can concurrently use the channel without necessarily affecting each other. In addition, the very short symbol duration T_p makes collisions between symbols highly unlikely. However, as the number of communicating nodes increases, interference becomes a problem, as we show in the next section.

5.2.2 Interference Model

In the existing interference models, the total interference power at the receiver is obtained as the addition of the interference power from each node. However, by considering the received signal power instead of the received signal amplitude, the fact that interference can be either constructive or destructive is effectively neglected. This usually results in unrealistically large values of interference, specially when the transmitted signals have large fluctuations between positive and negative amplitude values. Our analytic model overcomes this limitation by taking into account both the signal waveform as well as the THz-band channel. We taylor our model to Gaussian-shaped pulses, but the same methodology could be utilized for any other waveform.

In order to characterize the interference, we observe the signals at the receiver. For the system model described in Sec. 5.2.1, the signal $y(t)$ at the receiver can be written as

$$y(t) = \sum_{u=1}^U (s(t - \tau_u)) * h(t, d_u) + n(t), \quad (38)$$

where U is the total number of nodes in the network, $s(t - \tau_u)$ is the transmitted signal along with the delay τ_u , $h(t, d_u)$ is the system impulse response, $*$ denotes convolution, and $n(t)$ is the noise at the receiver. The system impulse response $h(t, d_u)$ captures the impact of the THz-band channel, and is obtained as in [63].

If we consider the signal from user $u = 1$ as the intended signal, the total interference is given by

$$i(t) = \sum_{u=2}^U i_u(t), \quad (39)$$

where $i_u(t)$ is the interference at receiver due to each node u . By focusing on one specific symbol, without losing generality, $i_u(t)$ can be written as

$$i_u(t) = \sqrt{e_{p,u}} p(t - \tau_{t,u}), \quad (40)$$

where $e_{p,u}$ stands for the energy of the received pulse, $p(t)$ is the shape of the pulse with unitary energy, and $\tau_{t,u}$ refers to the total delay (initial delay and propagation delay).

Given that nodes are randomly distributed in space and uncoordinatedly transmitting in time, the PDF of the interference distribution I_u generated by a node u can be modeled as a function of two random variables, namely, the energy of the pulse, with distribution E_p , and the shape of the pulse, with distribution P .

On the one hand, the energy of the pulse depends on the transmitted pulse energy, which we consider a parameter in our analysis, and the distance between the nodes, which is a random variable D with PDF given by (35). Therefore, the PDF of E_p can be derived from the PDF of D as follows:

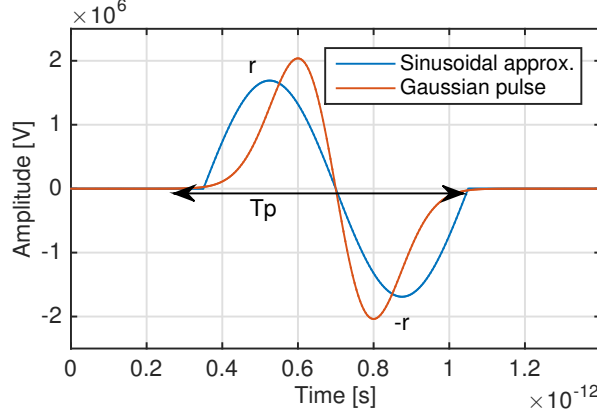


Fig. 10: Sinusoidal approximation of the transmitted pulse in TS-OOK.

$$f_{E_p} = \frac{f_D(f^{-1}(e_p))}{f'(f^{-1}(e_p))}, \quad (41)$$

where f^{-1} denotes the inverse and f' denotes the first derivative of e_p . The PDF of E_p can only be analytically obtained if $e_p(d)$ is invertible. For the distances considered in our analysis, it can be shown that the received energy can be approximated by the polynomial

$$e_p = \xi d^{-\eta}, \quad (42)$$

where ξ and η are two constants which depend on the specific channel molecular composition as well as on the energy and the shape of the transmitted signal. By computing the inverse function of (42), and combining it with (35) in (41), we obtain

$$f_{E_p}(e_p) = \begin{cases} \frac{2\xi^{\frac{2}{\eta}}}{a^2\eta} e_p^{-\frac{2+\eta}{\eta}} & \text{for } \xi a^{-\eta} < e_p < \infty \\ 0 & \text{otherwise.} \end{cases} \quad (43)$$

The step by step derivation is methodological and has been omitted due to space constraints. Finally, the interference from a node depends on the amplitude of the received pulse, not its energy. If we define $e_s = \sqrt{e_p}$, the PDF of E_s is now given by

$$f_{E_s}(e_s) = \begin{cases} \frac{4\xi^{2/\eta} |e_s|^{-\frac{\eta+4}{\eta}}}{a^2\eta} & \text{for } \sqrt{\xi a^{-\eta}} < e_s < \infty \\ 0 & \text{otherwise.} \end{cases} \quad (44)$$

On the other hand, in order to capture the constructive or destructive addition of the interference at the receiver, we need to take into account the shape of the transmitted pulse, which is deterministic, and the time instant at which it reaches the receiver, which we model as a random variable T with uniform distribution over the duration between two symbols T_s ,

$$f_T(t) = \begin{cases} \frac{1}{T_s} & \text{for } 0 < t < T_s \\ 0 & \text{otherwise.} \end{cases} \quad (45)$$

As before, to obtain the PDF of P , we need to first obtain the inverse function of $p(t)$, which in this case is given by (37). However, this cannot be obtained in closed form expression. To overcome this limitation, we approximate the transmitted pulse with a shifted sinusoidal pulse of same duration T_p , as shown in Fig. 10. This pulse can be expressed mathematically as follows

$$p(t) = r \sin\left(\frac{2\pi}{T_p}\left(t - \frac{T_p}{2}\right)\right), \quad (46)$$

where $r = \sqrt{\frac{2}{T_p}}$ is the amplitude of the sinusoid normalized to have unit energy. The inverse function of this new pulse can be written as

$$t = f^{-1}(p) = \frac{T_p}{2\pi} \sin^{-1}\left(\frac{p}{r}\right) + \frac{T_p}{2}. \quad (47)$$

Now the PDF of P can be derived from the PDF of T similarly as for E_P , yielding to

$$f_P(p) = \begin{cases} \frac{T_p}{T_s \pi r \sqrt{1 - \frac{p^2}{r^2}}} & \text{for } -r < p < r \\ 0 & \text{otherwise.} \end{cases} \quad (48)$$

Note that the above PDF integrates to $\frac{T_p}{T_s}$, not 1. This is because the pulse p has nonzero values only within a duration of T_p . For rest of the time $1 - \frac{T_p}{T_s}$, the signal value is zero. Hence, we express the PDF of P as a mixed distribution

$$f_P(p) = \frac{T_p}{T_s \pi r \sqrt{1 - \frac{p^2}{r^2}}} + \left(1 - \frac{T_p}{T_s}\right) \delta(p), \quad (49)$$

where δ stands for the Dirac-delta function.

Since the interference generated by one user is the product of two random variables E_s and P , its PDF can be determined from their PDFs as follows:

$$f_{I_u}(i_u) = \int_{-\infty}^{\infty} f_P(p) f_{E_s}\left(\frac{i_u}{p}\right) \frac{1}{p} dp. \quad (50)$$

By replacing the PDFs from (44) and (49) in (50), the PDF of I_u is obtained (51), where $\Gamma()$, $B()$, and ${}_2F_1()$ are the standard Gamma, Beta and Hyper-geometric functions:

$$f_{I_u}(i_u) = \left(1 - \frac{T_p}{T_s}\right) \delta(i_u) + \begin{cases} \frac{T_p \xi^{2/\eta} r^{4/\eta} \Gamma\left(\frac{1}{2} + \frac{2}{\eta}\right) |i_u|^{-\frac{\eta+4}{\eta}}}{\sqrt{\pi} a^2 T_s \Gamma\left(\frac{2}{\eta}\right)} & \text{for } i_u < \sqrt{\xi} r (-a^{-\eta/2}) \vee i_u > \sqrt{\xi} r a^{-\eta/2} \\ -\frac{2 T_p \xi^{2/\eta} \left(-\frac{r}{i_u}\right)^{4/\eta} B_{\frac{a^\eta i_u^2}{\xi r^2}}\left(\frac{1}{2} + \frac{2}{\eta}, \frac{1}{2}\right)}{\pi a^2 \eta T_s i_u} & \text{for } \sqrt{\xi} r (-a^{-\eta/2}) < i_u < 0 \\ \frac{4 T_p a^{\eta/2} {}_2F_1\left(\frac{1}{2}, \frac{1}{2} + \frac{2}{\eta}; \frac{3}{2} + \frac{2}{\eta}; \frac{a^\eta i_u^2}{\xi r^2}\right)}{\sqrt{\xi} (\pi \eta r T_s + 4 \pi r T_s)} & \text{for } 0 < i_u < \sqrt{\xi} r a^{-\eta/2} \\ 0 & \text{otherwise} \end{cases} \quad (51)$$

Since the signals from individual nodes add up at the receiver and are independent, the PDF of the total interference can be determined by the convolution of the individual PDFs:

$$f_I(i) = f_{I_1}(i_1) * f_{I_2}(i_2) * f_{I_3}(i_3) * \dots * f_{I_U}(i_U). \quad (52)$$

To calculate the n-fold convolution on the right hand side, we go into transform domain. We define the characteristic function of the interference from node u as

$$\phi_u(\omega) = E[e^{j\omega i_u}]. \quad (53)$$

Since the interferences from nodes are independent and identically distributed random variables, they have the same characteristic function. The convolution becomes a product in the transform domain and, thus, the characteristic function of the interference can be written as

$$\phi(\omega) = (\phi_u(\omega))^U. \quad (54)$$

Now the PDF of the total interference can be found by taking the inverse transform of $\phi(\omega)$:

$$f_I(i) = F^{-1}\{\phi(\omega)\}. \quad (55)$$

Unfortunately, this characteristic function cannot be analytically derived in closed form, and, thus, we numerically obtain it in the next section.

5.3 Results and Discussions

5.3.1 Experimental Setup

In order to experimentally emulate THz communication signals emanating from multiple THz nodes, we utilize a THz time-domain spectroscopy (THz-TDS) system combined with an innovative interference generating setup (Fig. 11). In particular, a collimated 3 cm wide THz-TDS beam is used to illuminate a row of metal rods. The metallic rods are 1 mm in diameter and can effectively reflect the THz pulses. Therefore, each rod effectively represents an interferer at a different distance.

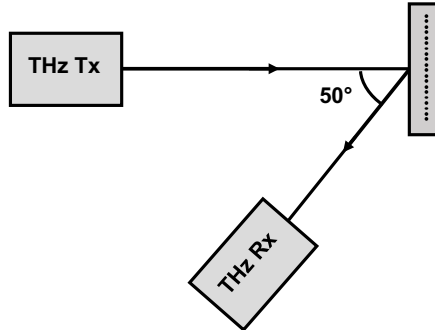


Fig. 11: Illustration of the THz beam from the transmitter (Tx) to receiver (Rx) via reflections from the metal rods, which emulate interference from multiple nodes.

For the measurements, an apparatus (Fig. 12) was created to hold up to 20 metal rods in place, linearly. The THz transmitter is positioned so that the THz beam is centered at position 13, 27.5 cm

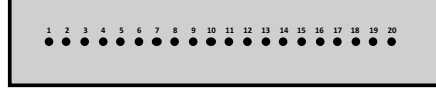


Fig. 12: Top view of the linear apparatus that holds the metal rods in place.

away. The receiver is set at 50 degrees from the transmitter at a distance of 14.5 cm away from a metal rod in position 13 (Fig. 11). Reflected pulse obtained by the receiver shows the presence of a metal rod. Data is collected by taking scans of the metal rods placed in specific positions and obtaining the results in the time domain. Fig. 13 shows the THz time domain waveform for the reflection off of one metal rod in position 13.

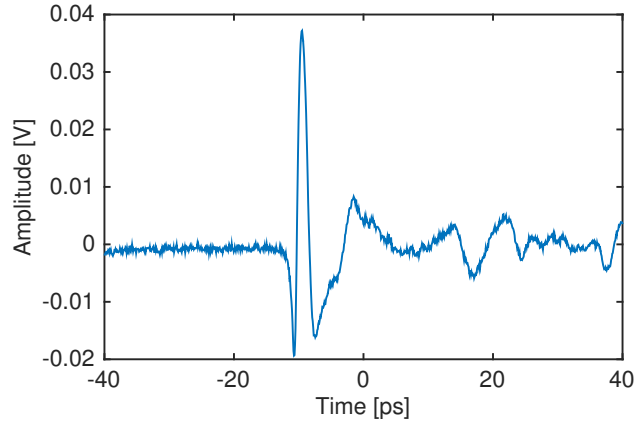


Fig. 13: THz pulse from the reflection off of one metal rod in position 13.

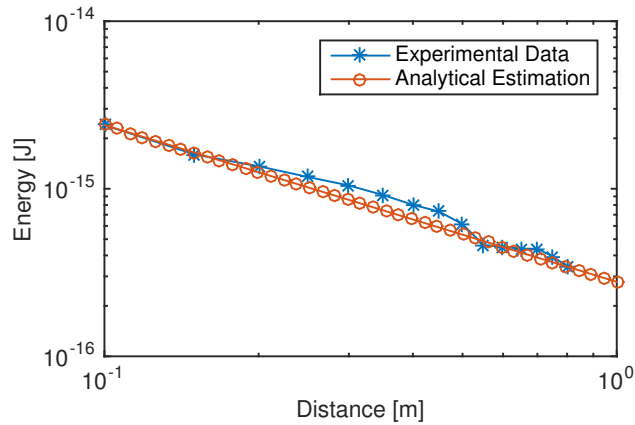


Fig. 14: Measured and approximated received pulse energy as functions of the transmission distance.

Fig. 14 shows the received energy versus distance curve for the measurements taken in the above described setup. A curve fitting was done to determine the ξ and η values from the experimental data and has been found to be 3.7820e-16 and 0.9357 respectively. The value of η confirms the cylindrical spreading of the signal as it was collimated in the experimental setup. These extracted parameter values have then been used in the analytical model to generate the PDF of the interference for different number of nodes in the network. The other parameters of the model have been chosen to match the experimental setup. For example, $T_p = 8$ ps has been approximated from

the radiated pulse duration, $\beta=10$ has been chosen to match the observation period of the measured signal. Also, $a = 0.8$ m was chosen to reflect the experimental setup and $r = \sqrt{\frac{2}{T_p}}$ to ensure the pulse unit energy.

5.3.2 Single Interferer Model Validation

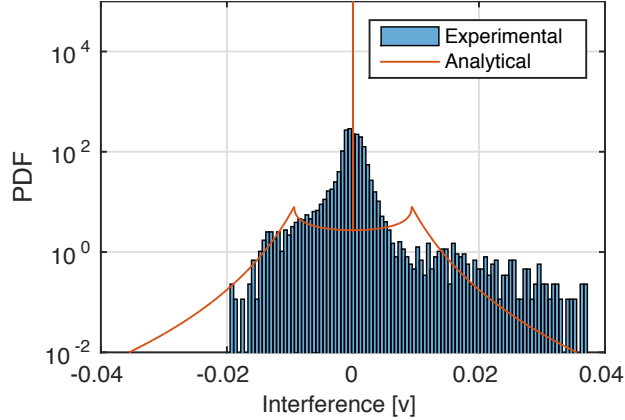


Fig. 15: Interference distribution of a single interferer.

Fig. 15 shows the the probability distribution function of the interference for both experimental and analytical case when there is a single interferer in the network. As expected, most of the probability mass is concentrated at zero as shown by the impulse at the center. The impulse was cut to show the graph of the distribution clearly. It can also be seen from the figure that the experimental data has a lot of samples near zero whereas the analytical model doesn't. The reason for this is that there is inevitable noise in the experiment and we haven't considered the noise in our analytical

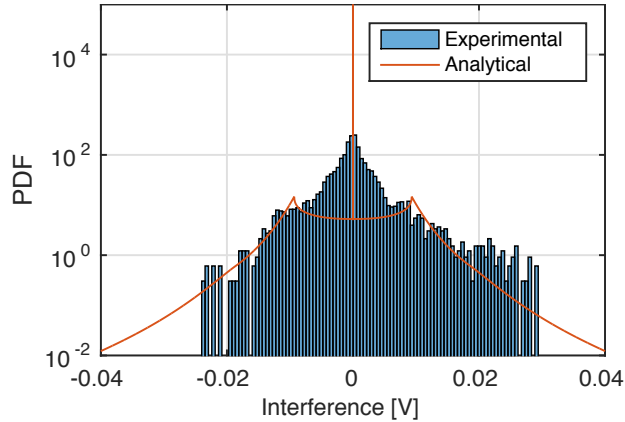


Fig. 16: Interference distribution of two interferers.

model. Also, we couldn't take measurements below 5 cm distance between the transmitter and receiver due to the experimental set up limitations. Nevertheless, the distribution from the analytical model and experimental data follows similar trend. It can reasonably be said that, as the number of measurements is increased and the distances are picked randomly, the experimental PDF will more closely follow the analytical model.

5.3.3 Multiple Interferer Model Validation

Fig. 16 compares the interference PDFs from analytical model and experimental data for two interferers in the network. It can be seen that they match much better than the single interferer case. The reason is that the measurements were taken by putting two rods at random locations in the linear apparatus which essentially created randomness in the distance between transmitter and the receiver. Fig. 17 shows that the interference spreads away from the 0 value as the number of interferer increases in the network. In addition, the height of the impulse is also decreased, reducing the chance of zero interference. For large number of interferers, the PDF converges to a Gaussian PDF as expected from the Central Limit theorem, and originally shown for TS-OOK in [63].

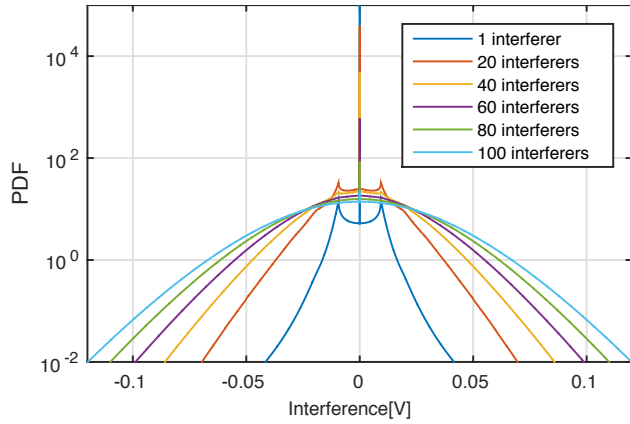


Fig. 17: Illustration of PDF converging to Gaussian with increasing number of nodes.

5.3.4 Discussion

An stochastic model for short range pulse-based THz-band communication network has been presented considering the fact that interference occurs with the amplitude of the signal, not the power. The PDF of the interference has been analytically deduced from the PDFs of the energy and the pulse. In addition, it has been compared with experimental data to validate the model. The results show similarity in spite of the limitation we had in the experimental set up and noise modeling. It has also been shown that the PDF converges to a Gaussian distribution as the number of nodes increases in the network.

6 TERAHERTZ SYMBOL DETECTION AND PHYSICAL LAYER SYNCHRONIZATION

6.1 Motivation

Independently of interference, one of the main challenges with ultra-high-speed pulse-based communications is the need for tight symbol synchronization between transmitter and receiver. Physical-layer synchronization affects the successful symbol detection probability and impacts the overall link performance. Unfortunately, we cannot directly reuse the existing solutions for similar pulse-based communication systems, such as Impulse-Radio Ultra Wide Band (IR-UWB) communications or Free Space Optical systems (FSO) [68–70]. One of the main reasons for this is the very short duration of THz pulses, which require the use of very high-speed Analog-to-Digital Converters (ADCs) for synchronization and symbol detection. The fastest existing ADC to date can only sample at rates below 100 Giga-Samples-per-second (GSas) [71], much below the Nyquist rate for THz signals. Furthermore, its size and power consumption make it inadequate for nano-devices. In addition to the lack of ADCs, the local clock [72] at different nano-devices might oscillate at slightly different frequencies, which can result in a significant clock skew between the transmitter and the receiver.

As part of this effort, we have developed a new synchronization scheme for pulse-based THz-band communication, which is based on dynamically time-shifting the signal at the receiver by means of a voltage-controlled delay (VCD) line [73] and adapting the observation window of a Continuous-Time Moving-Average (CTMA) symbol detector [74]. The fundamental idea is that, during an initial synchronization preamble, a synchronization block, which is composed by a bunch of VCD lines and CTMA detectors, is used to iteratively determine the symbol start time and observation window length that is then used for the detection of the data symbols in the packet.

Next, we first describe and analyze the accuracy of the synchronization block and provide closed-form expressions for the number of bits in the preamble necessary to achieve synchronization, which depends on the number of elements in the synchronization block as well as the clock skew between transmitter and receiver (Sec. 6.2.1). Then, we analyze the successful symbol detection probability of the CTMA symbol detector as a function of the observation window length determined from the synchronization block (Sec. 6.2.2). In addition, we investigate the impact of the synchronization and symbol detection blocks on the achievable link throughput, and identify the optimal parameter values for their design (Sec. 6.2.3). Moreover, we validate and test the scheme with experimental data obtained with a THz time-domain spectroscopy platform, and provide extensive numerical results to support our developed solution (Sec. 6.3).

6.2 Methods, Assumptions and Procedures

6.2.1 System Model and Synchronization Algorithm

In our scenario, we consider that nodes communicate in an uncoordinated fashion and by utilizing TS-OOK modulation. The main objective of our proposed synchronization scheme is to jointly determine the symbol start time and the observation window length, by successively narrowing down the integration window around the true location of the pulse. More specifically, we consider that each packet incorporates a synchronization preamble composed of a pre-established sequence

of logical zeros and ones. During the preamble, the synchronization block iteratively adapts the delay of the pulses at the receiver by means of a VCD line, which could be implemented for example by means of a graphene-based plasmonic waveguide [73]. The working principle of this VCD is based on the property that the propagation speed of a SPP wave on a graphene waveguide can be dynamically changed by electrically modulating the Fermi energy of the graphene layer [75]. This result is leveraged in our proposed design to change the signal propagation delay between the antenna and the symbol detector. In our design, we consider a CTMA detector, which outperforms energy-based detectors in terms of sensitivity [74] (see Sec. 6.2.2).

The proposed synchronization scheme, illustrated in Fig. 18, can be implemented with an array of VCD lines and CTMA detectors and a single control logic circuit. Next, we describe the iterative procedure by which the symbol start time and observation window length are jointly determined.

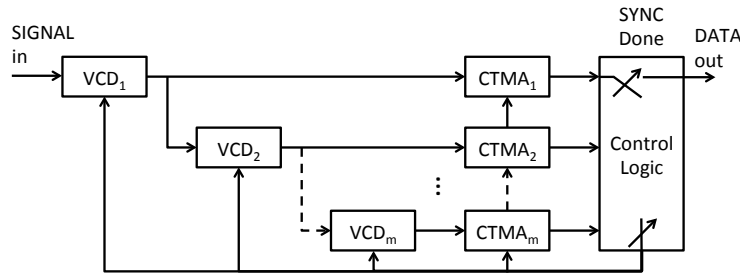


Fig. 18: Synchronization block diagram.

Symbol Start Time and Observation Window Length Let m denote the number of channels or branches in the synchronization block shown in Fig. 18. Each branch is composed of a VCD line and a CTMA symbol detector, whose delay and observation window length, respectively, are dynamically adapted through the following iterative process.

Iteration 1: In the first iteration, the delay introduced by each VCD line is T_s/m and the CTMA observation window length is set to T_s/m . Together, all the CTMA detectors look for the pulse over the entire symbol time T_s . Based on this, the output of the first CTMA detector is equal to one only when the pulse is located between $[(m-1)T_s/m, T_s]$. Similarly, the output of the second CTMA detector is equal to one only when the pulse is located between $[(m-2)T_s/m, (m-1)T_s/m]$, and so on. The output of the last branch, m , is only equal to one when the pulse is located between $[0, T_s/m]$. We then define *block1* as the block where the pulse is present.

Iteration 2: In this iteration, each CTMA detector utilizes an observation window of duration T_s/m^2 . The first VCD line introduces a delay equal to $(block1 - 1)T_s/m + T_s/m^2$. The remaining VCD lines introduce a delay equal to T_s/m^2 . Thus, the total delay in the second line is equal to $(block1 - 1)T_s/m + 2T_s/m^2$. Similarly, the total delay in the third line is equal to $(block1 - 1)T_s/m + 3T_s/m^2$, and so on. We then define *block2* as the block where the pulse is found.

Iteration 3: In this iteration, each CTMA detector utilizes an observation window of duration T_s/m^3 . The first VCD line introduces a delay equal to $(block1 - 1)T_s/m + (block2 - 1)T_s/m^2 + T_s/m^3$. The remaining VCD lines introduce a delay equal to T_s/m^3 . Thus, the total delay in the second line is equal to $(block1 - 1)T_s/m + (block2 - 1)T_s/m^2 + 2T_s/m^3$. Similarly, the total delay in the third branch is equal to $(block1 - 1)T_s/m + (block2 - 1)T_s/m^2 + 3T_s/m^3$, and so on. We then define *block3* as the block where the pulse is found.

Having explained the logic behind the first three iterations, we can write a generalized formula for the estimated symbol start time T_d after the synchronization preamble:

$$T_d = \sum_{i=1}^{x-1} (block_i - 1) \frac{T_s}{m^i} + (block_x) \frac{T_s}{m^x}, \quad (56)$$

where m is the total number of branches in the synchronization block, x is the number of synchronization iterations and T_s is the symbol time. The maximum number of branches m is limited by the hardware constraints of nano-devices, and the number of iterations x depends on the length of the preamble bits sent by the transmitter. Both are considered parameter values in our analysis. Note there is no synchronization adjustment if the preamble bits are equal to zero.

Similarly, the observation window length T_{win} of the symbol detector after the synchronization preamble is given by

$$T_{win} = \frac{T_s}{m^x}, \quad (57)$$

and can also be written as a multiple of the pulse duration T_p

$$T_{win} = nT_p. \quad (58)$$

By combining (57) and (58), we can write n as

$$n = \frac{\beta}{m^x}, \quad (59)$$

where β is the spreading factor in TS-OOK.

From Fig. 18, once the synchronization phase is completed, we close the DATA out switch and disconnect the feedback to channels two to m . Hence, we can use the same block to capture the data by using only the first branch, with the VCD delay set to T_d and the observation window set to T_{win} .

Impact of Clock Skew The clock skew, or difference between the transmitter and receiver clock frequencies, introduces further synchronization challenges. In particular, a mismatch in the symbol rates between the two nodes might progressively move the symbols outside of the detector observation window. This sets an upper bound on the number of data bits that can be transmitted before a new synchronization phase is needed. In this section, we investigate such bound for different values of the clock skew. In our analysis, we define the clock skew from the receiver's perspective. In particular, we consider that the symbol time T_s varies for each sample n at a rate μ

$$T_s[n] = T_s[n-1](1 + \mu), \quad (60)$$

where μ can be either positive or negative. When μ is positive, the symbol period appears to increase with time, whereas when μ is negative, it appears to decrease.

Without loss of generality, we consider that, after the initial synchronization phase, the position p of the pulse within the observation window is characterized with a uniform random variable with probability density function (PDF) f_P given by

$$f_P(p) = \begin{cases} \frac{m^x}{T_s}, & \text{if } 0 < p < \frac{T_s}{m^x}, \\ 0, & \text{otherwise.} \end{cases} \quad (61)$$

Therefore, the expected pulse position is given by $\frac{T_s}{2m^x}$, or equivalently, $\frac{T_{win}}{2}$. The maximum number of bits n_{bits} to be transmitted before requiring a new synchronization phase is then computed as follows. When μ is positive, re-synchronization should happen before this condition is met

$$T_s[n] \geq T_s[0] + T_{win}/2 \quad (62)$$

where μ is the clock variation factor, T_s is the symbol time and T_p is the pulse time. By combining (62), (60) and (59), n_{bits} can be obtained as

$$T_s[0] \cdot (1 + \mu)^{n_{bits}} = (T_s[0] + T_{win}/2), \quad (63)$$

$$n_{bits} = \frac{\log_{10}(1 + \frac{1}{2m^x})}{\log_{10}(1 + \mu)}. \quad (64)$$

We can see that, as the value of μ increases, the number of bits after which re-synchronization should take place decreases, as expected. The same procedure can be followed to obtain the value of n_{bits} for $\mu < 0$, reaching the same equation for n_{bits} in (64), but with $|\mu|$ instead of μ .

6.2.2 Continuous-Time Moving-Average Detector

In this section, we describe and analytically model the performance of the CTMA symbol detector scheme, with a special emphasis on the impact of observation window T_{win} on the successful symbol detection probability.

Detector Overview Traditional energy-based symbol detector schemes for pulse-based communication integrate the received signal over the entire symbol time or, following our definition, over the observation window T_{win} . The output is then compared to a pre-defined threshold and a decision on the received symbol is made. However, as mentioned before, the signals radiated by individual nano-devices have a very low power and are affected by the THz-band channel path-loss. This results into very high Symbol Error Rate (SERs) in realistic scenarios.

To overcome such limitation, a CTMA symbol detector for THz pulses was first proposed in [74]. A revised block diagram for the CTMA symbol detector is shown in Fig. 19.

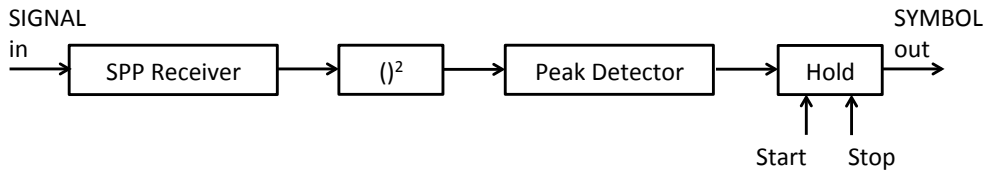


Fig. 19: CTMA symbol detector block diagram.

The fundamental idea behind this symbol detection scheme can be summarized as follows. When the detector integrates the pulse over a window T_{win} greater than the pulse time T_p , the noise contribution increases with T_{win} . This effect drops the performance of the receiver in terms of SER (Fig. 20(top)). To mitigate the impact of noise, we could reduce the integration time down to the pulse duration, T_p . However, since the observation window T_{win} is generally much larger than T_p , and we cannot know the exact position of the pulse within T_{win} , we would have to implement a total of T_{win}/T_p integrators in parallel and shifted in time to guarantee that the symbol is not missed. This

implementation is certainly impractical for low complexity devices. Additionally, the pulse may not perfectly fit in the integration time window (Fig. 20 (center)). Alternatively, we could just use a single integrator and move it in time at tiny steps $\Delta t \rightarrow 0$. This is the concept of a CTMA symbol detector (Fig. 20(bottom)).

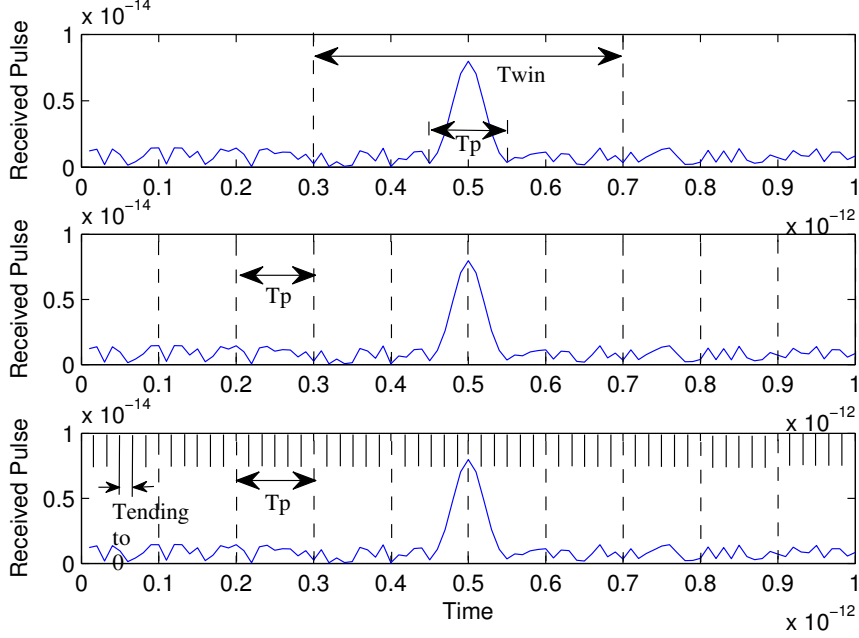


Fig. 20: Window length bigger than T_p (top); Window length equal to T_p , but pulse does not fit in a single integration window (center); Window length equal to T_p and pulse fits in a single integration window (bottom).

We define the CTMA detector as the linear time-invariant system with input to output relation given by

$$x(t) = \int_{t-T_p}^t v(t) dt, \quad (65)$$

where x stands for its output, t refers to time, T_p is the pulse time and v is the input signal to CTMA. As discussed in [74], the CTMA behaves as a low-pass filter and could be implemented with a discrete analog components. At each instant of time, the output of the CTMA, x is compared to a fixed threshold V_{th} , and the maximum value is held until the output is read and reset. The detector then decides whether the n -th symbol is one or zero according to:

$$s[n] = \begin{cases} 1, & \text{if } y = \max \{x(t)\} > V_{th}, \\ 0, & \text{otherwise,} \end{cases} \quad (66)$$

for $t \in [0, T_{win}]$. Next, we analytically investigate the successful symbol detection probability for both zeros and ones.

Detection of Zeros In TS-OOK, zero is transmitted as silence and, thus, only noise is detected at the receiver side. For this, we consider the detected signal to be composed of N identically distributed random variables. We define $\mathbf{X} = \{X_1, X_2, \dots, X_N\}$ as the vector that contains the N

random variables and we use X_i to refer to the random variable that represents the value of the input signal x at time t_i . N depends on the observation window length, T_{win} , the integration window length of the CTMA, which we consider to be equal to T_p , and the time step of the CTMA detector, z . From (59), N can be written as

$$N = \frac{n-1}{z} + 1. \quad (67)$$

Strictly speaking, $z \rightarrow 0$, as the CTMA is an analog detector and, thus, $N \rightarrow \infty$. Then, from (66), the output of the symbol detector is given by $Y = \max \{\mathbf{X}\}$. Therefore, the PDF $f_{Y,no}$ of the output can be obtained as a function of the PDFs for the individual variables X_i . In particular, it follows that

$$f_{Y,no}(y) = \frac{d}{dy} (F_{no}(y))^N = N F_{no}(y)^{N-1} f_{no}(y), \quad (68)$$

where f_{no} and F_{no} stand for the PDF and the Cumulative Distribution Function (CDF) for each one of the individual random variables. From [76], we consider that each individual variable follows a chi-square distribution and, thus,

$$f_{no}(y) = \frac{y^{(v-2)/2} e^{-(y/2)}}{2^{y/2} \Gamma(\frac{y}{2})}, \quad (69)$$

where $y = 2X/N_0$ is the normalized signal with respect to the noise two-sided power spectral density N_0 . $v = 2T_p B$ is the number of degrees of freedom, where T_p and B stand for the pulse duration and its equivalent bandwidth, and Γ refers to the Gamma function. Because we are using realistic THz pulses, which are further affected by the THz-band channel and the CTMA filter, the product $T_p B$ is generally larger than one and, thus, there is no closed form solution for (68).

Detection of Ones In TS-OOK, a logical one is transmitted as a one-hundred-femtosecond-long pulse. Following a similar methodology as before, we consider that the received signal is contributed by two kinds of random variables, some representing the pulse and some presenting noise. Hence, the output can be now represented as $Y = \max \{\mathbf{X}\} = \max \{\mathbf{X}_N, \mathbf{X}_S\}$, where \mathbf{X}_N and \mathbf{X}_S are vectors that contain N_n noise random variables and N_s signal random variables. As discussed in [74], provided that the signal power is kept higher than the noise power, $Y \approx \max \{\mathbf{X}_S\}$. Therefore, the PDF of the output $f_{Y,si}$ can be now written as

$$f_{Y,si}(y) = N_s F_{si}(y)^{N_s-1} f_{si}(y), \quad (70)$$

where now each variable X_i is modeled as non-central chi-square distribution with

$$f_{si}(y) = \frac{1}{2} \left(\frac{y}{\lambda} \right)^{\frac{v-2}{2}} e^{\frac{-(y+\lambda)}{4}} I_{\frac{v-2}{2}} \left(\sqrt{y\lambda} \right), \quad (71)$$

where $\lambda = \frac{2E}{N_o} = v SNR$, $v = 2T_p B$, and I_n stands for the n -th order modified Bessel Function of the first kind. As before, there is no closed-form expression for (70).

Symbol Error Rate To analyze the performance of the symbol detector as a function of the observation window length T_{win} , we are interested in computing the SER. This is directly obtained as

$$SER = P_{e|s=0} p_{s=0} + P_{e|s=1} p_{s=1}, \quad (72)$$

where p_0 and p_1 refer to the probability to transmit 0 and 1, respectively, and

$$P_{e|s=0} = \int_{\frac{2V_{th}}{N_0}}^{\infty} f_{Y,no}(y) dy, \quad (73)$$

$$P_{e|s=1} = \int_0^{\frac{2V_{th}}{N_0}} f_{Y,si}(y) dy, \quad (74)$$

where $f_{Y,no}$ and $f_{Y,si}$ are given by (68) and (70), respectively, and V_{th}/N_0 stands for the normalized signal power for the detection of logic 0 and logic 1 and N_0 stands for the noise level. The threshold value is calculated by finding out the intersection of logic 0 and logic 1.

6.2.3 Throughput Analysis

From the discussion in Sec. 6.2.2, we are interested in reducing the observation window length T_{win} to reduce the value of N in (68) and the SER given by (72). In Sec. 6.2.1, we showed that with the proposed synchronization block, T_{win} can be reduced by increasing the number of synchronization bits x in (57). Transmitting longer preambles can result in a reduction of the throughput, but at the same, given that the SER is reduced, it is more likely that the transmitted bits are properly received, which improves the throughput. Therefore, there is a compromise between different parameter values on the synchronization and symbol detection block.

In this section, we aim at identifying the best values for such parameters, by defining the maximization of the throughput as an optimization problem. In particular, the problem is formulated as:

Given:	SNR, μ
Find:	m, x, n_{bits}
Maximize:	$S = \frac{n_{bits}}{T_{delay}}$
Subject to:	$m^x \leq \beta; \quad n_{bits} \leq \frac{\log_{10} \left(1 + \frac{1}{2 \cdot m^x} \right)}{\log_{10} (1 + \mu)};$ $SER = \Psi(m, x, SNR);$ $FER = \Lambda(SER, n_{bits}, x); \quad \eta = 1/FER;$ $T_{delay} = (\eta - 1)(n_{bits} + P),$

where

- The first constraint guarantees that the final observation window length T_{win} is shorter than the symbol duration T_s , as given by (59).
- The second constraint guarantees that there is no need for re-synchronization within the transmission of one frame. This depends on the clock skew μ in (64).

- Ψ in the third constraint represents the SER as a function of m , x and SNR , and is given by (72).
- Λ in the fourth constraint represents the Frame Error Rate (FER) and is a function of the SER and the total number of bits per frame, including the synchronization preamble. If we consider that a simple error detection scheme is used, without error correction capabilities,

$$\Lambda = (1 - SER)^{(n_{bits} + P)}, \quad (76)$$

where P is the total number of bits in the preamble, $P \geq x$, as not all the bits in the preamble might be ones.

- η refers to the average number of retransmissions per frame and T_{delay} refers to the average delay per frame.

The optimal values for m , x and n_{bits} that maximize the single link throughput can be then numerically obtained.

6.3 Results and Discussions

In this section, we first test the functioning of the proposed synchronization scheme with experimental THz pulses. Then, we numerically investigate the impact of different parameters on the performance of the synchronization and detection blocks and compute the achievable throughput.

6.3.1 Synchronization Test with Experimental Data

To test the functioning of the proposed synchronization algorithm, we utilize measured THz pulses generated and captured by means of a time-domain THz spectroscopy platform available to the authors. Such platform is able to generate one-hundred-femtosecond-long pulses, which are emitted in free space and measured at a distance by a detector. The captured signal is passed through the proposed synchronization block in Fig. 18 which iteratively estimates the symbol start time and, thus, the necessary delay to be introduced by the first VCD during the reception of the actual data symbols.

The different iterations of the algorithm for $m = x = 2$ are illustrated in Fig. 21. In the first iteration, CTMA₁ looks from $T_s/2$ to T_s and CTMA₂ looks from 0 to $T_s/2$. CTMA₂ detects the pulse and, thus, Block1=2. In the second iteration, CTMA₁ looks from $T_s/4$ to $T_s/2$ and CTMA₂ looks from 0 to $T_s/4$. Now CTMA₁ detects the pulse and, thus, Block2=1. During the data phase, VCD₁ is tuned to introduce a delay equal to $0.5T_s$ and CTMA₁ utilizes an observation window length equal to $T_s/4$. In Table 2, we summarize the output for different number of pulses in the synchronization preamble x .

After the synchronization preamble, the measured data symbols were detected by utilizing the estimated delay for VCD₁ and the observation window length for CTMA₁. The low noise in the measurements resulted in almost no symbol errors, in line with the numerical results discussed next.

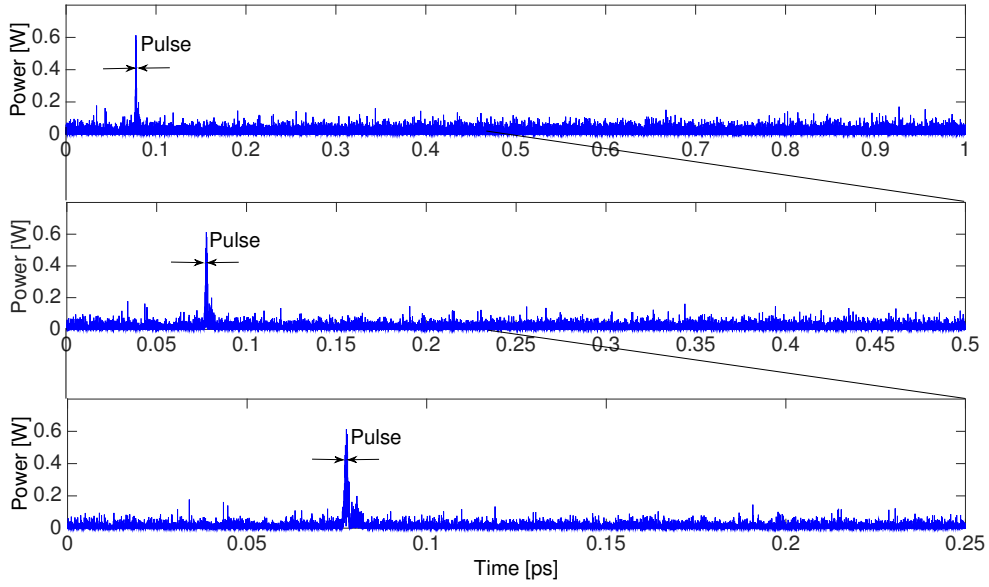


Fig. 21: Illustration of the synchronization algorithm for $m = x = 2$: First iteration (top); Second iteration (middle); Third iteration (bottom).

Table 2: Iterations in the synchronization algorithm ($m=2$)

Preamble	it=1	it=2	it=3	it=4	T_d	T_{win}
$x = 2$	2	2	NA	NA	T_S	$T_S/4$
$x = 3$	2	2	2	NA	T_S	$T_S/8$
$x = 4$	2	2	2	1	$15T_S/16$	$T_S/16$

6.3.2 Numerical Results

We consider the following parameters in our analysis. The transmitted pulses are modeled as the first time derivative of a Gaussian pulse with pulse length $T_p=100$ fs and pulse energy $E_p=1$ aJ. The time between symbols T_s is set to 10 ps ($\beta = 100$). Symbols are considered equiprobable, i.e., $p_{s=0} = p_{s=1} = 0.5$ in (72).

Impact of Clock Skew on the Frame Length In Fig. 22, the number of bits n_{bits} after which resynchronization is needed given by (64) is shown as a function of number of branches in the synchronization block m , for different values of the clock skew μ . As expected, for higher values of μ , the number of bits after which re-synchronization should take place decreases hence signifying, re-synchronization becomes more often and more preamble bits are needed to transmit the same amount of data bits. Moreover, as the number of channel increases, the number of bits after which re-synchronization should take place decreases. This is because, T_{win} decreases as we increase m and hence, the CTMA looks to re-synchronize again when the clock shifts by a value of T_{win} which is small for large values of m .

Symbol Error Rate In Fig. 23, the SER given by (72) is shown as a function of the SNR for four different values of m^x . As the term m^x increases, the observation window length T_{win} decreases and,

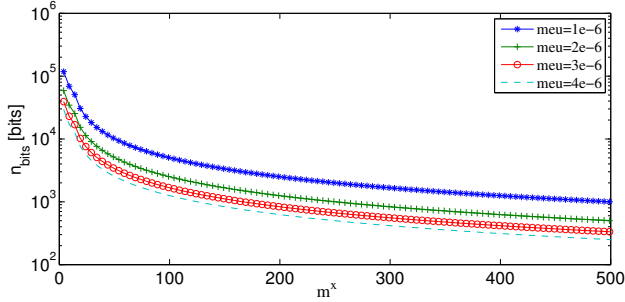


Fig. 22: Maximum number of bits before resynchronization as a function of m^x , for different values of the clock skew μ .

thus, the SER also decreases. This can also be understood from the PDFs for the detected signal in the transmission of 0s and 1s, given by (68) and (70), respectively.

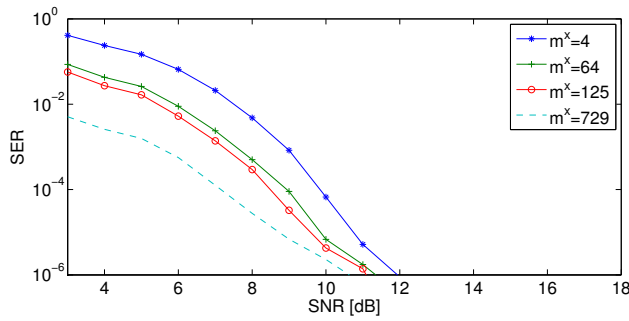


Fig. 23: SER as a function of the SNR for different values of m^x .

Throughput In Fig. 24, the throughput given by (75) is plot as a function of the m^x for different values of the SNR. It can be seen that as the value of m^x increases, the throughput also increases. This result shows that the benefits of reducing SER by shortening the observation window length T_{win} largely overcome the cost introduced by increasing the size of the synchronization block, i.e., increasing m , or transmitting longer synchronization pREAMbles, x .

Given the constraints of nano-devices, it seems more adequate to keep m to the minimum number possible, i.e., $m = 2$, and investigate the impact of x alone. In Fig. 25, the throughput is shown as a function of the x for $m = 2$. For low SNR values, the impact of x on the SER is larger than the impact of x in the total delay. Therefore, the throughput S increases rapidly with x at low values of SNR . For example, for $SNR=3$ dB, we can triple the throughput by adding only 6 bits to the synchronization preamble. For higher values of SNR , the impact of x on the SER is less significant and hence the throughput does not drastically change with x .

Finally, the impact of the number of bits per frame on the throughput S is illustrated by means of Fig. 26. For low values of SNR , lesser of bits should be sent in a single packet, whereas for large values of SNR , the trend reverses and the throughput remains the same for the different numbers of bits.

Optimal Synchronization and Detection Parameters In light of the illustrated results, combined with exhaustive search, the values of m , n , SNR and $bits$ that are required to maximize the throughput can be summarized as follows. For SNR above 7 dB, the throughput remains almost constant

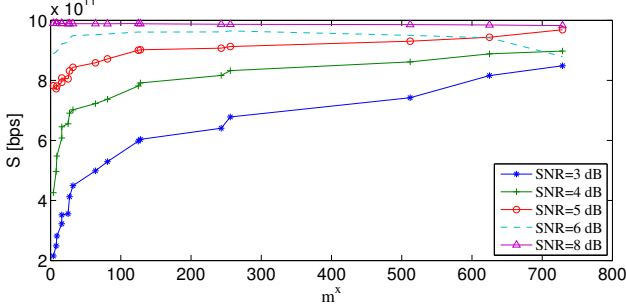


Fig. 24: Throughout as a function of the SNR for different values of m^x (frame length=1000 bits).

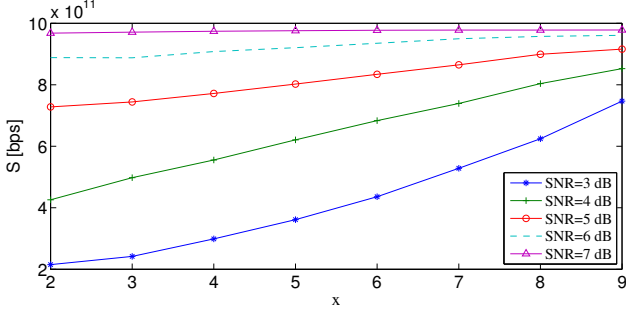


Fig. 25: Throughout as a function of the SNR for different values of x ($m=2$, frame length=1000 bits).

for different values of x , m and *bits*. In that case, reducing m and x allows the transmission of longer frames, if needed, and simplifies the synchronization block hardware. Otherwise, the maximum throughput is numerically obtained for $x = 6$, $m = 3$ and *bits* = 5000. For low SNR values, significant improvement is achieved by increasing the number of bits in the synchronization preamble x . Maximum throughput is achieved again for $x = 6$ and $m = 3$, now with shorter frames.

6.3.3 Discussion

We have proposed a joint physical-layer synchronization and symbol detection scheme for pulse-based THz-band communication. The main objective of the proposed scheme is to jointly determine the symbol start time and the observation window length, by successively narrowing down the integration window around the true location of the pulse. The proposed solution is

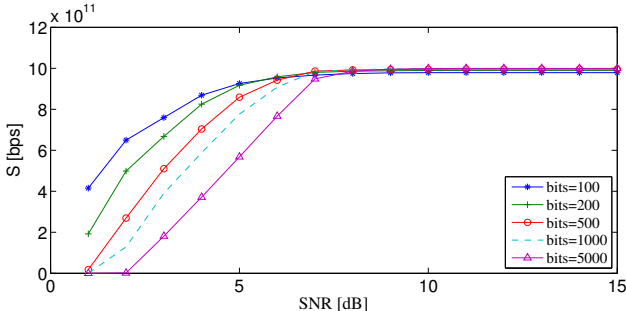


Fig. 26: Throughout as a function of the SNR for different values of *bits* ($m=3$, $x=6$).

fully analog and can be implemented with a combination of voltage-controlled delay lines and continuous-time moving-average symbol detectors with tunable observation window. We have analytically investigated the synchronization preamble length and the maximum number of bits to be transmitted before requiring re-synchronization. We have also obtained analytical expressions for symbol error rate as a function of the observation window length. We have investigated the compromise between synchronization preamble length and symbol detection observation window length, and investigated their joint impact on the achievable throughput. Finally, we have tested the algorithm with experimental THz pulses and provided extensive simulation results to analyze the impact of different parameters. The results show how, with the proposed synchronization algorithm, tight synchronization and low symbol error rates are possible just with very short preambles, less than bits long.

7 PACKET SIZE OPTIMIZATION

7.1 Motivation

One of the key applications of THz communications is in the field of nanonetworks and WNSNs [29, 34]. Indeed, the very small size of graphene-based plasmonic nano-transceivers and nano-antennas (Sec. 4) enables their integration with miniature sensors for physical, chemical and biological sensing. On the one hand, the THz band provides nanosensors with a very large bandwidth [23]. However, on the other hand, the very high propagation loss at such frequencies combined with the very limited transmission power of nanosensors result in very short communication distances. Moreover, the limited capacity of nano-batteries, which requires the use of time-consuming energy-harvesting procedures [35, 36], and the limited computational capabilities of nanosensors, affect the throughput of WNSNs. All these interdependencies motivate the joint analysis of the nano-device capabilities, the THz band peculiarities and their impact on the achievable throughput.

There have been many cross-layer studies on packet size optimization in wireless communication networks for a myriad of environments, including terrestrial, underwater, underground, and intra-body sensor networks [77–80]. However, all these works cannot be directly applied for energy-harvesting networks, in which the energy fluctuates with time instead of monotonically decreasing. In this direction, several energy consumption optimization problems for wireless networks with energy harvesting nodes have been proposed over the recent years [81–83]. All these works are mainly focused on optimizing the utilization of the harvested energy following a general approach to find the trade-off between the consumed energy and the achieved quality of service. While the aforementioned studies are applicable to general wireless communication networks, in [84], a study is performed for the specific case of communication in nanonetworks. However, the impact of such energy management policies on the achievable throughput at the link layer is not analyzed.

As part of this effort, we have addressed the throughput maximization problem in WNSNs, by taking into account the existing device and communication interdependencies. In particular, a link throughput optimization problem is defined, and the optimal data packet size which maximizes the link efficiency is derived by capturing the power, energy and computational constraints of nanosensors; the very high path-loss and very large bandwidth of the THz-band channel; the possibility to communicate by transmitting one-hundred-femtosecond-long pulses, which can virtually create parallel orthogonal channels between nanosensors [63]; and three different error control strategies tailored to WNSNs, namely, Automatic Repeat reQuest (ARQ), Forward Error Correction (FEC) and novel Error Prevention Codes (EPCs), which have been designed with the WNSNs peculiarities in mind [85]. Both the energy harvesting limits and the successful packet transmission time are defined as the optimization problem constraints, and the optimal solution is derived by using a bisection method. Our results show that the link efficiency quickly decreases when considering the energy constraints compared to the scenario that there is no energy shortage. The decrease depends on various parameters including the error-control technique, the communication distance, and the harvesting capability of the nanosensors. Similarly, the packet size quickly decreases with the transmission distance, approaching several hundreds bits for distances beyond a few millimeters.

Next, in Sec. 7.2.1, we define the system model for WNSNs and discuss the throughput optimization problem while defining different constraints for various error-control methods. Sec. 7.2.2

contains the approach to solve the optimization problem, and covers the related algorithm to find the optimal solution for our problem. Finally, in Sec. 7.3.1, we numerically study the optimal packet size for different error-control techniques and compare the performance of them under different conditions.

7.2 Methods, Assumptions and Procedures

7.2.1 System Model and Optimization Problem Formulation

We consider a single communication link between two nanosensors. Nanosensors communicate with each other using TS-OOK [63]. As previously discussed, such mechanism can effectively provide nanomachines with orthogonal communication challenges, thus minimizing the potential multi-user interference. The transmitter node is a nanomachine with the capability of harvesting energy by means of piezoelectric nano-generators [35], which converts kinetic energy into electricity by exploiting nanowires. At the receiver node it is assumed that always enough energy is available to receive the packets successfully, and the receiver has enough amount of memory to buffer the received data. Based on these assumption, first a throughput optimization problem with the objective of maximizing the link throughput between a pair of transceivers in a WSN is defined in this section, considering different constraints for different error-control techniques. Then different constraints are tailored in details for different error-control techniques respectively. We start with the definition of throughput in a WSN link as the rate of successful message transmission measured in bits per second (bps), which can be given by:

$$S = \frac{\text{Useful Data Length}}{\text{Successful Transmission Time}}. \quad (77)$$

Without loss of generality, instead we can optimize the link utilization efficiency η for a given transmission rate r which can be further defined as:

$$\eta = \frac{1}{r} \cdot \frac{L_{data}}{N_{ret} \cdot T_{tx}}, \quad (78)$$

where L_{data} is the useful data length in bits, N_{ret} represents the expected number of retransmissions needed for the packet to be received and processed successfully at the receiver node according to the chosen error-control method. T_{tx} is the total time required to accomplish a complete packet transmission including the time required to harvest enough energy for transmission, and will be defined later in Sec. 7.2.1 as one of the constraints of the optimization problem. Hence, for a chosen error-control technique, to find optimal data length L_{data}^* which maximizes the link efficiency, the optimization problem can be formulated as follows.

Channel Efficiency Maximization Problem for WSNs We define next the optimization problem with the objective function of maximizing the channel efficiency in WSNs, and the constraints which will be defined later in Sec. 7.2.1 through 7.2.1 in details according to the error-control method.

Optimization Problem [P1]

Given :	$r, \psi^{\mathcal{E}}, \phi^{\mathcal{E}}, N_0, p_x^{\mathcal{E}}, f, d, \theta^{\mathcal{E}}, \tau^{\mathcal{E}}, E_{tx}^{\mathcal{E}}, \lambda_{harv}$
Find :	L_{data}^*
Maximize :	$\eta = \frac{1}{r} \cdot \frac{L_{data}}{N_{ret} \cdot T_{tx}}$
Subject to :	

$$L_{data} > 0 \quad (79)$$

$$N_{ret} = \frac{1}{1 - p_e} \quad (80)$$

$$p_e = \psi^{\mathcal{E}}(BER, L_{data}, L^{\mathcal{E}}) \quad (81)$$

$$BER = \phi^{\mathcal{E}}\left(\frac{E_{tx}^{bit}}{\overline{PL} \cdot N_0}, p_x^{\mathcal{E}}\right) \quad (82)$$

$$T_{tx} = \max\{T_{tx}^{\mathcal{E}}, T_{tx-harv}^{\mathcal{E}}\} \quad (83)$$

$$T_{tx}^{\mathcal{E}} = \theta^{\mathcal{E}}(L_{data}, L^{\mathcal{E}}, T_{proc}^{\mathcal{E}}, T_{t/o}^{\mathcal{E}}, T_{prop}) \quad (84)$$

$$T_{tx-harv}^{\mathcal{E}} = \tau^{\mathcal{E}}(L_{data}, L^{\mathcal{E}}, E_{tx}^{\mathcal{E}}, p_x^{\mathcal{E}}, \lambda_{harv}) \quad (85)$$

$$E_{tx}^{\mathcal{E}} \leq \lambda_{harv} \cdot T_{tx-harv}^{\mathcal{E}} \quad (86)$$

where:

- $p_e = \psi^{\mathcal{E}}(BER, L_{data}, L^{\mathcal{E}})$ is the *Packet Error Rate* (PER), which is a function of the *Bit Error Rate* (BER), data length L_{data} , and the length of the redundant bits $L^{\mathcal{E}}$, which depends on the error-control scheme \mathcal{E} .
- $BER = \phi^{\mathcal{E}}\left(\frac{E_{tx}^{bit}}{\overline{PL} \cdot N_0}, p_x^{\mathcal{E}}\right)$ is a function of energy required to transmit a bit E_{tx}^{bit} , the path loss between the transmitter and receiver nodes \overline{PL} , and the noise spectral density N_0 . It also depends on the pulse probability $p_x^{\mathcal{E}}$ that itself varies according to the chosen error-control method \mathcal{E} .
- $\overline{PL}(f, d)$ is the path loss between the transmitter and receiver nodes and depends on the transmission frequency f and the distance between the nodes d .
- $T_{tx}^{\mathcal{E}} = \theta^{\mathcal{E}}(L_{data}, L^{\mathcal{E}}, T_{proc}^{\mathcal{E}}, T_{t/o}^{\mathcal{E}}, T_{prop})$ is the *packet round-trip time* or the total time needed for the packet to be transmitted and the acknowledgment to be received. $T_{proc}^{\mathcal{E}}$ and $T_{t/o}^{\mathcal{E}}$ are the processing time for a complete packet transmission and the time-out before retransmission respectively, and will be later defined in Sec. 7.2.1 through 7.2.1 based on chosen \mathcal{E} . T_{prop} is the propagation time and is relative to the distance between the transmitter and receiver nanomachines and it can be rewritten as d/c where c is the speed of light.
- $T_{tx-harv}^{\mathcal{E}} = \tau^{\mathcal{E}}(L_{data}, L^{\mathcal{E}}, E_{tx}^{\mathcal{E}}, p_x^{\mathcal{E}}, \lambda_{harv})$ is the time to harvest enough energy for a complete transmission including processing and transmitting the data.

- $E_{tx}^{\mathcal{E}}$ is the energy consumption needed to transmit a packet of length L_{data} . Note that this energy contains both the required energy to process data which depends on selected \mathcal{E} , and the required energy for transmitting the data which depends on L_{data} , $L^{\mathcal{E}}$, and $p_x^{\mathcal{E}}$.
- λ_{harv} is the rate at which the nanosensor transmitter mote is able to harvest energy in J/s.

Here we assume that the nano-transmitter always transmits with the maximum available energy, hence the inequality in (86) reduces to the following equality:

$$E_{tx}^{\mathcal{E}} = \lambda_{harv} \cdot T_{tx-harv}^{\mathcal{E}}; \quad (87)$$

Therefore the function $\tau^{\mathcal{E}}$, can be defined as follows:

$$\tau^{\mathcal{E}} = \frac{E_{tx}^{\mathcal{E}}}{\lambda_{harv}}. \quad (88)$$

Hence the two constraints (85) and (86) can be merged into one constraint as in (88). Moreover, for the *BER*, the function $\phi^{\mathcal{E}}$ does not depend on the optimization variable L_{data} , and depends on the physical layer parameters. In this paper we use the derived values for *BER* in [85], as given values of the proposed optimization problem.

As it can be seen, the optimization problem defined in [P1] is a general problem with functions $\psi^{\mathcal{E}}$, $\theta^{\mathcal{E}}$, and $E_{tx}^{\mathcal{E}}$ which have to be defined for three different error-control techniques, namely ARQ, FEC, and EPC, which are addressed as follows.

Automatic Repeat reQuest (ARQ) Constraints The *packet error rate* in ARQ is defined as follows:

$$\psi^{\mathcal{E}} = 1 - (1 - BER^{ARQ})^l, \quad (89)$$

where $l = L_{data} + L_{CRC}$, and L_{CRC} is the length of *Cyclic Redundancy Check* (CRC) used for error detection. Moreover, the *packet round-trip time* is given by the following equation:

$$\begin{aligned} T_{tx}^{ARQ} &= T_{tx,data}^{ARQ} + T_{CRC} \\ &+ p_{s,data}^{ARQ} p_{s,ack}^{ARQ} (2T_{prop} + T_{CRC} + T_{tx,ack}^{ARQ}) \\ &+ (1 - p_{s,data}^{ARQ} p_{s,ack}^{ARQ}) T_{t/o}^{ARQ}, \end{aligned} \quad (90)$$

where $T_{tx,data}^{ARQ}$ and $T_{tx,ack}^{ARQ}$ are the data and acknowledgment transmission times and are given by l/r and L_{ack}/r respectively, where L_{ack} is the acknowledgment packet length. T_{CRC} refers to the delay caused by computational process of the CRC, and is given by $(L_{data} \cdot T_{clk})$ where T_{clk} is the inverse of the nanomachine's clock frequency. $p_{s,data}^{ARQ}$ and $p_{s,ack}^{ARQ}$ are *data* and *acknowledgment* packet success rate respectively and can be obtained from (89) with $l = L_{data}$ and $l = L_{ack}$ respectively. Finally $T_{t/o}^{ARQ}$ is defined as follows:

$$T_{t/o}^{ARQ} = 1.1(2T_{prop} + T_{CRC} + T_{tx,ack}^{ARQ}), \quad (91)$$

which is the propagation delay to transmit the data and receive the acknowledgment, plus the time the receiver takes to process the CRC and transmit the acknowledgement packet, plus a ten percent margin time. The energy required for transmission process in ARQ can be defined as follows [85]:

$$E_{tx}^{ARQ} = E_{tx,data}^{ARQ} + E_{CRC} + p_{s,data}^{ARQ} p_{s,ack}^{ARQ} E_{rx,ack}^{ARQ}, \quad (92)$$

where $E_{tx,data}^{ARQ}$ and $E_{rx,ack}^{ARQ}$ refer to the energy required to transmit the data packet and receive the acknowledgement packet, and are given by $(l \cdot p_x^{\mathcal{E}} \cdot E_{tx}^{bit})$ and $(p_{s,data}^{ARQ} \cdot p_{s,ack}^{ARQ} \cdot L_{ack} \cdot E_{rx}^{bit})$ respectively. E_{CRC} stands for the consumed energy caused by computational process of the CRC, and is given by $(L_{CRC} \cdot L_{data}(E_{shift} + E_{hold}))$ where E_{shift} and E_{hold} are the energy consumed to shift and hold a registry value in a shift register. Note that the value of E_{CRC} is defined based on the assumption that a CRC is implemented by exploiting shift registers and XOR logic gates as described in [85]. Therefore, the equivalent optimization problem for the ARQ mode, is given by [P1], while replacing the constraints (81) and (84) by (89) and (90), respectively, and using constraint (88) instead of (85) and (86), while the definition of $E_{tx}^{\mathcal{E}}$ is given by (92).

Forward Error Correction (FEC) Constraints For the FEC, $\psi^{\mathcal{E}}$ depends on the *Block Error Rate* (BLER), and is defined as follows:

$$\psi^{\mathcal{E}} = 1 - (1 - BLER^{FEC})^n, \quad (93)$$

where n is the number of blocks per data packet payload, and $BLER^{FEC}$ is given as follows:

$$BLER^{FEC} = \sum_{j=t+1}^k \binom{k}{j} (BER)^j (1 - BER)^{k-j}, \quad (94)$$

where k refers to the block size and t is the error correction capability of the code. Moreover, the *packet round-trip time* for FEC can be defined as follows:

$$T_{tx}^{FEC} = T_{tx,data}^{FEC} + T_{code}^{FEC} + p_{s,data}^{FEC} (T_{prop} + T_{decode}^{FEC}) + (1 - p_{s,data}^{FEC}) T_{t/o}^{FEC}, \quad (95)$$

where $T_{tx,data}^{FEC}$ is the data transmission time and is given by l/r where l is the total length of the transmitted *data* and is equal to $(L_{data} + L^{FEC})$, and L^{FEC} is the length of the redundant bits added for error correction. T_{code}^{FEC} and T_{decode}^{FEC} refer to latency caused by coding and decoding processes of the *data* respectively and are given as follows [85]:

$$T_{code}^{FEC} = 2nT_{clk} \quad (96)$$

$$T_{decode}^{FEC} = (k + 1)nT_{clk}, \quad (97)$$

$p_{s,data}^{FEC}$ is the *data* packet success rate and can be obtained from (93). Finally, $T_{t/o}^{FEC}$ is given as follows:

$$T_{t/o}^{FEC} = 1.1(2T_{prop} + T_{decode}^{FEC}). \quad (98)$$

The function $E_{tx}^{\mathcal{E}}$ for FEC mode is defined as follows:

$$E_{tx}^{FEC} = E_{tx,data}^{FEC} + E_{code}^{FEC}, \quad (99)$$

where $E_{tx,data}^{FEC}$ refers to the energy required to transmit the data packet, and is given by $(l \cdot p_x^{\mathcal{E}} \cdot E_{tx}^{bit})$, and E_{code}^{FEC} stands for the consumed energy caused by computational process of coding the *data* in transmitter, and is given by $n \cdot k(E_{load} + E_{hold})$ where E_{load} and E_{hold} are the energy consumed to load and hold a registry value in a shift register. Note that the value of E_{code}^{FEC} is defined based on the assumption that a Hamming code is exploited for the FEC which can be implemented by using shift registers as well as XOR and AND logic gates as described in [85]. Therefore, the equivalent optimization problem for the FEC mode, is given by [P1], while replacing the constraints (81) and (84) by (93) and (95), respectively, and using constraint (88) instead of (85) and (86), while the definition of $E_{tx}^{\mathcal{E}}$ is given by (99).

Error Prevention Codes (EPC) Constraints Instead of correcting channel errors or just detecting them and asking for retransmissions *a posteriori*, the idea of preventing channel errors from occurring in advanced or *a priori*, has been recently proposed [85]. The fundamental idea is that, by adjusting the coding weight, i.e., the average number of logical “1”s and “0”s, the molecular absorption noise at THz-band frequencies and the multi-user interference in TS-OOK can be minimized. This effectively results into lower BERs. Different EPC techniques are discussed in detail in [85].

In this case, the *packet error rate* is given by

$$\psi^{\mathcal{E}} = 1 - (1 - BER^{EPC})^{nk}, \quad (100)$$

where n is the number of blocks per data packet payload, and k refers to the block size. Moreover, the *packet round-trip time* in EPC is defined as follows:

$$T_{tx}^{EPC} = T_{tx,data}^{EPC} + T_{code}^{EPC} + p_{s,data}^{EPC}(T_{prop} + T_{decode}^{EPC}) + (1 - p_{s,data}^{EPC})T_{t/o}^{EPC}, \quad (101)$$

where $T_{tx,data}^{EPC}$ is the data transmission time and is given by l/r where l is the total length of the transmitted *data* and is equal to $(L_{data} + L^{EPC})$, and L^{EPC} is the length of the redundant bits added by error prevention codes. T_{code}^{EPC} and T_{decode}^{EPC} refer to latency caused by coding and decoding processes of the *data* respectively and are given as follows [85]:

$$T_{code}^{EPC} = T_{decode}^{EPC} = 2nT_{clk}, \quad (102)$$

$p_{s,data}^{EPC}$ is the *data* packet success rate and can be obtained from (100). Finally, $T_{t/o}^{EPC}$ is given as follows:

$$T_{t/o}^{EPC} = 1.1(2T_{prop} + T_{decode}^{EPC}). \quad (103)$$

Eventually, the following equation describes the energy required to accomplish the transmission process $E_{tx}^{\mathcal{E}}$ in EPC:

$$E_{tx}^{EPC} = E_{tx,data}^{EPC} + E_{code}^{EPC}, \quad (104)$$

where $E_{tx,data}^{EPC}$ refers to the energy required to transmit the data packet, and is given by $(l \cdot p_x^{\mathcal{E}} \cdot E_{tx}^{bit})$, and E_{code}^{EPC} stands for the consumed energy caused by computational process of coding the *data* in transmitter, and is given by $n \cdot (l_d + k)(E_{load} + E_{hold})$, where E_{load} and E_{hold} are the energy

consumed to load and hold a registry value in a shift register, and l_d is the length of useful data bits in a transmitted block. Note that the value of E_{code}^{EPC} is defined based on exploiting logic gates and parallel-load shift registers to implement the EPC as described in [85]. Therefore, the equivalent optimization problem for the EPC mode, is given by [P1], while replacing the constraints (81) and (84) by (100) and (101), respectively, and using constraint (88) instead of (85) and (86), while the definition of $E_{tx}^{\mathcal{E}}$ is given by (104).

7.2.2 Problem Solution Approach and Algorithm

Solution of The Optimization Problem [P1] To solve the optimization problem [P1], we start with the equality constraints (80), (81), and (82). As it is mentioned earlier in Sec. 7.2.1, the *BER* does not depend on the optimization variable and the constraint (82) can be defined as a given parameter to our optimization problem. Moreover the equalities (80) and (81) can be merged with the objective function of [P1]. For the equality constraint (83) which contains the non-smooth maximum function, we can also plug it in the objective function by defining two auxiliary efficiency functions $\eta_1(L_{data})$ and $\eta_2(L_{data})$ as follows:

$$\eta_1(L_{data}) = \frac{1}{r} \cdot \frac{L_{data}(1 - \psi^{\mathcal{E}})}{\theta^{\mathcal{E}}}, \quad (105)$$

$$\eta_2(L_{data}) = \frac{1}{r} \cdot \frac{L_{data}(1 - \psi^{\mathcal{E}})}{\tau^{\mathcal{E}}}; \quad (106)$$

Hence we can define our objective function as follows:

$$\eta = \min\{\eta_1(L_{data}), \eta_2(L_{data})\}. \quad (107)$$

Note that $\eta_1(L_{data})$ and $\eta_2(L_{data})$ only depend on the L_{data} as the optimization variable, and all other parameters are assumed to be given. Also the functions $\psi^{\mathcal{E}}$, $\theta^{\mathcal{E}}$, and $\tau^{\mathcal{E}}$ are all functions of L_{data} which are defined in Sections 7.2.1 through 7.2.1 for three different error-control techniques. Now by merging the constraints (80), (81), (82), and (83) with the objective function of [P1], we can define the following equivalent optimization problem:

Optimization Problem [P2]

Given :	$r, \psi^{\mathcal{E}}, \theta^{\mathcal{E}}, \tau^{\mathcal{E}}$
Find :	L_{data}^*
Minimize :	$-\eta = \max\{-\eta_1(L_{data}), -\eta_2(L_{data})\}$
Subject to :	$L_{data} > 0$

where $\eta_1(L_{data})$ and $\eta_2(L_{data})$ are given in (105) and (106) respectively. Note that here we are using the standard minimization problem by changing the sign of the functions η , $\eta_1(L_{data})$ and $\eta_2(L_{data})$, and using *max* function instead of *min*. It can be shown that [P2] is a Quasi-Convex optimization problem. More specifically, $-\eta_1(L_{data})$ and $-\eta_2(L_{data})$ are Quasi-Convex functions and since “nonnegative weighted maximum” function preserves Quasi-Convexity [86] therefore the

objective function $-\eta(L_{data})$ is Quasi-Convex. Moreover, the inequality constraint (79) is a convex set, hence [P2] is a Quasi-Convex optimization problem. For solving this optimization problem we define the epigraph form of the problem and use a bisection method described in Sec. 7.2.2.

Epigraph Form and Bisection Algorithm to Solve [P1] To solve the optimization problem stated in [P2] we can define the epigraph form of the problem as follows:

Epigraph form of Optimization Problem [P2]

$$\begin{aligned}
 \text{Given :} & \quad r, \psi^{\mathcal{E}}, \theta^{\mathcal{E}}, \tau^{\mathcal{E}} \\
 \text{Find :} & \quad L_{data}^* \\
 \text{Minimize :} & \quad t \\
 \text{Subject to :} & \quad -\eta(L_{data}) - t \leq 0 \\
 & \quad -L_{data} < 0
 \end{aligned}$$

Now, our quasi-convex optimization problem can be solved as a sequence of convex feasibility problems as follows:

$$\begin{aligned}
 \text{Given :} & \quad r, \psi^{\mathcal{E}}, \theta^{\mathcal{E}}, \tau^{\mathcal{E}} \\
 \text{Find :} & \quad L_{data}^* \\
 \text{Subject to :} & \quad -\eta(L_{data}) - t \leq 0 \\
 & \quad -L_{data} < 0
 \end{aligned} \tag{108}$$

The above feasibility problem is convex, since all its inequality constraints are convex. Now let us define p^* as the optimal value of our optimization problem in [P2]. If the problem (108) is feasible, then $p^* \leq t$, and if it is not feasible, then $p^* \geq t$. Therefore by using a bisection method we can solve the our quasi-convex optimization problem, by solving a convex feasible problem in each iteration. For the bisection method we have to determine a lower bound l and an upper bound u for the possible values of p^* . Since we are dealing with efficiency ($-\eta$) as our objective function so we know that it always $\eta \in [0, 1]$. Hence we can set the bounds to $l = -1$ and $u = 0$. However, it can be easily observed that $\min(-\eta) \geq \max\{\min(\eta_1), \min(\eta_2)\} \geq -1$, and since η_1 and η_2 are both quasi-convex, differentiable, and continuous, we can directly calculate the min value of them and use it for the lower bound as $l = \max\{\min(-\eta_1), \min(-\eta_2)\}$ which results in less iterations. The steps of the bisection method to solve [P2] are defined in Algorithm 1.

7.3 Results and Discussions

7.3.1 Numerical Results and Performance Evaluation

In this section we numerically study the performance of different error-control techniques, in terms of maximum link throughout achievable under the energy harvesting and transmission delay constraints.

In our analysis we use the following parameters. We consider that nanosensors communicate by using TS-OOK, hence every bit of logic “1” is transmitted as a pulse (which is modeled as the

Algorithm 1 Bisection Algorithm for solving [P2]

Set: $l = \max\{\min(-\eta_1), \min(-\eta_2)\}$ using equations (105), (106)

Set: $u = 0$, and $\epsilon > 0$

```
1: repeat
2:    $t := (l + u)/2$ 
3:   Solve the convex feasibility problem (108)
4:   if (108) is feasible then
5:      $u := t$ 
6:   else
7:      $l := t$ 
8:   end if
9: until  $u - l < \epsilon$ 
```

derivative of a one-hundred-femtosecond long Gaussian pulse) with energy of $E_{tx}^{bit} = 1$ aJ, and the logic “0” is transmitted as silence [63]. The propagation of the pulses is modeled by utilizing the THz-band channel model in [23]. Both TS-OOK and this model have been validated by means of extensive simulations with COMSOL Multi-physics. Due to the limited computational capability of nanomachines, only very simple error-control methods are utilized. For the ARQ, we use a 16-bit CRC for error correction with a 2 bytes long acknowledgement packet; a Hamming(15,11) code is assumed for the FEC; and, for EPC, a 16-bit low-weight code with codeword size of 19 bits is used (EPC type II [85]). The resulting probability to transmit a pulse p_x^E is 0.5 for ARQ and FEC, and 0.31 for EPC.

We further consider that the nanosensors communicate with the bit rate of $r = 100$ Gbps, and the the clock period to compute the latency caused by the CRC or coding and decoding processes is $T_{clk} = 1$ ps. We also consider the energy required to shift, hold, and load in a shift register as $E_{shift} = E_{hold} = E_{load} = 0.1$ aJ. The communication distance range is assumed to be $d = 1 - 100$ mm, and the energy harvesting rate ranges $\lambda_{harv} = 1 - 400$ nJ/s.

The link efficiency η of the ARQ is shown in Fig. 27 as a function of packet size for a fixed distance and energy harvesting rate. η_1^{ARQ} in this figure represents the link efficiency affected only by the transmission time, i.e., the nano-transmitter has enough energy to transmit and does not need time to harvest energy. In contrary η_2^{ARQ} , shows the link efficiency which is only affected by energy harvesting time consumption, i.e., the transmission time is always less than the time needed to harvest energy. Finally, η^{ARQ} shows the trade-off between these two scenarios and shows the link efficiency considering both constraints. As shown in Fig. 27, as we increase the packet size, at some point, the energy harvesting time consumption becomes dominant and restricts the efficiency of the link.

In Fig. 28, the link efficiency η of different error-control techniques is shown as a function of packet size for a fixed distance and energy harvesting rate. As it can be seen in this figure, EPC performs better than the other two techniques for very small packet sizes, and as we increase the packet size FEC outperforms EPC, while ARQ has the lowest efficiency.

Fig. 29 and Fig. 30 depict the optimal link efficiency and the optimal packet size respectively, for different error-control techniques as a function of distance for a fixed energy harvesting rate. It can be seen that for very short distances EPC outperforms the other two error-control methods, while transmitting smaller packets. However, FEC has a better performance for longer distances

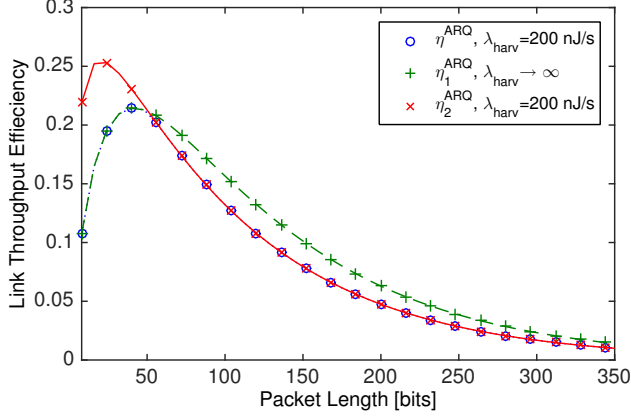


Fig. 27: Link efficiency for ARQ, when $d = 1$ cm.

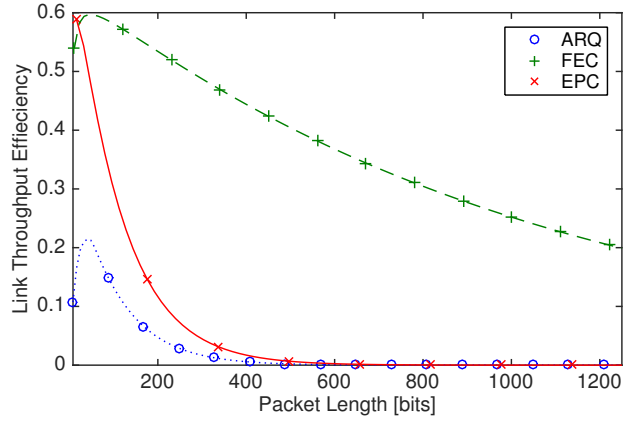


Fig. 28: Link efficiency for different error-control techniques, when $d = 1$ cm and $\lambda_{harv} = 200$ nJ/s.

and uses bigger packets for transmission. The ARQ optimal packet size is in between the other two methods, and has the lowest link efficiency.

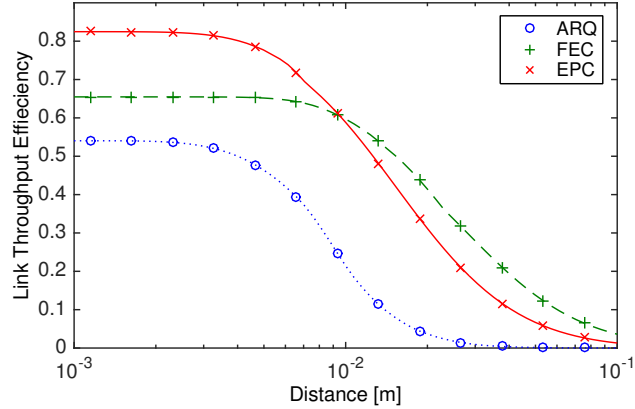


Fig. 29: Optimal link efficiency for different error-control techniques, when $\lambda_{harv} = 200$ nJ/s, and $L_{data}^{max} = 16$ Kbits.

Finally, in Fig. 31, we show the optimal link efficiency for different error-control methods as a function of energy harvesting rate, for a fixed distance. This figure shows that FEC and EPC

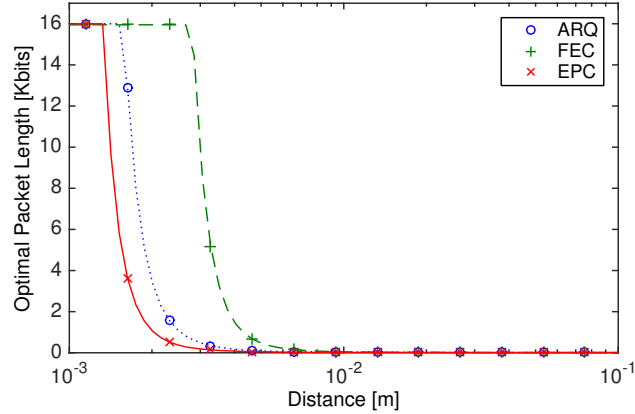


Fig. 30: Optimal packet size for different error-control techniques, when $\lambda_{harv} = 200$ nJ/s, and $L_{data}^{max} = 16$ Kbits.

have better performance for low energy harvesting rates, while ARQ outperforms the other two techniques when the nanomachines is capable to harvest energy at higher rates.

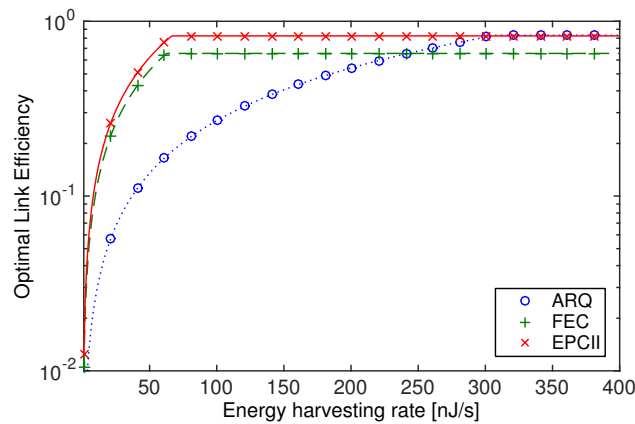


Fig. 31: Optimal link efficiency for different error-control techniques, when $d = 1$ mm, and $L_{data}^{max} = 16$ Kbits.

8 LINK LAYER SYNCHRONIZATION AND MEDIUM ACCESS CONTROL

8.1 Motivation

In parallel to the development of THz devices and physical layer mechanisms, there is a need to investigate new networking solutions for very-high-speed wireless data networks. Traditional MAC protocols need to be revised in light of the properties of THz-band communication. In particular, the THz band provides devices with a very large bandwidth and, thus, these do not need to aggressively contend for the channel. In addition, such very large bandwidth results in very high bit-rates and, consequently, very short transmission times, which further minimize the collision probability. However, due to the low transmission power of THz transceivers and the high path-loss at THz-band frequencies, very high directivity antennas are needed to establish wireless links beyond one meter. While directional communication further decreases multi-user interference, it requires tight synchronization between transmitter and receiver to overcome the deafness problem [87]. Moreover, the relatively long propagation delay when transmitting at Tbps over multi-meter-long links results in low channel utilization. While these two issues vanish in nanoscale applications, there are other challenges that affect the link layer design of THz nano-devices, such as their temporal energy fluctuations and, thus, availability, introduced by required energy harvesting systems [88].

To the best of our knowledge, there are no existing protocols for macroscale THz-band communication networks. Available solutions for lower-frequency systems cannot directly be utilized in this paradigm, mainly because they do not capture the peculiarities of the THz-band channel or the capabilities of THz devices. In terms of frequency, millimeter-wave (mm-wave) systems [4], such as those at 60 GHz, are the closest existing technology. In addition to the IEEE 802.11ad standard [89], which mainly adopts a very similar link layer to that of the entire IEEE 802.11 family, a few alternative MAC protocols for mm-wave systems have already been developed [90–92]. These protocols are mainly aimed at solving the deafness problem introduced by directional antennas. As in many of the directional MAC protocols for lower frequency bands [93, 94], the existing solutions assume that a node can alternate between directional and omnidirectional antenna modes. However, at THz-band frequencies, highly-directional antennas are simultaneously needed both at the transmitter and the receiver to successfully establish the link.

As part of this effort, we have developed a synchronization and MAC protocol for very-high-speed wireless communication networks in the THz band. The protocol relies on a receiver-initiated handshake as a way to guarantee synchronization between transmitter and receiver. In addition, it incorporates a sliding window flow control mechanism, which combined with the one-way handshake, maximizes the channel utilization. We consider two different application scenarios: a macroscale scenario, in which nodes utilize high-speed turning directional antennas to periodically sweep the space, and a nanoscale scenario, in which nodes make use of a piezoelectric nano-generator to harvest energy. For each scenario, we consider a different physical layer, namely, a traditional carrier-based modulation for the macro-scenario and a femtosecond-long pulse-based modulation with user interleaving for the nano-scenario. We analytically investigate the performance of the proposed MAC protocol in terms of delay, throughput and successful packet transmission probability, and compare it to that of a modified Carrier Sense Multiple Access with Collision Avoidance (CSMA/CA) with and without handshake. In addition, we have implemented in *ns-3* the proposed protocol and the necessary THz models (channel, carrier-based and pulse-based physical layers, turning antenna and harvesting system), and provide extensive simulation results to validate the

performance of our solution.

Next, in 8.2.1, we describe the system model considered throughout the paper and derive formulations for the bit and frame error rate, the probability of collision in the macroscale and the nanoscale scenarios, and the energy harvesting system for nano-devices. In Sec. 8.2.2, we describe the proposed protocol and analytically investigate its performance for the two scenarios. We provide simulation and numerical results in Sec. 8.3.

8.2 Methods, Assumptions and Procedures

8.2.1 THz-band Communication System Model

In this section, we summarize the main peculiarities of THz-band communication networks, both for the macroscale and the nanoscale scenarios. In particular, first, we formulate the Signal-to-Noise Ratio (SNR), which is needed for the computation of Bit Error Rate (BER) and Frame Error Rate (FER), starting from an accurate THz-band channel model. Then, we formulate the collision probability in the macroscale scenario, for which we introduce and analyze the impact of utilizing high-speed turning THz directional antennas, as well as in the nanoscale scenario, for which we revise the concept of interleaved pulse-based transmissions [95]. Finally, we introduce the energy harvesting model utilized in nanonetworks.

Signal-to-noise Ratio, Bit Error Rate and Frame Error Rate The propagation of electromagnetic waves at THz-band frequencies is mainly affected by molecular absorption, which results in both molecular absorption loss and molecular absorption noise. In particular, based on the THz-band channel model introduced in [23], the signal power at a distance d from the transmitter, P_r is given by

$$P_r(d) = \int_B S_t(f) |H_c(f, d)|^2 |H_r(f)|^2 df, \quad (109)$$

where S_t is the single-sided power spectral density (p.s.d) of the transmitted signal, B stands for its bandwidth and f refers to frequency. H_c refers to the THz-band channel frequency response, which is given by

$$H_c(f, d) = \left(\frac{c}{4\pi f d} \right) \exp \left(-\frac{k_{abs}(f) d}{2} \right), \quad (110)$$

where c refers to the speed of light and k_{abs} is the molecular absorption coefficient of the medium. This parameter depends on the molecular composition of the transmission medium, i.e., the type and concentration of molecules found in the channel and is computed as in [23]. H_r in (109) refers to the receiver frequency response, which we consider an ideal low-pass filter with bandwidth B , for the time being.

Similarly, the molecular absorption noise power N_r at a distance d from the transmitter, which can be modeled as additive, Gaussian, colored and correlated to the transmitted signal [63], is given by

$$N_r(d) = \int_B (S_{N^B}(f) + S_{N^I}(f, d)) |H_r(f)|^2 df, \quad (111)$$

where it is taken into account that the total molecular absorption noise is contributed by the background atmospheric noise p.s.d., S_{N^B} and the self-induced noise p.s.d., S_{N^I} , and are computed as described in [63].

The SNR at a distance d from the transmitter can be then obtained dividing (109) by (111). For a given SNR, the BER, P_b , only depends on the modulation technique. In our analysis, we consider two different physical layers:

- In the macroscale scenario, i.e., for distances above a few meters, we consider that nodes transmit a conventional m-PSK modulated signal over a 100-GHz-wide transmission window at 1.05 THz. This is done to overcome the very high molecular absorption loss over long distances [23].
- In the nanoscale scenario, i.e., for distances much below one meter, we consider that nodes transmit by using TS-OOK, a modulation scheme based on the transmission of one-hundred-femtosecond-long pulses by following an on-off keying modulation spread in time [63]. The p.s.d. of such pulses is mainly contained between 0.9 and 4 THz.

Finally, to compute the frame error rate P_p , we consider that a hybrid error control technique based on the combination of low-weight channel codes with ARQ is utilized [67].

Collision Probability The collision probability depends on the application.

A. Macroscale Scenario In this case, nodes require high-gain directional antennas in transmission and in reception to successfully establish a link. As we already discussed, this results into low multi-user interference, at the cost of high synchronization requirements. To model the multi-user interference, we need to take into account both the spatial distribution of the nodes as well as their temporal activity. In our model, we consider that nodes are randomly distributed in space by following a spatial Poisson process with rate λ_A . The area of influence of an individual node is given by $A(\theta) = \frac{\theta}{2\pi}\pi^2 = \frac{\theta^2}{2}$, where θ is the antenna beam-width in radians and θ stands for the maximum transmission distance. Then, the probability of finding i nodes in A is given by

$$P[i \in A(\theta)] = \frac{(\lambda_A A(\theta))^i}{i!} e^{-\lambda_A A(\theta)}. \quad (112)$$

If each node i in A generates new frames at a rate given by $1/\alpha FT$, where α is a constant and FT stands for frame time, the aggregated traffic generated by i nodes is simply $\lambda_T = i/\alpha FT$. Thus, the probability that j out of i nodes are active during a vulnerable time of $2FT$ is given by:

$$P[j \in 2FT] = \frac{(\lambda_T 2FT)^j}{j!} e^{-\lambda_T 2FT}. \quad (113)$$

Finally, the collision probability in the macroscale scenario is:

$$P_c = \sum_{i=1}^{\infty} P[i \in A(\theta)] (1 - P[0 \in 2FT]). \quad (114)$$

B. Nanoscale Scenario In this case, miniature nodes do not require directional antennas, but transmit omnidirectionally. Therefore, the probability of finding i nodes in the area of influence of a node is given by (112) for $\theta = 2\pi$. This results into a much larger number of potentially interfering nodes. Interestingly, however, TS-OOK supports the simultaneous transmission and reception of time-interleaved frames. In this scheme, a logical "0" is transmitted as silence, whereas a logical

“1” is transmitted with a pulse. The time between symbols, pulses and silences, T_s is much longer than the pulse duration T_p , $\beta = T_s/T_p \gg 1$.

By considering that each node i in A generates new frames at a rate $1/\alpha FT$, the rate at which new pulses are generated is given by $\lambda_P = ip_1/\alpha T_s$, where p_1 refers to the probability of transmitting a pulse, and is related to the coding weight [67]. Then, the probability of j out of i nodes generate pulses within the vulnerable time $2T_p$ is:

$$P [j \in 2T_p] = \frac{(\lambda_P 2T_p)^j}{j!} e^{-\lambda_P 2T_p}. \quad (115)$$

Finally, if there are n symbols in one frame, the collision probability of one frame in the nanoscale scenario is:

$$P_c = \sum_{i=1}^{\infty} P [i \in A(2\pi)] \left(1 - P [0 \in 2T_p]\right)^n. \quad (116)$$

Nano Energy Model In our analysis, we are interested in computing the frame error probability caused by insufficient energy at the transmitter or at the receiver. For this, we utilize the same methodology as in [36]. Due to space limitations, we only qualitatively describe our methodology, but refer the reader to the original paper for further details. Mainly, the probability mass function (p.m.f.) of the energy stored at the nano-node battery after reaching a steady state depends both on the rate at which energy is harvested and the rate at which energy is consumed. The latter depends on the new frame generation rate as well as on the expected number of retransmissions. Ultimately, different MAC protocols result into different number of transmissions and, thus, into different p.m.f. for the energy at the nano-battery. With the p.m.f. of the energy, we can calculate the probability of having enough energy at each node. We implement the harvesting model in *ns-3* and utilize the collected data to estimate the battery p.m.f. used in our numerical results.

8.2.2 Receiver-initiated Synchronization and Medium Access Control Protocol

In this section, we first describe the proposed protocol for THz-band communication. Then, we analytically investigate its performance in terms of successful packet delivery probability, packet delay and throughput.

Protocol Overview In light of the system model described in Sec. 8.2.1, it is clear that an initial handshake is needed in THz-band communication networks to guarantee link-layer synchronization between the transmitter and the receiver. The objective of such handshake is to prevent unnecessary data transmissions when the receiver is not available, whether because it is not facing the transmitter (macroscale scenario) or because it does not have enough energy to handle a new transmission (nanoscale scenario). The fundamental idea behind the proposed protocol is to reduce the overhead introduced by such handshaking process by having nodes announce their availability to receive data. In other words, the traditional two-way handshake is reduced to a one-way handshake process. Receiver-initiated MAC protocols have been successfully utilized in other scenarios [93, 94, 96], but the existing solutions cannot directly be utilized in our scenario because of the aforementioned peculiarities of THz-band communication networks.

Besides the one-way handshake, the proposed protocol also makes use of sliding flow control window at the link layer to maximize the channel utilization. In particular, both the delay introduced

while waiting for the receiver availability and the relatively long propagation delay when transmitting at multi-Gbps or Tbps over multi-meter distances (macroscale scenario) result in a relative low channel utilization. To overcome such problem, the receiver can specify the time that it will remain facing in the current direction (macroscale scenario) or the amount of data packets willing to accept with its currently available energy (nanoscale scenario).

The basics of the protocol are summarized next. A node can be found in transmitting mode or in receiving mode:

- A node in *transmitting mode (TM)*, i.e., with data to transmit, checks whether a current Clear-To-Send (CTS) frame from the intended receiver has been recently received. We consider that a CTS has an expiration time, which is a parameter value in our system. If not, the node listens to the channel until the reception of a new CTS frame. In the macroscale scenario, we consider that the node in TM points its directional antenna to the receiver. For this, we consider that, at the link layer, the node in TM knows the position of the receiver. This information is provided by the network layer after a discovery process, which remains as future work. In the nanoscale scenario, we consider that nodes utilize omnidirectional antennas.
- A node in *receiving mode (RM)*, i.e., with sufficient resources (e.g., energy or even memory) to handle a new incoming transmission, broadcasts its status by means of a CTS frame. In the macroscale scenario, the node in RM uses a dynamically turning narrow-beam to broadcast CTS frames while sweeping its entire surrounding space. Such electrically-controlled high-speed turning directional antennas can be implemented for example by means of the proposed graphene-based plasmonic nano-antenna array (Sec. 4). The node in RM mode cannot know in advance who is willing to transmit, which is why it needs to sweep the entire space. The turning speed of beam is a parameter to be optimized in our analysis. In the nanoscale scenario, this information is omnidirectionally transmitted. The CTS frame also contains information on the receiver's current sliding window size.

Upon the reception of a CTS frame, a node in TM mode checks whether it has data for such receiver and the necessary resources. If so, it proceeds with the DATA frame transmission by taking into account also the receiver sliding window size. If the transmission is successful, the node in RM sends a positive acknowledgement (ACK) frame. Otherwise, after a time-out, the node in TM will set a random back-off time, which depends on the number of transmission attempts, and repeats the entire process when done. After successfully receiving a packet, i.e., successfully transmitting a CTS, a DATA and an ACK frames, the node in RM can decide to keep turning, continue to collect more packets, or switch to TM.

A couple of comments regarding *fairness* need to be made. First, as in any triggered reaction protocol, nodes in TM wait a random time after receiving a CTS frame and before sending the DATA frame. In the macroscale scenario, carrier-sense is performed during that time. In the nanoscale scenario, in which a pulsed-based physical layer is used, there is no carrier to sense, but the chances of having a collision are very low (Sec. 8.2.1). Second, only for the macroscale scenario, it is relevant to note that the node in RM cannot simply stop indefinitely at a node in TM, but it needs to continue "turning". Therefore, we need to guarantee that, within the small span of time that the node in RM is facing the node in TM, the DATA frame can be successfully transmitted. This is possible because nodes are transmitting at multi-Gbps and even Tbps and, thus, only several nanoseconds are

usually needed, which is much lower than in existing wireless communication systems and, thus, can be leveraged to effectively never stop turning.

Performance Analysis To analyze the performance of the proposed protocol, we analytically investigate the successful packet delivery probability, the packet delay and the throughput. First, we focus on the macroscale scenario and develop a mathematical framework in detail. Then, we summarize the differences needed to capture the nanoscale scenario peculiarities.

A. Macroscale Scenario In this case, the main factor affecting the performance of the protocol is the antenna turning speed ω , given in circles-per-second. In particular, we consider that the antenna shifts its direction in discrete steps and, thus, provides coverage to different sectors in different times. We define the sector time or time during which the antenna beam is pointing to a certain direction as $T_{sector} = \theta/(2\pi\omega)$. This limits the maximum number of retransmissions that a node can complete in the current round s . This affects the overall packet delay and throughput, as the node will have to wait for an entire cycle before being able to continue its ongoing transmission in round $s + 1$. More specifically, the maximum number of retransmission η_{max} that a node can complete in round s can be calculated as follows

$$\eta_{max} [s] = \min \left\{ \left\lfloor \frac{T_{sector} - T_{CTS} - T_{prop}}{T_{t/o} + T_{b/o}} \right\rfloor, k [s] \right\}, \quad (117)$$

where $T_{t/o} = 2T_{prop} + T_{proc} + T_{DATA} + T_{ACK}$ is the time-out time, T_{CTS} , T_{DATA} and T_{ACK} refer to the CTS, DATA, and ACK frames transmission time, respectively, and $T_{b/o}$ is a random exponential back-off time. In our analysis, we do not ignore the impact of the propagation delay T_{prop} , as it is comparable or even larger than the frame transmission time in the macroscale scenario. k is a parameter value that specifies the maximum number of retransmissions available in the current round. In particular, $k [1]$ is set to a default value k_0 . For example, if $k_0 = 5$, the total amount of retransmissions for a specific packet is equal to 5. This can be “consumed” within one round if T_{sector} is very long, i.e., the antenna turns at a slow speed, or might be spread across rounds, otherwise.

Then, the probability to succeed with exactly i retransmissions within the same round is given by

$$P_{succ}^{i-rtx} = P_{CTS} (1 - P_{DATA} P_{ACK})^{i-1} P_{DATA} P_{ACK}, \quad (118)$$

where $P_{CTS} = \overline{P_p} = (1 - P_p)$ is the probability of successfully receiving a CTS frame; $P_{DATA} = \overline{P_c} \overline{P_p}$ is the probability of successfully receiving a DATA frame; $P_{ACK} = \overline{P_p}$ is the probability of successfully receiving an ACK frame. We consider that the main reason for not properly receiving the CTS is the presence of bit errors, rather than the collision with other CTS. In the macroscale scenario, this is generally true, as it is very unlikely to have two or more receivers exactly pointing towards the same transmitter with their directional beams. Similarly, in the nanoscale scenario, given the energy constraints of nano-nodes, it is not likely to have many nearby receivers announcing their availability at the same time. When it comes to the DATA frame, failures might occur because of both bit errors as well as collisions. Even if we introduce a random initial delay between the CTS reception and the DATA transmission, collisions can occur. Finally, ACK frames might also suffer from bit errors.

From this, we can easily write the probability to successfully transmit the packet P_{succ}^{rnd} in

round s as well as the expected number of retransmissions η in that round as

$$P_{succ}^{rnd}[s] = \sum_{i=1}^{\eta_{max}[s]} P_{succ}^{i-rtx}; \quad \eta[s] = \sum_{i=1}^{\eta_{max}[s]} i P_{succ}^{i-rtx}. \quad (119)$$

If successful, the average successful packet delay introduced by the current round s can be calculated as

$$T_{succ}[s] = (\eta[s] - 1) (T_{t/o} + T_{b/o}) + T_{succ}^1, \quad (120)$$

where $T_{succ}^1 = 2T_{prop} + T_{proc} + T_{DATA} + T_{ACK}$ is the delay when successfully transmitting the packet in one attempt.

If the node is not successful in the current round, but the maximum number of retransmissions across rounds k_0 has not been yet achieved, the node waits for a new CTS frame (after one antenna cycle). Now $k[s+1] = k[s] - \eta^{max}[s]$. The maximum number of rounds Γ_{max} is given by

$$\Gamma_{max} = \min_s \{k[s] = 0\}. \quad (121)$$

Then, the probability to successfully transmit a packet in the j -th round is given by

$$P_{succ}^{j-rnd} = \left(\prod_{u=1}^{j-1} \left(1 - P_{succ}^{rnd}[u] \right) \right) P_{succ}^{rnd}[j], \quad (122)$$

where P_{succ}^{rnd} is given in (119).

From this, the total packet successful delivery probability and the average number of rounds needed to do so are given by

$$P_{succ} = \sum_{j=1}^{\Gamma_{max}} P_{succ}^{j-rnd}; \quad \Gamma = \sum_{j=1}^{\Gamma_{max}} j P_{succ}^{j-rnd}. \quad (123)$$

The discard probability immediately follows as $P_{dis} = \overline{P_{succ}}$. The average packet delay can similarly be obtained as:

$$T_{packet} = \sum_{j=1}^{\Gamma_{max}} \prod_{u=1}^{j-1} \left(1 - P_{succ}^{rnd}[u] \right) P_{succ}[j] \cdot ((j-1) T_{cycle} + T_{succ}[j]) + T_{wait}, \quad (124)$$

where T_{cycle} is the time needed for the antenna to complete one entire circle. T_{wait} refers to the average time that the transmitter will have to wait for the receiver's CTS in the first round, and is computed as follows

$$T_{wait} = \sum_{i=1}^{n_{sectors}} \overline{P_f}^{(i-1)} P_f (i-1) T_{sector}, \quad (125)$$

where $n_{sectors} = 2\pi/\theta$ is the number of sectors and $P_f = \theta/\pi$ is the transmitter and receiver facing probability. Finally, we can obtain the throughput as $S = n_{packet}/T_{packet}$, where n_{packet} is the number of bits per packet.

B. Nanoscale Scenario In this case, the main problem affecting the performance of the protocol is posed by the fluctuations in the available energy in each nano-device, which were discussed in Sec. 8.2.1. In our analysis, we consider that the battery in each nano-node can hold up to ϵ_{max} energy frames. An energy frame is the energy in Joules consumed in the reception of a control frame (CTS or ACK), also denoted as $\epsilon_{control}^{rx}$. Similarly, $\epsilon_{control}^{tx}$ denotes the energy frames required to transmit a control frame, and ϵ_{DATA}^{tx} and ϵ_{DATA}^{rx} are the number of energy frames needed to transmit and receive a DATA frame, respectively. The rate at which energy frames are harvested is denoted by λ_{harv} . Based on the probability distribution of the battery energy status, we can calculate the insufficient energy probability and its impact on the system.

The model now is fundamentally the same, with only few modifications. In this case, the reception of a CTS frame is not governed by the antenna turning speed ω and the sector time T_{sector} , but by the time needed by the receiver to harvest enough energy to operate and the announced CTS lifetime. Upon the reception of a CTS frame, the transmitter node checks whether it has enough energy to successfully transmit one or more packets. The new maximum number of retransmissions η_{max} in round s is given by

$$\eta_{max} [s] = \min \left\{ \left\lfloor \frac{CTS_{life}}{T_{t/o} + T_{b/o}} \right\rfloor, k [s], \left\lfloor \sum_{i=\epsilon^{tx}}^{\epsilon_{max}} P [level = i] \left\lfloor \frac{i - \epsilon^{tx}}{\epsilon_{retry}} \right\rfloor + 1 \right\rfloor \right\}, \quad (126)$$

where CTS_{life} refers to the CTS frame lifetime, set by the receiver according to its energy, $T_{t/o}$ and $T_{b/o}$ are the time-out and back-off times, respectively, defined similarly as for the macroscale scenario, $\epsilon^{tx} = \epsilon_{CTS}^{rx} + \epsilon_{DATA}^{tx} + \epsilon_{ACK}^{rx}$ is the energy required to complete a packet transmission on the transmitter side, $level$ is the number of energy frame units contained in the battery, and ϵ_{retry} is the energy spent in a retransmission. As before, k is a parameter value that specifies the maximum number of retransmissions still available.

In general, there is no guarantee that the transmitter and the receiver will have enough energy to successfully complete the packet transaction in one round, i.e., during the duration of the current CTS lifetime. As a result, both nodes might have to wait to harvest the required energy. The average waiting times for the transmitter and the receiver nodes are given by

$$T_{wait}^{tx/rx} = \frac{1}{\lambda_{harv}} \sum_{i=0}^{\epsilon^{tx/rx}} P [level = i] (\epsilon^{tx/rx} - i), \quad (127)$$

where $\epsilon^{rx} = \epsilon_{CTS}^{rx} + \epsilon_{DATA}^{rx} + \epsilon_{ACK}^{rx}$ is the required energy to start transmission from receiver side, and λ_{harv} is the energy harvesting rate in frames per second. Thus, the average waiting time for the packet transmission can be calculated as:

$$T_{wait} = P_{wait}^{tx} \overline{P_{wait}^{rx}} T_{wait}^{tx} + \overline{P_{wait}^{tx}} P_{wait}^{rx} T_{wait}^{rx} + P_{wait}^{tx} P_{wait}^{rx} \max \{T_{wait}^{tx}, T_{wait}^{rx}\}, \quad (128)$$

where

$$P_{wait}^{tx} = \sum_{i=0}^{\epsilon^{tx}} P [level = i]; P_{wait}^{rx} = \sum_{i=0}^{\epsilon^{rx}} P [level = i], \quad (129)$$

are the waiting probability for the transmitter and the receiver, respectively. The packet delay T_{delay} can be now obtained by utilizing (128) in (124) instead of (125). The rest of the analytical model remains the same.

8.3 Results and Discussions

In this section, we investigate the performance of the proposed protocol and compare it to that of CSMA/CA with and without RTS/CTS (2-way and 0-way handshake). The numerical results obtained by solving the analytical models developed in Sec. 8.2.2 are validated by simulation obtained with *ns-3*. For this, we have implemented the frequency-selective THz-band channel, the two THz physical layers (carrier-based and pulse-based with interleaving), the high-speed turning antenna, the energy harvesting unit, our proposed protocol and we also tailored and tuned CSMA/CA to work with the THz models. For completeness, we have also developed the analytical models for CSMA/CA with and without RTS/CTS, but these are not included due to space constraints.

8.3.1 Macroscale Scenario

In this case, we utilize the following parameter values. The network is composed by 18 nodes over a circular area with radius $l = 10$ m. The transmission power of each node is limited to $10 \mu\text{W}$. Nodes are equipped with turning directional antennas with directivity $D = 35$ dB, which corresponds to an antenna beam-width of approximately 32° . The center frequency f_c and bandwidth B are 1.05 THz and 100 GHz, respectively, which corresponds to the first absorption-defined transmission window above 1 THz (any other transmission window can be selected). The antenna turning speed is a parameter in our analysis. The back-off time $t_{b/o}$ and the sector time T_{sector} , which is utilized to also set the receiver sliding window, is adjusted according to the turning antenna speed. The maximum number of retransmissions k_0 is set to 5.

In Fig. 32, the packet discard probability is shown as a function of the antenna turning speed. As expected, with our proposed receiver-initiated or 1-way handshake protocol, the probability of discarding a packet is virtually zero and significantly much lower than 0-way and 2-way protocols. The main reason for this is that no retransmission attempts will be “wasted” when the receiver is not facing the transmitter, i.e., unless the transmitter has recently received a CTS frame from the intended receiver. This is not the case for the two traditional protocols, which might discard up to 30% of their generated packets as the facing probability given in (125) is very low for such very high directivity antennas.

However, the cost of a lower discard probability is reflected in the achievable throughput, which is plotted in Fig. 33 as a function of the antenna turning speed. For low turning antenna speeds, the throughput achieved by 0-way or 2-way protocols is higher than that of the proposed protocol, mainly because, successful packets (less than 80% of the total) have been transmitted when the receiver has been found facing at the transmitter, without the need to wait for it. As the antenna turning speed increases, the throughput for the proposed protocol increases and ultimately meets that of the other two protocols with the advantage of having no packets dropped. The values considered for the turning speed are conservative in light of the theoretically achievable with the aforementioned structures.

8.3.2 Nanoscale Scenario

In this case, we utilize the following parameter values. A circular area with radius $l = 0.01$ m with varying nano-node densities is considered. Nano-nodes communicate by utilizing TS-OOK

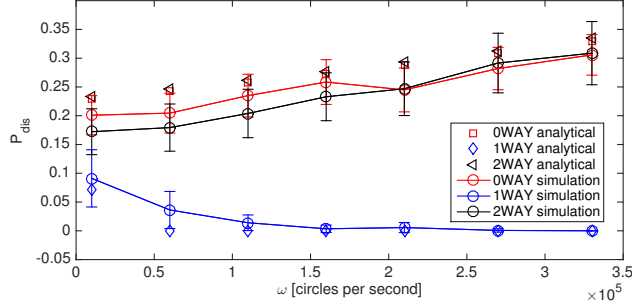


Fig. 32: Discard probability as a function of the antenna turning speed ω .

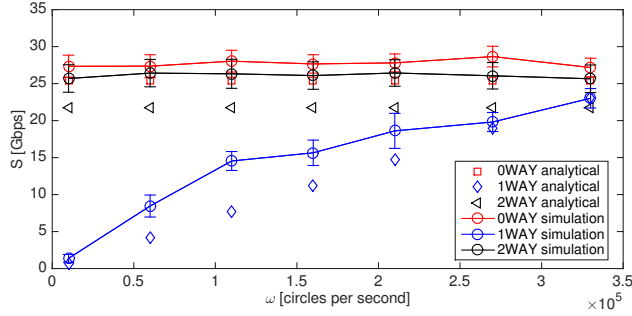


Fig. 33: Throughput as a function of the antenna turning speed ω .

with pulse energy $E_p=1$ attoJoule (aJ), pulse length $T_p=100$ fs, and spreading factor $T_s/T_p = 100$. Nodes utilize omnidirectional antennas with no directivity gain. For the energy model, we define $1/\lambda_{harv} = 8$ μ s per energy frame, $\epsilon_{control}^{rx}=1$, $\epsilon_{control}^{tx}=4$, $\epsilon_{DATA}^{rx}=16$, and $\epsilon_{DATA}^{tx}=64$ energy units. The capacity of the battery is $\epsilon_{max}=1000$ energy frames. These values have been obtained by taking into account the energy to transmit and receive a pulse, the coding weight, and the harvesting model given in [36].

In Fig. 34, the packet discard probability is shown as a function of the node density. Similarly as for the macroscale scenario, the number of dropped packets is significantly lower than with the other protocols. It is relevant to note that in this case, the 0-way handshake protocol has also a very low discard probability. The reason for this is because the time needed to harvest energy to transmit a packet is much larger than the time needed to harvest energy to receive. As a result, when the transmitter has enough energy to transmit, it is likely that the receiver has it too. However, for every transmission missed, the time before the next retransmission is very high. This can be seen in Fig. 35, where the throughput is shown as a function of the node density. Note that in this case the throughput for our proposed protocol is significantly higher than for the other two protocols (note the logarithmic scale). The reason is again related to the very long time needed for a node to have enough energy to transmit after a failed transmission. This emphasizes the need for transmitter-receiver synchronization, which is the main reason behind the one-way handshake.

8.3.3 Discussion

We have presented a link-layer synchronization and MAC protocol for ultra-high-speed wireless communication networks in the THz band. The protocol relies on a receiver-initiated handshake as well as a sliding window flow control mechanism to guarantee synchronization between transmitter

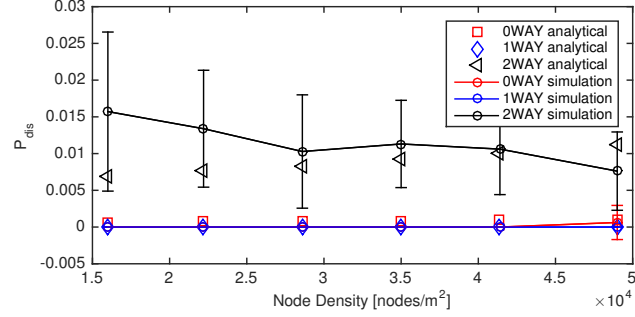


Fig. 34: Packet discard probability as a function of the node density.

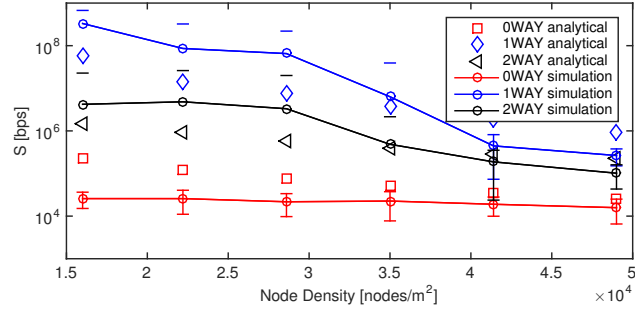


Fig. 35: Throughput as a function of the node density.

and receiver, maximize the channel utilization and minimize the packet discard probability. The performance of the proposed protocol is analytically investigated, compared to that of a modified CSMA/CA with and without RTS/CTS, and validated through extensive simulations with *ns-3*. The results show that the proposed protocol can maximize the successful packet delivery probability and enhance the achievable throughput in THz-band communication networks.

9 CONCLUSIONS

The potential impacts of THz communication, once realized, would be second to none. THz technology has been recently *identified by DARPA as one of the four major research areas that could eventually have an impact on our society larger than that of the Internet itself* [97]. The THz band opens the door to a plethora of applications [8] in very diverse domains, ranging from Terabit Wireless Personal and Local Area Networks to wireless nanosensor networks [29] or the Internet of Nano-Things [34]. In this context, the development of a new communication and networking technology to support networks with “billions of connected nanosystems” has been recently identified as *one of the four essential components of the next IT revolution by the Semiconductor Research Consortium and NSF* [98].

As part of this project, we have made novel contributions across different aspects required to enable practical THz communication systems. For a period of 20 months and with a total budget of \$240,000, we have developed both novel device concepts as well as physical and link layer solutions, which resulted in a total of eight conference paper publications [24, 26, 28, 30, 31, 33, 37, 38], three journal publications [27, 32, 39], four additional journals submitted for publication or in preparation, and potentially one patent application.

As part of this project, four graduate students have been partially supported. The developed work has been presented at conferences by the PIs as well as their students, who have been trained to become experts in this quickly evolving field. Through their participation in conferences, they have also been exposed to other research groups and research areas, and have now a better understanding of the broad wireless communication community.

As with any new pioneering field, the dissemination of the work is of key importance. Besides the aforementioned conferences, the PIs have actively presented their works in different venues. PI Jornet has taught three invited courses and three invited seminars on THz communications in national and international universities. In addition, he organized and hosted the first Joint Academia and Industry Panel on THz Communications, at IEEE GLOBECOM 2015, one of the premiere conferences of the IEEE Communications Society. Co-PI Einarsson presented results at the 2016 IRMMW-THz conference and at an invited seminar at Binghamton University, and his student supported by this project presented her work at the 2016 American Physical Society March Meeting.

10 LIST OF ACRONYMS

AFOSR	Air Force Office of Scientific Research
AFRL	Air Force Research Laboratory
BER	Bit Error Rate
CSMA	Carrier-Sense Multiple Access
CTMA	Continuous-time Moving Average
FER	Frame Error Rate
MAC	Medium Access Control
PDF	Probability Density Function
PSD	Power Spectral Density
SER	Symbol Error Rate
SNR	Signal-to-Noise Ratio
SPP	Surface Plasmon Polariton
USAF	United States Air Force
VCD	Voltage-controlled Delay

References

- [1] Cisco, “Cisco visual networking index: Global mobile data traffic forecast update, 2015–2020,” *White Paper*, Feb. 2016.
- [2] S. Cherry, “Edholm’s law of bandwidth,” *IEEE Spectrum*, vol. 41, no. 7, pp. 58 – 60, Jul. 2004.
- [3] I. F. Akyildiz, D. M. Gutierrez-Estevez, R. Balakrishnan, and E. Chavarria-Reyes, “LTE-Advanced and the Evolution to Beyond 4G (B4G) Systems,” *Physical Communication (Elsevier) Journal*, vol. 10, pp. 31–60, March 2014.
- [4] T. Rappaport, J. Murdock, and F. Gutierrez, “State of the art in 60-ghz integrated circuits and systems for wireless communications,” *Proceedings of the IEEE*, vol. 99, no. 8, pp. 1390 –1436, Aug. 2011.
- [5] M. A. Khalighi and M. Uysal, “Survey on free space optical communication: A communication theory perspective,” *IEEE Communications Surveys Tutorials*, vol. 16, no. 4, pp. 2231–2258, Fourthquarter 2014.
- [6] J. Federici and L. Moeller, “Review of terahertz and subterahertz wireless communications,” *Journal of Applied Physics*, vol. 107, no. 11, p. 111101, 2010.
- [7] H.-J. Song and T. Nagatsuma, “Present and future of terahertz communications,” *IEEE Transactions on Terahertz Science and Technology*, vol. 1, no. 1, pp. 256–263, 2011.
- [8] I. F. Akyildiz, J. M. Jornet, and C. Han, “Terahertz band: Next frontier for wireless communications,” *Physical Communication (Elsevier) Journal*, vol. 12, pp. 16 – 32, Sep. 2014.
- [9] T. Kurner and S. Priebe, “Towards THz Communications-Status in Research, Standardization and Regulation,” *Journal of Infrared, Millimeter, and Terahertz Waves*, vol. 35, no. 1, pp. 53–62, 2014.
- [10] S. Koenig, D. Lopez-Diaz, J. Antes, F. Boes, R. Henneberger, A. Leuther, A. Tessmann, R. Schmogrow, D. Hillerkuss, R. Palmer *et al.*, “Wireless sub-thz communication system with high data rate,” *Nature Photonics*, vol. 7, no. 12, pp. 977–981, 2013.
- [11] Y. Kurita, G. Ducournau, D. Coquillat, A. Satou, K. Kobayashi, S. B. Tombet, Y. Meziani, V. Popov, W. Knap, T. Suemitsu *et al.*, “Ultrahigh sensitive sub-terahertz detection by inp-based asymmetric dual-grating-gate high-electron-mobility transistors and their broadband characteristics,” *Applied Physics Letters*, vol. 104, no. 25, p. 251114, 2014.
- [12] V. Radisic, K. Leong, D. Scott, C. Monier, X. Mei, W. Deal, and A. Gutierrez-Aitken, “Sub-millimeter wave inp technologies and integration techniques,” in *IEEE MTT-S International Microwave Symposium (IMS)*, May 2015, pp. 1–4.
- [13] B. S. Williams, “Terahertz quantum-cascade lasers,” *Nature photonics*, vol. 1, no. 9, pp. 517–525, 2007.

- [14] Q. Lu, S. Slivken, N. Bandyopadhyay, Y. Bai, and M. Razeghi, “Widely tunable room temperature semiconductor terahertz source,” *Applied Physics Letters*, vol. 105, no. 20, p. 201102, 2014.
- [15] Q. Lu, D. Wu, S. Sengupta, S. Slivken, and M. Razeghi, “Room temperature continuous wave, monolithic tunable thz sources based on highly efficient mid-infrared quantum cascade lasers,” *Scientific reports*, vol. 6, 2016.
- [16] S. Slivken and M. Razeghi, “High power, electrically tunable quantum cascade lasers,” in *SPIE OPTO*. International Society for Optics and Photonics, 2016, pp. 97 550C–97 550C.
- [17] K. S. Novoselov, V. Fal, L. Colombo, P. Gellert, M. Schwab, K. Kim *et al.*, “A roadmap for graphene,” *Nature*, vol. 490, no. 7419, pp. 192–200, 2012.
- [18] A. C. Ferrari, F. Bonaccorso, V. Fal’Ko, K. S. Novoselov, S. Roche, P. Bøggild, S. Borini, F. H. Koppens, V. Palermo, N. Pugno *et al.*, “Science and technology roadmap for graphene, related two-dimensional crystals, and hybrid systems,” *Nanoscale*, vol. 7, no. 11, pp. 4598–4810, 2015.
- [19] J. M. Jornet and I. F. Akyildiz, “Graphene-based plasmonic nano-antenna for terahertz band communication in nanonetworks,” *IEEE JSAC, Special Issue on Emerging Technologies for Communications*, vol. 12, no. 12, pp. 685–694, Dec. 2013.
- [20] I. F. Akyildiz and J. M. Jornet, “Graphene-based plasmonic nano-antenna for terahertz band communication,” U.S. Patent 14/253,539, 2013.
- [21] J. M. Jornet and I. F. Akyildiz, “Graphene-based plasmonic nano-transceiver for terahertz band communication,” in *Proc. of European Conference on Antennas and Propagation (EuCAP)*, 2014.
- [22] I. F. Akyildiz and J. M. Jornet, “Graphene-based plasmonic nano-transceiver for wireless communication in the terahertz band,” U.S. Patent 9,397,758, 2016.
- [23] J. M. Jornet and I. F. Akyildiz, “Channel modeling and capacity analysis of electromagnetic wireless nanonetworks in the terahertz band,” *IEEE Transactions on Wireless Communications*, vol. 10, no. 10, pp. 3211–3221, Oct. 2011.
- [24] P. K. Singh, G. Aizin, N. Thawdar, M. Medley, and J. M. Jornet, “Graphene-based plasmonic phase modulator for terahertz-band communication,” in *Proc. of the European Conference on Antennas and Propagation (EuCAP)*, 2016.
- [25] I. F. Akyildiz and J. M. Jornet, “Realizing ultra-massive mimo (1024× 1024) communication in the (0.06–10) terahertz band,” *Nano Communication Networks*, vol. 8, pp. 46–54, 2016.
- [26] L. Zakrajsek, E. Einarsson, N. Thawdar, M. Medley, and J. M. Jornet, “Design of graphene-based plasmonic nano-antenna arrays in the presence of mutual coupling,” in *Proc. of European Conference on Antennas and Propagation (EuCAP)*, 2017.

- [27] L. Zakrajsek, E. Einarsson, N. Thawdar, M. Medley, and J. M. Jornet, “Lithographically defined plasmonic graphene antennas for terahertz-band communication,” *IEEE Antennas and Wireless Propagation Letters*, vol. 15, pp. 1553–1556, 2016.
- [28] F. Vandrevala, A. Karmakar, J. M. Jornet, and E. Einarsson, “Extracting complex optical properties of ultra-thin conductors using time-domain thz spectroscopy,” in *Proc. of the 41st International Conference on Infrared, Millimeter and Terahertz Waves (IRMMW-THz)*, 2016.
- [29] I. F. Akyildiz and J. M. Jornet, “Electromagnetic wireless nanosensor networks,” *Nano Communication Networks (Elsevier) Journal*, vol. 1, no. 1, pp. 3–19, Mar. 2010.
- [30] Z. Hossain, S. H. Vedant, C. R. Nicoletti, and J. F. Federici, “Multi-user interference modeling and experimental characterization for pulse-based terahertz communication,” in *Proc. of the Third ACM International Conference on Nanoscale Computing and Communication (NanoCom)*, 2016.
- [31] V. Petrov, M. Komarov, D. Moltchanov, J. M. Jornet, and Y. Koucheryavy, “Interference analysis of ehf/thf communications systems with blocking and directional antennas,” in *Proc. of IEEE GLOBECOM*, 2016.
- [32] V. Petrov, D. Moltchanov, P. Kustarev, J. M. Jornet, and Y. Koucheryavy, “On the use of integral geometry for interference modeling and analysis in wireless networks,” *IEEE Communications Letters*, vol. PP, no. 99, pp. 1–1, 2016.
- [33] A. Gupta, M. Medley, and J. M. Jornet, “Joint synchronization and symbol detection design for pulse-based communications in the thz band,” in *Proc. of IEEE GLOBECOM*, 2015.
- [34] I. F. Akyildiz and J. M. Jornet, “The internet of nano-things,” *IEEE Wireless Communications Magazine*, vol. 17, no. 6, pp. 58–63, Dec. 2010.
- [35] Z. L. Wang, “Towards self-powered nanosystems: from nanogenerators to nanopiezotronics,” *Advanced Functional Materials*, vol. 18, no. 22, pp. 3553–3567, 2008.
- [36] J. M. Jornet and I. F. Akyildiz, “Joint energy harvesting and communication analysis for perpetual wireless nanosensor networks in the terahertz band,” *IEEE Transactions on Nanotechnology*, vol. 11, no. 3, pp. 570–580, 2012.
- [37] P. Johari and J. M. Jornet, “Packet size optimization for wireless nanosensor networks in the terahertz band,” in *2016 IEEE International Conference on Communications (ICC)*. IEEE, 2016, pp. 1–6.
- [38] Q. Xia, Z. Hossain, M. Medley, and J. M. Jornet, “A link-layer synchronization and medium access control protocol for terahertz-band communication networks,” in *Proc. of IEEE GLOBECOM*, Dec. 2015.
- [39] X.-W. Yao and J. M. Jornet, “Tab-mac: Assisted beamforming mac protocol for terahertz communication networks,” *Nano Communication Networks*, vol. 9, pp. 36–42, 2016.

- [40] M. Rahm, J.-S. Li, and W. J. Padilla, “Thz wave modulators: a brief review on different modulation techniques,” *Journal of Infrared, Millimeter, and Terahertz Waves*, vol. 34, no. 1, pp. 1–27, 2013.
- [41] T. Kleine-Ostmann, P. Dawson, K. Pierz, G. Hein, and M. Koch, “Room-temperature operation of an electrically driven terahertz modulator,” *Applied physics letters*, vol. 84, no. 18, pp. 3555–3557, 2004.
- [42] H.-T. Chen, W. J. Padilla, M. J. Cich, A. K. Azad, R. D. Averitt, and A. J. Taylor, “A metamaterial solid-state terahertz phase modulator,” *Nature Photonics*, vol. 3, no. 3, pp. 148–151, 2009.
- [43] S. Luo, Y. Wang, X. Tong, and Z. Wang, “Graphene-based optical modulators,” *Nanoscale Research Letters*, vol. 10, no. 1, pp. 1–11, 2015.
- [44] B. Sensale-Rodriguez, R. Yan, M. M. Kelly, T. Fang, K. Tahy, W. S. Hwang, D. Jena, L. Liu, and H. G. Xing, “Broadband graphene terahertz modulators enabled by intraband transitions,” *Nature Communications*, vol. 3, pp. 780+, Apr. 2012.
- [45] S. H. Lee, H.-D. Kim, H. J. Choi, B. Kang, Y. R. Cho, and B. Min, “Broadband modulation of terahertz waves with non-resonant graphene meta-devices,” *IEEE Transactions on Terahertz Science and Technology*, vol. 3, no. 6, pp. 764–771, 2013.
- [46] L. Falkovsky and A. A. Varlamov, “Space-time dispersion of graphene conductivity,” *The European Physical Journal B*, vol. 56, pp. 281–284, 2007.
- [47] G. W. Hanson, “Dyadic Green’s functions and guided surface waves for a surface conductivity model of graphene,” *Journal of Applied Physics*, vol. 103, no. 6, p. 064302, 2008.
- [48] M. Jablan, H. Buljan, and M. Soljačić, “Plasmonics in graphene at infrared frequencies,” *Physical Review B*, vol. 80, p. 245435, Dec. 2009.
- [49] I. Llatser, C. Kremers, A. Cabellos-Aparicio, J. M. Jornet, E. Alarcon, and D. N. Chigrin, “Graphene-based nano-patch antenna for terahertz radiation,” *Photonics and Nanostructures - Fundamentals and Applications*, vol. 10, no. 4, pp. 353–358, Oct. 2012.
- [50] M. Tamagnone, J. S. Gomez-Diaz, J. R. Mosig, and J. Perruisseau-Carrier, “Reconfigurable terahertz plasmonic antenna concept using a graphene stack,” *Applied Physics Letters*, vol. 101, no. 21, p. 214102, 2012.
- [51] V. Ryzhii, “Terahertz plasma waves in gated graphene heterostructures,” *Japanese journal of applied physics*, vol. 45, no. 9L, p. L923, 2006.
- [52] J. G. Proakis and D. K. Manolakis, *Digital Signal Processing (4th Edition)*. Upper Saddle River, NJ, USA: Prentice-Hall, Inc., 2006.
- [53] J. M. Jornet and I. F. Akyildiz, “Graphene-based nano-antennas for electromagnetic nanocommunications in the terahertz band,” in *Proc. of 4th European Conference on Antennas and Propagation, EUCAP*, Apr. 2010.

- [54] M. Aldrigo, M. Dragoman, and D. Dragoman, “Smart antennas based on graphene,” *Journal of Applied Physics*, vol. 116, no. 11, 2014.
- [55] W. Tan, Y. Sun, Z.-G. Wang, and H. Chen, “Manipulating electromagnetic responses of metal wires at the deep subwavelength scale via both near-and far-field couplings,” *Applied Physics Letters*, vol. 104, no. 9, p. 091107, 2014.
- [56] H. A. Haus, *Waves and fields in optoelectronics*. Prentice-Hall, 1984.
- [57] E. Van Lil and A. Van de Capelle, “Transmission line model for mutual coupling between microstrip antennas,” *IEEE Transactions on antennas and propagation*, vol. 32, no. 8, pp. 816–821, 1984.
- [58] M. Malkomes, “Mutual coupling between microstrip patch antennas,” *Electronics Letters*, vol. 18, pp. 520–522, 1982.
- [59] E. Penard and J.-P. Daniel, “Mutual coupling between microstrip antennas,” *Electronics Letters*, vol. 18, pp. 605–607, 1982.
- [60] A. Derneryd, “A theoretical investigation of the rectangular microstrip antenna element,” *IEEE Transactions on Antennas and Propagation*, vol. 26, no. 4, pp. 532–535, 1978.
- [61] C. A. Balanis, *Antenna theory: analysis and design*. John Wiley & Sons, 2005.
- [62] S. Priebe and T. Kurner, “Stochastic modeling of thz indoor radio channels,” *IEEE Transactions on Wireless Communications*, vol. 12, no. 9, pp. 4445–4455, 2013.
- [63] J. M. Jornet and I. F. Akyildiz, “Femtosecond-long pulse-based modulation for terahertz band communication in nanonetworks,” *IEEE Transactions on Communications*, vol. 62, no. 5, pp. 1742 – 1754, May 2014.
- [64] J. Andrews, R. Ganti, M. Haenggi, N. Jindal, and S. Weber, “A primer on spatial modeling and analysis in wireless networks,” *Communications Magazine, IEEE*, vol. 48, no. 11, pp. 156 –163, Nov. 2010.
- [65] P. Cardieri, “Modeling interference in wireless ad hoc networks,” *IEEE Communications Surveys and Tutorials*, vol. 12, no. 4, pp. 551–572, 2010.
- [66] M. Win, P. Pinto, and L. Shepp, “A mathematical theory of network interference and its applications,” *Proceedings of the IEEE*, vol. 97, no. 2, pp. 205 –230, Feb. 2009.
- [67] J. M. Jornet, “Low-weight error-prevention codes for electromagnetic nanonetworks in the terahertz band,” *Nano Communication Networks (Elsevier) Journal*, vol. 5, no. 1-2, pp. 35–44, March-June 2014.
- [68] R. Merz, M. Flury, and J.-V. L. Boudec, “Synchronization for impulse-radio uwb with energy detection and multi-user interface: Algorithms and applications to ieee 802.15.4a,” *IEEE Transactions on Signal Processing*, vol. 59, no. 11, pp. 5458–5472, Nov. 2011.

- [69] R. Akbar, S. A. Emanuel Radoi, and M. N. ul Islam, “Low complexity synchronization algorithms for orthogonally modulated ir-uwb systems,” *EURASIP Journal on Wireless Communications and Networking*, 2013.
- [70] X. Y. Wang and A. B. Apsel, “Pulse coupled oscillator synchronization for low power uwb wireless transceivers,” in *Circuits and Systems, 2007. MWSCAS 2007. 50th Midwest Symposium on*. IEEE, 2007, pp. 1524–1527.
- [71] Fujitsu. 56GSa/s 8-bit Analog-to-Digital Converter. [Online]. Available: http://www.fujitsu.com/downloads/MICRO/fma/pdf/56G_ADC_FactSheet.pdf
- [72] F. Rana, “Graphene terahertz plasmon oscillators,” *IEEE Transactions on Nanotechnology*, vol. 7, no. 1, pp. 91–99, Jan. 2008.
- [73] J. T. Kim and S.-Y. Choi, “Graphene-based plasmonic waveguides for photonic integrated circuits,” *Optics express*, vol. 19, no. 24, pp. 24 557–24 562, 2011.
- [74] R. G. Cid-Fuentes, J. M. Jornet, E. Alarcon, and I. F. Akyildiz, “A receiver architecture for pulse-based electromagnetic nanonetworks in the terahertz band,” in *Proc. of IEEE International Conference on Communications, ICC*, Jun. 2012.
- [75] A. Vakil and N. Engheta, “Transformation optics using graphene,” *Science*, vol. 332, no. 6035, pp. 1291–1294, Jun. 2011.
- [76] R. F. Mills and G. E. Prescott, “A comparison of various radiometer detection models,” *Aerospace and Electronic Systems, IEEE Transactions on*, vol. 32, no. 1, pp. 467–473, 1996.
- [77] D. Pompili, T. Melodia, and I. F. Akyildiz, “Routing algorithms for delay-insensitive and delay-sensitive applications in underwater sensor networks,” in *Proc. of the 12th ACM Annual International Conference on Mobile Computing and Networking (MobiCom)*, 2006, pp. 298–309.
- [78] M. Vuran and I. F. Akyildiz, “Cross-layer packet size optimization for wireless terrestrial, underwater, and underground sensor networks,” in *Proc. of the 27th IEEE Conference on Computer Communications (INFOCOM)*, 2008.
- [79] M. Stojanovic, “Optimization of a data link protocol for an underwater acoustic channel,” in *Proc. of IEEE Oceans 2005-Europe*, vol. 1, 2005, pp. 68–73.
- [80] M. C. Domingo, “Packet size optimization for improving the energy efficiency in body sensor networks,” *ETRI Journal*, vol. 33, no. 3, pp. 299–309, 2011.
- [81] A. Seyed and B. Sikdar, “Energy efficient transmission strategies for body sensor networks with energy harvesting,” *IEEE Transactions on Communications*, vol. 58, no. 7, pp. 2116–2126, 2010.
- [82] K. Tutuncuoglu and A. Yener, “Optimum transmission policies for battery limited energy harvesting nodes,” *IEEE Transactions on Wireless Communications*, vol. 11, no. 3, pp. 1180–1189, 2012.

- [83] V. Sharma, U. Mukherji, V. Joseph, and S. Gupta, “Optimal energy management policies for energy harvesting sensor nodes,” *IEEE Transactions on Wireless Communications*, vol. 9, no. 4, pp. 1326–1336, 2010.
- [84] S. Mohrehkesh and M. C. Weigle, “Optimizing energy consumption in terahertz band nanonetworks,” *IEEE Journal on Selected Areas in Communications*, vol. 32, no. 12, pp. 2432–2441, 2014.
- [85] N. Akkari, J. Jornet, P. Wang, E. Fadel, L. Elrefaei, M. Malik, S. Almasri, and I. Akyildiz, “Joint physical and link layer error control analysis for nanonetworks in the terahertz band,” *Wireless Networks*, pp. 1–13, 2015.
- [86] S. Boyd and L. Vandenberghe, *Convex optimization*. Cambridge university press, 2004.
- [87] S. Singh, R. Mudumbai, and U. Madhow, “Interference analysis for highly directional 60-ghz mesh networks: The case for rethinking medium access control,” *IEEE/ACM Transactions on Networking*, vol. 19, no. 5, pp. 1513–1527, 2011.
- [88] P. Bai, G. Zhu, Y. Liu, J. Chen, Q. Jing, W. Yang, J. Ma, G. Zhang, and Z. L. Wang, “Cylindrical rotating triboelectric nanogenerator,” *ACS nano*, vol. 7, no. 7, pp. 6361–6366, 2013.
- [89] *IEEE 802.11ad-2012: Wireless LAN Medium Access Control (MAC) and Physical Layer (PHY) Specifications Amendment 3: Enhancements for Very High Throughput in the 60 GHz Band*, IEEE Standard for Information Technology, Telecommunications and Information Exchange between Systems Std.
- [90] T. Tandai, R. Matsuo, T. Tomizawa, H. Kasami, and T. Kobayashi, “Mac efficiency enhancement with prioritized access opportunity exchange protocol for 60 ghz short-range one-to-one communications,” in *IEEE 73rd Vehicular Technology Conference (VTC)*, 2011, pp. 1–5.
- [91] F. Yildirim and H. Liu, “Directional mac for 60 ghz using polarization diversity extension (dmac-pdx),” in *IEEE Global Telecommunications Conference (GLOBECOM)*, 2007, pp. 4697–4701.
- [92] Q. Chen, J. Tang, D. T. C. Wong, X. Peng, and Y. Zhang, “Directional cooperative mac protocol design and performance analysis for ieee 802.11 ad wlans,” *IEEE Transactions on Vehicular Technology*, vol. 62, no. 6, pp. 2667–2677, 2013.
- [93] R. R. Choudhury, X. Yang, R. Ramanathan, and N. Vaidya, “On designing mac protocols for wireless networks using directional antennas,” *IEEE Transactions on Mobile Computing*, vol. 5, no. 5, pp. 477–491, 2006.
- [94] M. Takata, M. Bandai, and T. Watanabe, “A receiver-initiated directional mac protocol for handling deafness in ad hoc networks,” in *IEEE International Conference on Communications (ICC)*, vol. 9, 2006, pp. 4089–4095.
- [95] P. Wang, J. M. Jornet, M. Abbas Malik, N. Akkari, and I. F. Akyildiz, “Energy and spectrum-aware mac protocol for perpetual wireless nanosensor networks in the terahertz band,” *Ad Hoc Networks (Elsevier) Journal*, vol. 11, no. 8, pp. 2541–2555, 2013.

- [96] S. Mohrehkesh and M. C. Weigle, “Rih-mac: receiver-initiated harvesting-aware mac for nanonetworks,” in *Proceedings of ACM The First Annual International Conference on Nanoscale Computing and Communication*, 2014, pp. 1–9.
- [97] A. Prabhakar, “Statement by the Director of the Defense Advanced Research Projects Agency submitted to the US Senate Committee on Appropriations,” Defense Advanced Research Projects Agency, Tech. Rep., 2014.
- [98] Semiconductor Industry Association and Semiconductor Research Corporation, “Rebooting the IT Revolution: A Call to Action,” Tech. Rep., Aug. 2015.